Volumetric adaptive optical multiphoton microscope for *in vivo* imaging and photomanipulation

Yongxiao Li

Department of Engineering

The Australian National University

This dissertation is submitted for the degree of

Doctor of Philosophy

I would like to dedicate this thesis to the people who are suffering.

Declaration

I hereby declare that except where specific reference is made to the work of others, the contents of this dissertation are original and have not been submitted in whole or in part for consideration for any other degree or qualification in this, or any other university. This dissertation is the result of my own work and includes nothing which is the outcome of work done in collaboration, except where specifically indicated in the text. This dissertation contains less than 55,000 words including appendices, bibliography, footnotes, tables and equations and has less than 150 figures.

Yongxiao Li

2019

Acknowledgements

It is a great pleasure and enjoyable experience of doing my PhD at the Australian National University (ANU) in Australia. First, I want to thank ANU for granting me the University Research Scholarship, which makes this memorial voyage possible. Moreover, thank you Canberra, the capital of Australia, a perfect place for study, for your peaceful scenery and the welcoming residents, it is much harder to say goodbye than I thought after four years.

Obtaining the right of writing this thesis to me, is a tortuous journey, after three years of master study and two years of industrial working, I finally got the chance of doing PhD in this fascinating bioimaging field that I am very much interested. Therefore, the first and most important person I would like to thank and acknowledge, is my supervisor, Steve (Woei Ming) Lee. Thank you for supporting my PhD application and trusting me with this complex interdisciplinary study, thank you for arranging the full training schedule with different projects from different departments across the university, from astronomy to physics and biomedical. Thank you for showing me what high quality research should be. In all, thank you for your continuous knowledge imparting, doctrine propagating and doubts resolving through my whole PhD studies.

I also have a robust academic committee and several collaborators who facilitated my study a lot, Elizabeth Gardiner (Liz), Cathy Gillespie, Francois Rigaut, John Chow, Roland Fleddermann, Lynette Beattie and Barry Luther-Davies. Thanks, Elizabeth Gardiner (Liz) for instructing platelets study and providing the working space at the John Curtin School of Medical Research (JCSMR) as well as being my referee for my postdoc applications. You are always there and giving me suggestions about my career. Thanks, Cathy Gillespie for supporting and arranging the microscope resources to me. Thanks, Francois for teaching me the adaptive optics in the Stromlo Observatory. Thanks, John Chow and Roland for teaching me the optical coherence tomography technique in the Physics Department. Thanks, Lynette for teaching me the immunology organ imaging. Thanks, Barry Luther-Davies for teaching me the femtosecond laser and three photon microscope.

Also, thanks to Nicolò (Nic) Malagutti, for providing me with the tutor position at the last stage of my PhD, given me a valuable tutorial experience and salary support of writing the thesis.

I would also like to thank my group colleagues and college mates, Tahseen Kamal, Samantha (Sam) Montague, Tao Xu, Jiazheng Ji, Yujie Zheng, Tienan Xu, Thomas (Tom) McMenamin, Xuefei He, Avinash Upadhya, Qiongkai Xu, Daniel Lim, Josie Munro, Alex Ma, Zhiduo Zhang, Wei Zong, Juan David Adarve, Xiaoshuai Huang and Xinxin Peng. The discussions and advice from you guys inspired me a lot not only in study but also in life. I know when I get problems, there will always be a help.

Except for the study, I also want to thank my roommates, Rongxuan Liu and Zongqiao Guan. It is such a fortune to get along, sharing our joy and distress.

Finally, I would like to thank my wife and my parents as well as my son. Thank you all for the supporting and understanding, it is hard to imagine how a 30s PhD student can survive without the help and suffering from their families. I have nothing but your love, I know from deep of my heart that the family is the always my source of moving forward.

Abstract

Modern biological studies are mainly built upon observational sciences and thus rely heavily on imaging and manipulation tools. The light microscope is one of the most widely recognized instrument in life science that can decipher fundamental biological processes over several length scales; from the molecules at the genetic level to the organelles of living cells and tissues in living organs. Modern optical microscopy is no longer a single lens but the intricate and creative combination of laser engineering, optical design, software development and biochemical labelling. A well-orchestrated advanced microscope system accumulates high throughput spatial-temporal information of biological processes volumetrically as well as possesses the ability to manipulate biological events of living cells in its native microenvironment within a living host. Amongst all the laser scanning microscopy, multiphoton microscope, is widely used to study cellular and sub-cellular events ranging from immunological diseases model to neurological responses in living mice. A critical success in the multiphoton microscope is the unprecedented imaging depth and imaging resolution from the nonlinear optical absorption. Because of this nonlinear optical effect, it becomes possible to excite fluorophores and identify specific proteins through deep layers of biological tissues and track them over time. However, the inefficiencies of multiphoton microscopy restraint the delivering of concentrated photons over space and time within highly scattering tissue. A grand challenge in the multiphoton microscope is to provide real-time volumetric information that will allow high throughput of spatial-temporal information of cells being collected from thick living biological tissue.

In this thesis, I shall elaborate upon the design, development and application of a rapid volumetric scanning multiphoton microscope platform with adaptive optics (AO) capability for the intravital imaging and photomanipulation. The work reported in this thesis tackles the developmental steps on both the hardware and software for the polygonal mirror microscope system. A broad range of *in vivo* imaging experiments with a keen focus on microvasculature imaging is demonstrated. A significant milestone achievement in this work is the fully functioning video-rate AO at 20 frames per second through a unique raster aberration correction method. Furthermore, the polygon multiphoton microscope was shown to achieve

volumetric imaging (1~10 volume per second) with an extendable imaging field of view (FOV) from 300 μm x 450 μm x 80 μm to 700 μm x 600 μm x 80 μm. The system could achieve a space bandwidth product (SBP- digital pixel density from 512 x 512 pixels ~ 10240 x 10240 pixels) in a single acquisition for high spatial-temporal throughput beyond most existing mirror-based multiphoton microscope systems. An essential delivery in this thesis is the that the devices and functions are fully integrated into a customized control software named PScan, that provides not only an accessible operation interface for high throughput imaging but also offers photomanipulation capabilities. Unlike other polygon microscope systems, this system developed in this thesis allows rapid switching between imaging and localized photomanipulation in a single laser scanning system. The flexibility of our system was confirmed by performing laser induced injury to observe blood cell dynamics and thrombus formation along the femoral artery of the mice.

In the first chapter (Chapter 1), I shall provide a general introduction and discussion of the development of state of the art intravital microscopy based on the multiphoton microscope, followed by laying out the background of light-tissue interaction and reviewing existing approaches in beam engineering tools used in multiphoton microscopies. In the following three chapters (Chapter 2 - 4), I shall first describe in detail our approach in designing, constructing and implementing of the next generation of polygon based multiphoton system along with the control software PScan (Chapter 2). Then illustrate a new raster adaptive optics (RAO) method that can rapidly compensate the field-dependent aberration, which is a critical hurdle in modern AO microscopes. Using RAO, we achieved video-rate AO over a wide-field of view. Although RAO is a time multiplexing approach, it was able to achieve a 5 ms update rate. Chapter 4 will describe volumetric imaging and photomanipulation in polygon microscope system through the application of a piezo-deformable mirror and a switchable binary slit. It achieved localized photomanipulation for fluorescence recovery after photobleaching (FRAP) and laser induced injury, which are essential steps for future quantification of *in vivo* thrombus studies. Finally, in Chapter 5, I shall summaries the critical outcomes of the thesis and also propose plans to further expanding the many functions of the microscope system for *in vivo* longitudinal photoconversion imaging.

In summary, this thesis presents the detail of designing and building a state of the art volumetric microscope that achieves multi-functionality imaging performance (speed, FOV,

contrast, aberration-free) for *in vivo* studies of mice models. I anticipate that this volumetric microscope will be beneficial for a broader field of laser scanning microscopy for biologists and I believe that the publication of this thesis will impact various areas of biological sciences such as neurobiology, immunology and cancer research.

Related Publications

Journals

1. **Li, Y.,** Lim, Y. J., Xu, Q., Beattie, L., Gardiner, E. E., Gaus, K., ... & Lee, W. M. (2020). "Raster adaptive optics for video rate aberration correction and large FOV multiphoton imaging". Biomedical Optics Express, 11(2), 1032-1042. **(Chapter 3)**
2. **Li, Y.**, Montague, S. J., Brüstle, A., He, X., Gillespie, C., Gaus, K., ... & Lee, W. M. (2018). "High contrast imaging and flexible photomanipulation for quantitative in vivo multiphoton imaging with polygon scanning microscope". Journal of biophotonics, 11(7), e201700341. **(Chapter 2 and 4)**
3. Lee, W. M., McMenamin, T., & **Li, Y.** (2018). "Optical toolkits for *in vivo* deep tissue laser scanning microscopy: a primer". Journal of Optics, 20(6), 063002. **(Chapter 1)**.
4. **Li, Y.** , Gautam, V., Brüstle, A., Cockburn, I. A., Daria, V. R., Gillespie, C., ... & Lee, W. M. (2017). "Flexible polygon mirror based laser scanning microscope platform for multiphoton *in vivo* imaging". Journal of biophotonics, 10(11), 1526-1537. **(Chapter 2)**

Conference Proceedings

1. **Li, Y.**, Lim, Y. J., Xu, Q., Beattie, L., Gardiner, E. E., Gaus, K., ... & Lee, W. M. (2020, May). "Raster Adaptive Optics for Video Rate Laser Scanning Microscopy with Large

Field of View Correction". In CLEO: Advanced Microscopy (Accepted). Optical Society of America. (**Chapter 3**)

2. **Li, Y.**, Huang, H. M., Burgio, G., Heath, W., & Lee, W. M. (2017, April). "Dynamic control over field of view in polygon mirror-based laser scanning multiphoton microscope". In Bio-optics: Design and Application (pp. BoTu3A-2). Optical Society of America. **(Chapter 4)**
3. **Li, Y.**, & Lee, W. M. (2016, December). "PScan 1.0: flexible software framework for polygon based multiphoton microscopy". In SPIE BioPhotonics Australasia (Vol. 10013, p. 1001333). International Society for Optics and Photonics. **(Chapter 2)**
4. **Li, Y.**, Brustle, A., Gautam, V., Cockburn, I., Gillespie, C., Gaus, K., & Lee, W. M. (2016, December). "High speed multiphoton imaging". In SPIE BioPhotonics Australasia (Vol. 10013, p. 100130K). International Society for Optics and Photonics. **(Chapter 2)**

Patents

1. **Li. Y.**, Daniel Lim, & W. M. Lee (2019). "Raster Scanning Adaptive Optics". Patent pending. **(Chapter 3)**

Contents

List of Figures

List of Tables

Nomenclature

[Intravital Microscopy:	IVM]
[Green Fluorescence Protein:	GFP]
[Positron Emission Tomography:	PET]
[Magnetic Resonance Imaging:	MRI]
[Optical Coherence Tomography:	OCT]
[Widefield Microscope:	WF]
[Total Internal Reflection Microscope:	TIRF]
[Stimulated Emission Depletion Microscope:	STED]
[Photoactivated Localization Microscope:	PALM]
[Stochastic Optical Reconstruction Microscope:	STORM]
[Electron Microscope:	EM]
[Adaptive Optics:	AO]
[Raster Adaptive Optics:	RAO]
[Intravenous Injection:	IV]
[4’6-diamidino-2-phenylindole:	DAPI]

[Quantum Dots: QD]

[Quantum Yield: QY]

[Genetically Encoded Calcium Indicators: GECI]

[Signal to Noise Ratio: SNR]

[Swept Confocally Aligned Planar Excitation: SCAPE]

[Förster Resonance Energy Transfer: FRET]

[Fluorescence Lifetime Imaging: FLIM]

[Two-photon Absorption: TPA]

[Second Harmonic Generation: SHG]

[Point Spread Function: PSF]

[Full Width at Half Maximum: FWHM]

[Multiphoton Laser Scanning Microscope: MPLSM]

[Photomultiplier Tube: PMT]

[Avalanche Photodiode: APD]

[Electron Multiplying Charge-coupled Device: EMCCD]

[Spatial Light Modulator: SLM]

[Deformable Mirror: DM]

[Acousto-optic Modulator: AOM]

[Digital Micromirror Device: DMD]

[Frames per Second: FPS]

[Galvanometer Mirror: GM]

[Shack-Hartmann Wavefront Sensor:	SHWS]
[Adaptive Optics Element:	AOE]
[Electro-optic Modulator:	EOM]
[Volume per Second:	VPS]
[Acousto-optic Deflector:	AOD]
[Phosphate-buffered Saline:	PBS]
[Half Wave Plate:	HWP]
[Giant Unilamellar Vesicle:	GUV]
[Peak to Valley:	PV]
[Root Mean Square:	RMS]
[Radius of Curvature:	RoS]
[Graphical User Interface:	GUI]
[Spatial Bandwidth Product:	SBP]
[Analogue to Digital Converter:	ADC]

Chapter 1 Introduction

This chapter serves as an introduction to optical microscopy. I will provide an overview of fluoresce microscope technique, especially focus on the multiphoton absorption and its application in microscopy. First, I will give a general discussion of the development history of fluorescence microscopy, with a description of different labelling chemicals and techniques, including *in vivo* imaging microscope and the corresponding animal models. Then I will introduce the multiphoton absorption effect and tissue optics. Lastly, the implementation of multiphoton microscopy is being discussed.

1.1 Motivation

The field of life science is profoundly influenced by bioimaging methods [1]. Upon using an optical microscope made by curved lenses [2], the cell had been found by just watching a piece of cork (AD 1665), which opened up the door to modern biology. With evolved radiation sources, X-ray, double helix structure of deoxyribonucleic acid (DNA) had been mapped in 1952 [3], which deepened our understanding of life from the cellular level to the molecule level. Now, the advent of cryo-electron microscopy is resolving protein with an unprecedented atomic level in aqueous medium [4], thus to further understand the function and mechanism at the nanometre scale. However, high-resolution imaging in living specimens, especially at the whole animal body level, remains a grand challenge [5].

Among the many biological imaging systems that we have today[6, 7], optical microscope imaging tools, coupled with fluorescence labelling, is a definitive tool to study living cells owning to its non-invasiveness, rapidness, and broad observation ranges from cellular to sub-cellular scale[8]. Efforts have been made to circumvent the optical diffraction limit, hundreds

of nanometre, to achieve better resolution of tens of nanometres, as what electron microscope can do [9-11]. These processes, however, are often viewed in fixed samples that exclude dynamics events. The spread of imaging size-scales across macro-micro-nano can only be bridged by employing an assortment of imaging tools, as shown in Figure 1-1. Figure 1-1 a) shows the distribution of scale size ranging from green fluorescence molecule (GFP) to organelles of sub-cellular structure and single-cell level in organs. In Figure 1-1 b), a comparison of temporal and spatial resolution among the different bioimaging tools are displayed. The imaging tools here for comparison are positron-emission tomography (PET), magnetic resonance imaging (MRI), optical coherence tomography (OCT), widefield microscope (WF), total internal reflection fluorescence microscope (TIRF), stimulated emission depletion microscope (STED), photoactivated localization microscope (PALM), stochastic optical reconstruction microscope (STORM) and electron microscope (EM).

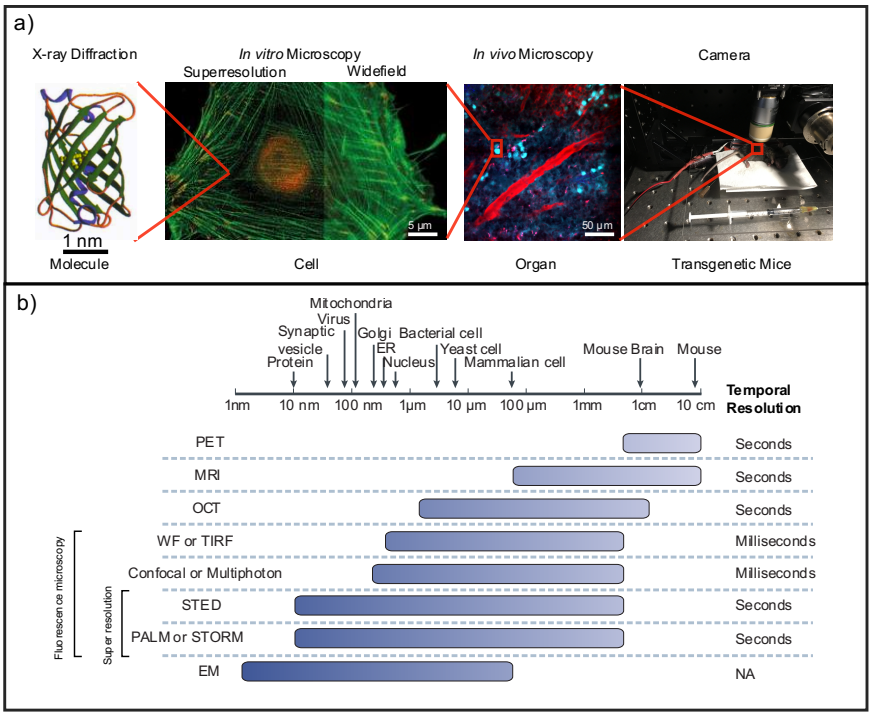

Figure 1-1 Comparison of biological imaging techniques. a) Pictures of different scales, with increased resolution, from the macro size of mouse image during the intravital imaging experiment, to cell level fluorescence *in vivo* image of the organ, to *in vitro* subcellular level of organelle imaging, and molecule level of GFP image by X-ray diffraction. b) The scale of biology creatures and the imaging resolution of different imaging tools. Adapted from [12] and [13, 14] with permissions.

From the quantitative comparison in Figure 1-1, optical microscopy (OCT, WF, TIRF, confocal, multiphoton, STED, PALM/STORM) can be seen to have the broadest range of spatial resolution along with the fastest speed comparing to other bioimaging techniques. A key component of modern optical microscopy is fluorescence labelling, which allows selective imaging of individual molecular activities in living cells and animals. Besides, the combination of fluorescence labelling and laser scanning microscopy [15], afforded the optical microscope with single-molecule sectioning at its native microenvironment [16-18].

While the impact of fluorescence microscopy has been nothing short of revolutionary, there are still many technological challenges that prevent real-time volumetric imaging in living animals. Efforts in mapping molecular activities in living animals with elucidating macroscopic biological events at the suitable temporal resolution, the field of view (FOV) and low phototoxicity are being made. However, there are limited microscopes systems [19] that can achieve this goal. From now on, this thesis is for the target of designing and building an intravital optical microscope, which has multimodalities of both imaging and manipulation, flexibilities in imaging speed and FOV, as well as imaging optimization (adaptive optics).

Chapter 1 is the introduction of fluorescence microscopy, especially multiphoton microscopy. Chapters 2 to 4 are the detail of the development of an advanced microscope system. In particular, I will describe a high contrast flexible multiphoton microscope system using a polygon mirror. The increase in pixel resolution tailored with the speed control over the polygon scanning system provided a controllable means for designing imaging parameters in real-time (> 5 FPS). Customised microscope system software named PScan that is engineered for polygon mirror system will be elaborated, which lays the software foundation of this thesis. Using high-speed imaging system for *in vivo* studies is often impeded by refractive index heterogeneity causing inferior beam focusing in biological tissue. In chapter 3, I shall discuss the use of multiplexing adaptive optics (AO) to achieve real-time aberration correction within a polygon laser scanning multiphoton microscope, named raster RAO (raster AO). As biological events occurred at volume and light tissue interaction will be a tool to stimulate specific biological reactions. In Chapter 4, I will discuss the direct phase modulating by a deformable mirror for high-speed volumetric imaging and the use of amplitude modulation

techniques through a single binary slit with a triplet mirror-conjugate system to perform site-specific fluorescent recovery after photobleaching (FRAP) and laser induced thrombus study.

Finally, in Chapter 5, I shall provide a summary of main achievements and describe potential enhancement in terms of the polygon microscope, and its corresponding biological applications. Overall, this thesis forms the basis for the development of the next generation of volumetric polygon laser scanning AO microscope. In the remaining part of this chapter, I will provide a historical and technological overview of fluorescence optical microscopes, including fluorescence labelling technique and the development of optical microscope both for *in vitro* and *in vivo* study. Then in the middle section, there will be a discussion on the multiphoton absorption and tissue optics. The last part will be the implementation of a multiphoton laser scanning microscope system.

1.2 Fluorescence Microscope

Antonie van Leeuwenhoek, a tradesman, was believed the first man to use a home-made spherical lens (portable microscope) to observe living cells in action (AD 1635) and drew intricate details over these microorganisms. At almost the same period, Christiaan Huygens proposed his wave theory of light in 1690 in his book *Treatise on Light*. The wave theory later was further developed by Thomas Young in a double-slit interference experiment in 1803 and Augustin-Jean Fresnel for the diffraction explanation in 1818. Using the theory of light, in 1837, German physicist, Ernst Abbe first put forward the limitation boundary of resolution that a microscope can achieve, which equals $\lambda/2NA$, λ is the wavelength of the illumination light, NA is the numerical aperture of the objective lens. This equation is now known as the diffraction limit. The cumulative knowledge of "micro-discovery" and physics of light is perhaps the birth of interdisciplinary research of optical microscopy. Many of the concepts that are used until this day.

The development of the modern microscope heavily relies on the ability to engineer illumination patterns or scanning systems to improve the imaging resolution in both space and time. For illumination, a traditional brightfield microscope system requires an illuminating

uniform field that is transmitted directly onto the sample either via trans-illumination or epi-illumination. Kohler illumination describes a set of optical arrangements that ensures partial coherence of the illuminating field that is necessary for the high contrast imaging, such as phase contrast [20], differential interference contrast [21] and Hoffman contrast [22]. Fluorescence imaging typically uses epi-illumination where the objective lens act as light collectors and illuminators.

In fluorescence imaging, the emitted light is of a different optical wavelength to the illuminating light, more typically known as the excitation source. The shift in optical frequency via absorption was first formulated by George Strokes in 1852, who analyzed the effects of fluorescence. The emission wavelength was shown to be always longer than the excitation wavelength, now known as the Strokes shift [23]. In 1911, Reichert and Heimstädt made the first fluorescence microscope [24] which is now routinely used in measuring antibody labelling and protein labelling for biology specimens. However, until then, all the excitation sources were made up of broadband UV sources. It was until the inception of laser and the integration of laser technology with microscopes that pushed the limits of imaging performance. Laser-based microscopy techniques possess the ability to localize a single illumination to a few femtoliters in volume, which allows high-resolution optical sectioning. This tiny focus can be used to stimulate specific fluorescence labelling in cells and provide high contrast images. Using modern super-resolution methods, one can track and monitor of single-molecule at high speed using localization microscopy [9, 10]. The historical development has been drawn up in Figure 1-2, to show the evolution of fluorescence microscopes history over several milestones > light microscope > fluorescence microscope > LASER > confocal microscope and light sheet microscope >super-resolution fluorescence microscope, e.g. STED.

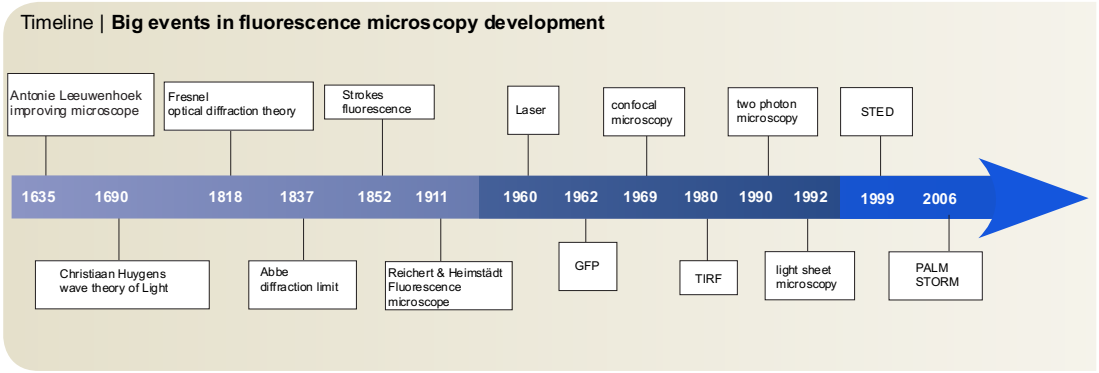

Figure 1-2 Timeline of fluorescence microscopes development. The arrow indicates the years of significant events in the fluorescence microscope. Selected events are on the rectangular shape zone. The figure is adapted from [12] with permission.

1.2.1 Fluorescence Labelling

The selective fluorescent staining allows the study of biomolecular interactions both inside the live cells and the living organs [25]. An ideal fluorescent probe should have a high quantum efficiency (the conversion rate from photons to fluorescence); wide enough spectral distance between absorption and emission wavelengths; short fluorescence decay time (~ns) for high dynamic events [26]; minimal disturbance to avoid affecting the object; large extinction coefficient with high photostability; and highly specific labelling target [27].

The fluorescent labelling technique can be characterized according to the tagging methods being used [28, 29]. In terms of imaging application scenarios, they can be divided by *in-vivo* labelling either through trans genetic fluorescence protein or by intravenous (IV) injection dye [30], and *in-vitro* labelling of targeting components of cells out of the body in the culture environment. More specifically, the tagging method is based on the chemically binding of fluorescent molecules (fluorophores) to a specific region or functional group of targets, including fluorescent protein fusions, fluorescent unnatural amino acids, *in situ* chemical labelling and fluorescent antibody labelling.

1.2.1.1 Fluorophores

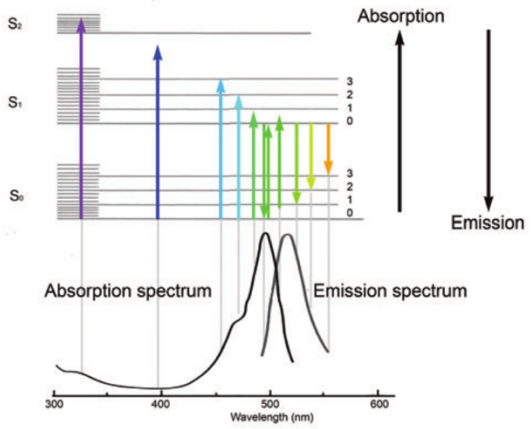

Figure 1-3 Jablonski Diagram. The band structure of fluorophores determines the absorption and emission spectrum. The lines of fundamental (S0) and two electronic excited states (S1, S2) denote the vibrational degeneracies states. The figure is adapted from [31] with permission.

A fluorophore is a molecule that emits fluorescent light [31]. This type of molecule has an electronic structure that can be stimulated by absorption, and when the excited electrons jump back to its base state, the change in energy state results in the emission of a photon whose energy is equivalent to the difference of the electric potential. Electronic energy diagrams are used to explain this excitation and emission process, which is first proposed by Alexander Jablonski (1930) [32]. This process is illustrated in Figure 1-3. It displayed the electronic energy states of the fluorophore molecule. In which the electronic states are labelled as S_0, S_1, and S_2. In which, S_0 denotes the ground state, S_1 and S_2 denote the excited states, respectively. For each of the electronic state, there are also vibrational degenerate states represented by different orbital lines. The energy difference between the orbitals determines the light's wavelength. Also noted that in each energy state, different levels of energies are noted by numbers.

The development of fluorescent probes has allowed a broad range of visualization from molecules to cell-signalling events and subcellular organelles, as well as system-level organs. There are several widely used fluorophores for different wavelength bands. Their emission and

excitation parameters are listed in Table 1.1. One of the most widely used fluorescent protein is GFP, which is based on the luminescent protein aequorin, a protein molecule first isolated from the jellyfish by Osamu Shimomura in the 1960s. GFP emits bright green fluorescence under the illumination light with blue to ultraviolet spectrum [38].

Immunofluorescence is one of the most widely used fluorescent tagging methods through binding to specific ligands (antibody-conjugation). A widely used antibody conjugate is called integrin alpha chain 2b, also known as CD41, which has been applied to conjugate to different fluorophores like FITC or Alexa Fluor, for coagulation labelling to platelet or stem cells.

Fluorophore molecules can also be stained with the specific area of sample tissue by binding. For example, 4'6-diamidino-2-phenylindole, also known as DAPI, has been used as DNA tagging fluorophores, because it becomes more fluorescent when bound to the minor groove of DNA thus to be able to label the nuclei of target cells in a very stable state [33]. DAPI has maximum absorption at 358 nm wavelength and maximum emission of 461 nm (blue) when stains to double-helix DNA, therefore, it can be used together with other fluorophores like GFP to get multiple color labelling.

The labelling methods mentioned above are either at the cellular level or subcellular level. Another labelling solution for vasculature identification is by injecting dyes into the blood circulation. Dextran, a sugar molecule that can be resolved in water and also conjugated to different dyes like rhodamine and FITC, had been widely applied to intravital in vivo imaging through IV injection [34]. Dextran dyes are famous in providing blood vessel contrast in the intravital imaging study and with different molecular weight (kDa) can be used to study tissue permeability.

Instead of organic dyes, fluorescence microscopy uses inorganic dyes for illuminance as well. Currently, the fascinating inorganic dyes are quantum dots (QD), made by tiny particles of semiconductor material, which only have a diameter of 2 -10 nanometres [35, 36]. The structure schematic of representative organic dye GFP and inorganic dye QD are shown in Figure 1-4 b), which has a semiconducting inorganic core and shell with organic coatings and ligands. QD is classified as zero-dimensional nanostructure because of its ultra-tiny sizes (less

than 100 nm), composed by semiconductor materials of CdS, CdSe or ZnS with discreet quantized energies. QD has very sharp emission wavelength with a bandwidth of only a few nanometers, and a wide range of absorption spectrum with high quantum yield (QY). These features improve the sensitivity and resolution of fluorescence microscopy. Therefore, if the polydispersity can be well controlled, QD is an ideal probe for two-photon microscopy because it has an extensive absorption cross section.

Because of QD's unique advantage of high brightness and long-term photostability, it has been applied to quite a few biological studies such as labelling and tracking of individual glycine receptors in living cells [37]. For example, it has been applied to cell imaging as immunofluorescence labelling and live-animal vascular imaging by solubilization and functionalization preprocessing [37]. The current limitation is its cytotoxicity but can be controlled with an optimised concentration of using.

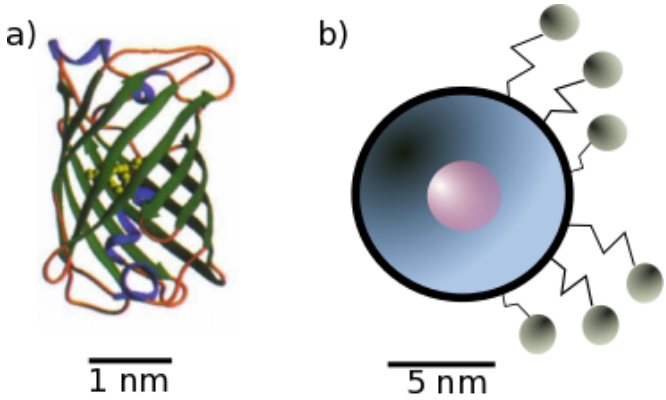

Figure 1-4 Structure of organic dyes and inorganic dyes. a) Reconstruction image of GFP, where chromophore is running through the centre of beta-barrel structure with pleated sheet arrangement. Adapted from [13] with permission. b) Schematic diagram of QD dyes. The red centre is an inorganic core, surrounded with inorganic shield and aqueous organic coating, with conjugated biomolecules for a specific function.

Although fluorescent particles are easy to use, there are limitations for intracellular tagging and is less preferred for *in vivo* animal studies. In order to solve this problem, fluorescent protein has been introduced, which can be used in labelling specific cells in live animals by modifications of genes.

1.2.1.2 Fluorescent Protein

One of the most widely used fluorescent protein is GFP, which is based on the luminescent protein aequorin, a protein molecule first isolated from the jellyfish by Osamu Shimomura in the 1960s. GFP emits bright green fluorescence under the illumination light with blue to ultraviolet spectrum [38]. The advantage of GFP is that it has a high fluorescence QY of 0.79 with a single emission peak at 509 nm. In addition to this, GFP is easy to be modified and is stable in the form of an internal chromophore, which makes it an essential tool as expression reporters and biosensors in cell and molecular biology [39].

Multiple derivative fluorescent proteins have been developed based on the GFP, such as enhanced GFP (EGFP), which enabled the utilization of GFP in mammalian cells with QY as 0.6 [40]. Another important GFP derivative is genetically encoded calcium indicators (GECI). The representative one is called GCaMP 6. GCaMP 6 is created by combining GFP, calmodulin and peptide sequence called M13 [27, 38, 41, 42]. This protein label is specified designed for expressing fluorescence signals in the mammalian body by transgenic engineering, making it an essential tool in live animal imaging, especially in neurology study as calcium indicators [43, 44].

There are also other specific biosensors for tracking and labelling target proteins in the study of cell interaction and signal pathway [45]. For example, the use of genetically engineered mice with biosensor for Förster resonance energy transfer (FRET) and fluorescence lifetime imaging (FLIM) facilitates the study of the pancreatic cancer progression and metastasis [46]. Despite these improvements in labelling technique, in order to adequately detect the signal with the demand contrast and resolution, corresponding design and optimization of microscopes are also important, especially in the case of *in vivo* studies, where it is a low-light imaging condition where the fluorescence signal is weak. In the next section, I will start to introduce several modern fluorescence microscopes that are widely used for live animal imaging.

Table 1.1 – Comparison of commonly used fluorophores, includes properties of wavelength, labelling, and tagging methods [47, 48].

Fluorophore	**Excitation 1p/2p (nm)**	**Emission (nm)**	**Common Labelling**	**Common Tagging**
FITC	490/780	525	IV injection	Dextran Conjugation
Rhodamine	510/840	615	IV injection	Dextran Conjugation
GFP	488/800~850	516	Transgene	Protein
eGFP	488/900~950	516	Transgene	Protein
GCamp6	497/920	512	Virus injection	Protein
Quantum Dots	Design specific	Design specific	IV injection	PEG functionalised

1.2.2 *In vivo* Fluorescence Microscopy

Comparing to microscopes which can only work with cells out of the tissue, e.g. TIRF [49] and super-resolution microscope [50], microscopes for live animal imaging, will provide more completed information of how cells communicate and collaborate. In terms of animal experiment, there have been quite a few animal models being genetically engineered to answer a specific biological question, from worm to fruit fly, fish and mouse, and even primate. For example, the drosophila has played an important role in gene study since its gene model has already been fully deciphered. However, to answer more complex questions in the mammalian system, such as cell communication, cell signalling, microenvironment, a trend is using more and more complex mammalian animals as research models. In this case, the intravital microscope (IVM) with deeper penetration depth is demanded. Until now, the traditional confocal and two-photon microscope are still the major choices of intravital microscope due to

its easy access and broad working range with different fluorophores. In order to get fast volumetric imaging and less photodamage, light sheet microscopy, e.g. selective plane illumination (SPIM) [51], swept confocally-aligned planar excitation (SCAPE) [52] and lattice light sheet [53], had been put forward, with less photobleaching due to its thin planar feature. Despite the advantages in speed and photobleaching, most types of light sheet microscope cannot be used for small animals (e.g. mice, rats) due to the physical constraints of the orthogonal arrangement of illuminating lens and imaging objective lens arrangements. The comparison of animal model sizes and microscopes working range are shown in Figure 1-5.

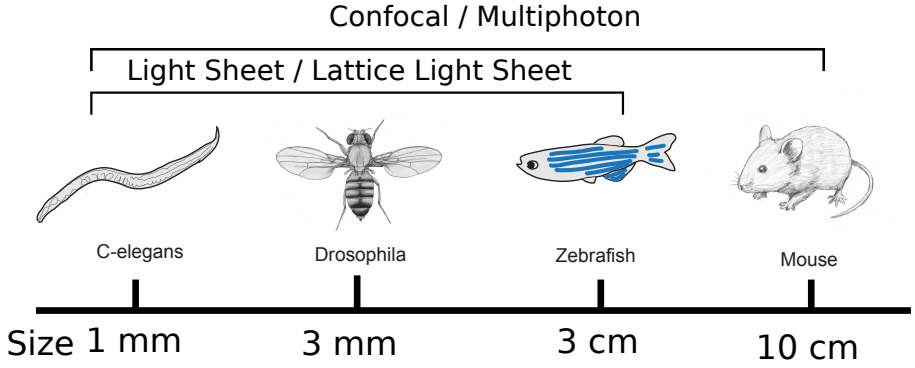

Figure 1-5 Animal Model. The animal model widely used in biological research, from small size to big size. Pictures are adapted from [54], [55] and [56].

Figure 1-6, a) shows the different implementation of light sheet techniques; SPIM light sheet, which uses two objective lenses to generate light sheet illumination and detection in orthogonal angle [57]. b) is the SCAPE microscope, which uses one objective lens to achieve both illumination and detection with oblique angles [52]. c) is the schematic of lattice light sheet, instead of a single light beam sheet, interference thinner lattice beam is used to enhance the resolution.

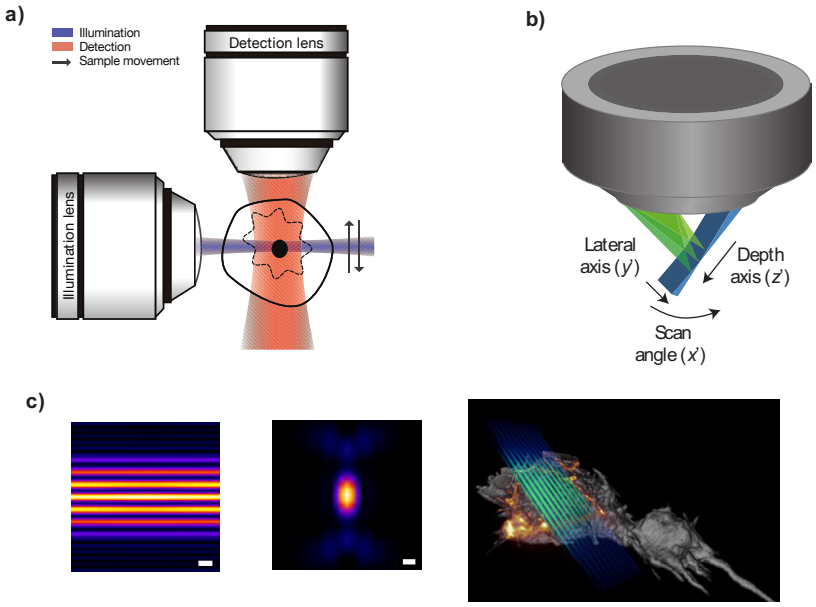

Figure 1-6 Optical sheet scanning plot. a) The light sheet scanning microscope. Adapted from [57] with permission. b) The SCAPE scanning microscope, adapted from [52] with permission. c) The lattice light sheet microscope, adapted from [53] with permission. From left to right are generated lattice light sheet beam at the image plane (xz plane), detected point PSF from the imaging objective lens (xz plane), and the schematic illustration of lattice light sheet working scenario with a biological specimen. Scale bars are 1 μm in image plane figure and 200 nm in the PSF measurement figure.

For large organisms such as mice, confocal and multiphoton microscopes are the prime tool for observation. The confocal microscope, proposed by Minsky's 1961 patent [58], is first demonstrated in 1969 after the invention of the laser, which can confine light at a point with high optical coherence [59]. The confocal microscope uses a pinhole to block out the out-focus light for enhancing the signal to noise ratio (SNR), which is crucial to fluorescence labelled biological samples with strong scattering. Confocal has achieved optical sectioning ability with unprecedented contrast comparing by laser point scanning, but it also retains to slow imaging rate and high photobleaching/phototoxicity risk as well as limited penetration depth with thick tissues. In order to solve these problems, an effort of a spinning disk with wide-field detector has been introduced, which improved the imaging speed to the video-rate speed. However, the signal cross talking is worse, comparing to the point scanned confocal.

In order to further increase the imaging penetration depth, the multiphoton microscope was invented by Denk and Webb in 1990, which is essentially a laser scanning microscope that uses ultrashort laser pulses [60]. The benefits of ultrashort laser pulses are the compression and concentration of light both in time and space for achieving multiphoton absorption, which would only occur at the focus of the laser beam - inherent depth sectioning. Denk and Webb used the same confocal laser scanning system without pinholes for depth sectioning. This means that all the emitted photons can be collected with improved detection sensitivity to weak signals. Due to the infrared wavelength laser source and widened absorption bandwidth, multiphoton microscopy retains the capability of deeper depth imaging and simultaneous excitations of multi-fluorophores.

In summary, currently, most of the IVM are used in preclinical instead with limited trials on the human as a diagnostic tool. In the next part, I will introduce the detail of multiphoton effect and tissue optics, including the principle of multiphoton effect, the interaction of photon and tissues (absorption and scattering). A basic configuration of the multiphoton microscope setup will be described in the last section of this chapter to provide context for instrument development for later chapters.

1.3 Multiphoton Absorption

The multiphoton effect is a nonlinear absorption phenomenon. It assumes that the one molecule can absorb several photons at the same time (10^{-15} s). The concept of photon comes from Albert Einstein in 1905, in his explanation of the photoelectric effect. He first argued that the energy of light is discrete, as

$$E = h\nu, \qquad \text{Equation 1-1}$$

where E denotes energy, h denotes Planck constant and ν is the frequency of light. This theory is complementary to the electromagnetic wave theory and greatly expanded the quantum energy idea proposed by Max Planck. Later, after the photon concept is built, two-photon absorption (TPA) was predicted by Maria Goeppert-Mayer in 1931 in her doctoral dissertation,

in which she investigated the consequence of concentrating photons in space and time theoretically [61].

Soon after the invention of laser (1960), the first observation of two-photon fluorescence was in crystal in 1961 by Kaiser and Garret [62]. Then in 1970, three-photon fluorescence was observed by Rentzepis [63]. Until 1990, the first 2-photon absorption laser scanning microscope (TPLSM) was invented by Denk and Webb [64] after the invention of femtosecond laser, which is an integration application of a femtosecond laser with high numerical aperture optics. Later, Xu developed the first 3-photon microscopy with longer wavelength [65]. This history of the multiphoton technique is shown in Figure 1-7.

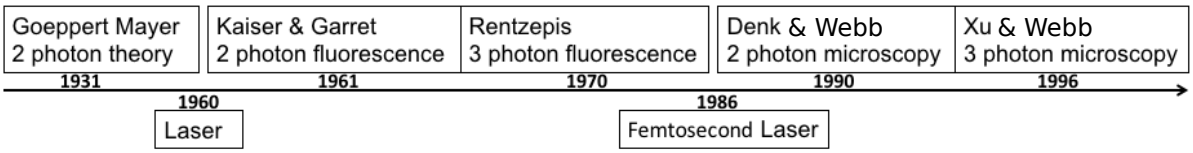

Figure 1-7 History of multiphoton effect and the applications. Directly related milestones of multiphoton effect are presented on the top of the time axis, below the time axis is the technical development which facilitated the multiphoton absorption development.

The schematic diagram of multiphoton absorption is shown in Figure 1-8. In which, the electron at the ground state (S_0) is stimulated to the excited electronic state (S_1) in the case of two photons come at the same interval. After a short time (fluorescence lifetime, ~ ns), this stimulated electron will relax back into the ground state with an emission of a fluorescence photon, whose frequency of light equals to the ratio between the energy difference and the Planck coefficient.

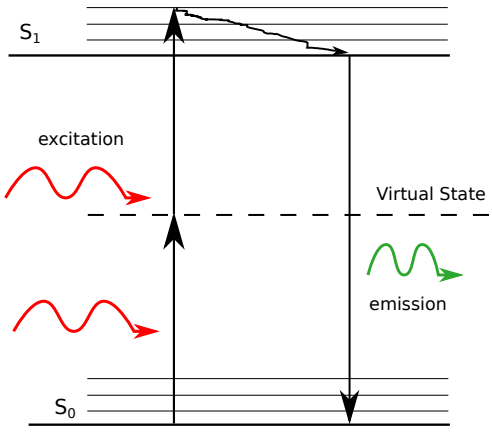

Figure 1-8 Schematic diagram of two-photon excitation process. S_x denotes energy states.

This absorption process is a nonlinear process, which has a square dependence on the power of light. As illustrated in Figure 1-8, TPA requires two photons arrived at the same time to stimulate the emission of a single fluorescent photon. Therefore, the dependence of TPA is based on the intensity of light with an exponential index of 2. The nonlinear relation of polarizability and the electric field is

$$P(t) \cdot E(t) = \varepsilon_0(\chi^1 E(t) + \chi^2 E^2(t) + \chi^3 E^3(t) + \cdots) \cdot E(t), \quad \text{Equation 1-2}$$

where P is dielectric polarization density (C/m^2), χ^n is the n-order susceptibilities of the medium, E is the electrical field of the input light. The second-order term in this equation is related to the second harmonic generation (SHG) [66]. SHG has been used as an imaging method for studying cells and tissue with nonsymmetric structures, like collagen, skeletal muscle and microtubules [67]. TPA is a third-order effect, considering the light intensity (I) is a Poynting vector, $E \times H$ (H denotes the magnetic field), therefore for a squared light field intensity, the total light intensity will be $I \propto E^4 \propto [\chi^3 E^3(t)] \cdot E(t)$, which has a third-order susceptibility term.

The TPA probability is related to the squared of laser intensity and two-photon cross section as

$$P_{TPA} \propto I^2 \delta_{TPA}, \quad \text{Equation 1-3}$$

where P_{TPA} denotes the TPA probability, I denotes the laser intensity, δ_{TPA} denotes the TPA cross section. This equation demonstrates that in order to increase the TPA probability, cross section of the molecule and the light intensity are the two parameters that need to be considered. For the molecule parameter, cross section is a physical quantity representing the chance of absorption event. In TPA, this cross section has a unit as Goeppert-Mayer (GM, 10^{-50} cm^4 • s/photon). The TPA cross section of various molecules and compounds over a range of stimulation wavelength had been measured by Xu and Webb [68], including rhodamine B, fluorescein and DAPI. For the light intensity, this is related to the NA of the objective lens and the peak power of the laser, which has a relation as

$$P_{peak} = {P_{average}}/{f\tau}, \quad \text{Equation 1-4}$$

where P_{peak} denotes the peak power of the laser, $P_{average}$ denotes the average power, f denotes the laser repetition frequency, and τ denotes the pulse duration. The dimension of two-photon absorption PSF can be obtained as

$$\omega_{xy} = {0.325\lambda}/{\sqrt{2}NA}, \quad \text{Equation 1-5}$$

$$\omega_z = {0.532\lambda}/{\sqrt{2}}\left[{1}/{n - \sqrt{n^2 - NA^2}}\right], \quad \text{Equation 1-6}$$

where *n* denotes the refractive index of immersion material. The PSF function of TPA is

$$PSF_{TPA} = [I(x, y, z)]^2 \approx PSF\left(\frac{\nu}{2}, \frac{\mu}{2}\right), \quad \text{Equation 1-7}$$

where ν, μ are the normalized optical coordinates with relation as [69] $\nu = k(NA)\sqrt{x^2 + y^2}, \mu = k(NA)^2 z$. The half coordinates indicate that TPA has longer stimulation wavelength with spatially more confined PSF due to quadratic dependence of the light intensity comparing to the single-photon absorption as shown in Figure 1-9.

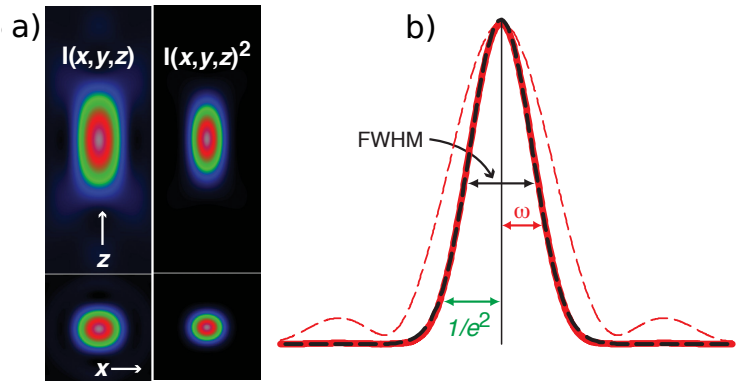

Figure 1-9 PSF comparison between linear and nonlinear absorption. a) The simulated PSF image in axial (xz) and lateral (xy) plane, with linear intensity absorption and square intensity absorption, respectively. The squared absorption leads to more localized PSF with minimal side lobes. b) Axial profile of the PSF. The dashed red line is the linear absorption PSF, while the solid line is the TPA PSF, dashed black line is the Gaussian curve fit plot. This figure is adapted from [70] with permission.

1.4 Tissue Optics

The above analysis of the TPA effect is under the ideal condition without considering the tissue of samples. The tissue is not imperious to the light. The light will be distorted by different types of interactions, which are scattering and absorption [71]. The study about the interaction and behaviour between light and tissue is known as tissue optics. Here in this subchapter, I shall discuss the tissue optics with a focus on scattering and absorption effect during the multiphoton imaging process.

Optical scattering is the dominant effect in a lot of light-matter interactions, especially in biological tissue, where the level of scattering determined the achievable imaging depth. Hence, the ability to analyze about how light wave is propagated in inhomogeneous media would provide novel tools for imaging applications [72], for example, the using of the coherence of single scattered reflected light given rise to the invention of optical coherence tomography (OCT), which has been mostly used in ophthalmology studies [73]. Scattering effect will make the photon to be away from the target region, generating blurred and opaque

images. However, for the diffused photons from the tissue, the interactions in the tissue will be useful, because the light scattered would bear the information of the structure of the tissue. For instance, optical diffusion tomography is based on the multiple-scattering effect [74]. The interactions between the atmosphere and the photons result in blurring of the image received by the telescope. The effort of compensating this distorting lead to the invention of the AO technique [75].

However, the interaction of light with biological tissue is far more complicated due to increased inhomogeneous biological tissues with multilayered and sophisticated structures. In general, the effects of light-tissue interactions can be classified as reflection, refraction, absorption, and scattering [76]. Among these, reflection and refraction occur as the incident light travels across the medium of different refractive index. The Absorption of photons determines the the penetrate depth of corresponding tissues. Absorption is wavelength dependent and is crucial in the photon dynamics therapy [77] and fluorescence microscope. Optical scattering is significant because of the mismatch of the refractive index between different mediums and the resulted in increased optical path length difference [78]. Absorption and scattering of photons will introduce the dispersion of light pulses and path delay during the propagating through tissues. These light tissue interaction processes also include other effects, like thermal coagulation and acoustic waves, as shown in Figure 1-10 [79]. These interactions are essential in designing and implementing diagnostic and therapeutic applications. For example, the photoacoustic signal can achieve high contrast imaging in depth of centimetres [80]. In the next paragraph, I will introduce the process in more detail and give some application examples.

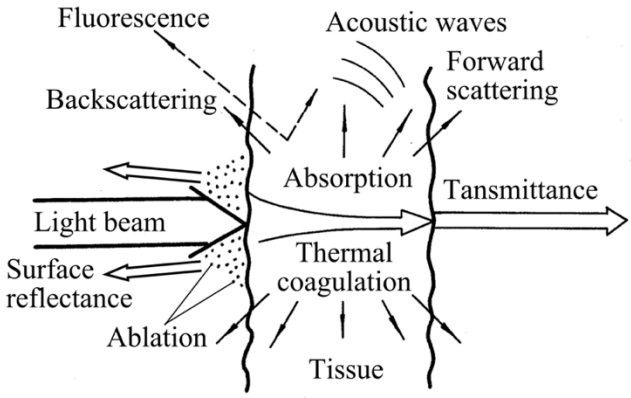

Figure 1-10 Tissue interaction phenomenon. A collimated light beam incident and interact with the tissue, several phenomena are being illustrated, part of the light is going through the tissue as transmittance and forward scattering, part of the light has been reflected back as surface reflectance and back scattering. Part of the light will be absorbed by the tissue to introduce several effects, like fluorescence, thermal coagulation, and acoustic waves. This figure is adapted from [79].

1.4.1 Absorption Effects

Photon absorption is a process that the light energy is converted into the molecule's energy during the propagation through the tissue. The absorption effect can be generally grouped as electronic absorption, vibrational absorption and rotational absorption [81]. The absorption effect is essential both in imaging and therapeutic applications. One of the consequences of photon absorption is the fluorescence process, which has been discussed in the subsection of Fluorescence Labelling in Chapter 1. For therapeutic purposes, the absorption of energy will produce thermal effects for treatment such as laser surgery for wound healing [82].

For a single particle, the absorption effect can be expressed by absorption cross section $\sigma_a = {}^{P_{abs}}/_{I_0}$, where P_{abs} is the value of power (unit time) absorbed out of the optical illumination intensity (unit time and unit area) I_0, so absorption cross section' unit is area. In a medium of uniform distribution of the particle, the absorption effect can be characterized by the absorption coefficient $\mu_a = \rho\sigma_a$, where ρ represents the density of particles. The most critical concept in absorption effect comes out as the reciprocal of the absorption coefficient,

$$l_a = \frac{1}{\mu_a}, \qquad \text{Equation 1-8}$$

in which l_a denotes the absorption mean free path (absorption attenuation length) [71, 78, 83]. This absorption attenuation length (1 μm ~ 10 cm) together with the scattering attenuation, will fundamentally determine the penetration depth of light in tissues.

Tissue absorption properties can be mapped out using optical spectroscopy. Figure 1-11 shows the spectral absorption of light and identifies a spectral range of light known as the therapeutic window, within which most tissues allow a significant penetration with weak absorptions. The dip in the spectrum suggests that there is an exclusive spectrum of optical wavelength between visible (Vis) and near-infrared (NIR). Some of the absorbers' absorption coefficient goes down towards the NIR, indicating that multiphoton absorption is superior in deep tissue imaging because of the longer illumination wavelength.

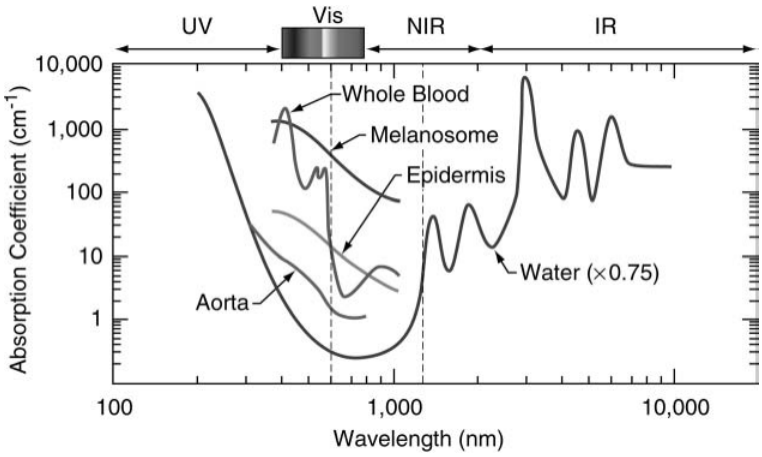

Figure 1-11 The spectrum of absorption coefficients in biophotonics area, image is adapted from [84]with permission requested.

There are studies on the properties of specific tissues. For example, studies showed that DNA, proteins and melanin and haemoglobin have peak absorption on UV light range [71]. For instance, haemoglobin, as a molecule that carries 97% oxygen in the blood, its absorption band (400 ~ 100 nm) will be dependent on its intrinsic oxygen, blood flow conditions, osmotic concentration and haematocrit. Besides, the absorption of tissues must consider the water absorption, because water constitutes a large portion of the body. Water is the dominant

absorber in the spectrum of NIR window. It determines the attenuation of light in multiphoton imaging, especially in brain tissue [65, 85]. In concluding, multiphoton imaging is affected by choice of lasers wavelength being used, which most lasers are centred at 800 nm and 1300 nm for two-photon and three-photon absorption respectively.

1.4.2 Scattering Effects

Another critical effect in tissue optics is scattering, which is mostly about how the photon gets reflected or refracted by the refractive index mismatch. One example is the difference of refraction between subcellular organelles, and surrounding cytoplasm will lead to the scattering of photons. Scattering can be used as a source of contrast for diagnostic and therapeutic applications since the variation of size, morphology, and structure of the tissue will alter the scattering properties [86].

Similar concepts from absorption can also illustrate scattering effects.. Scattering cross section, $\sigma_s = {}^{P_{sca}}/_{I_0}$, where P_{sca} is the amount of power gets scattered, I_0 denotes the intensity of light hitting onto the scatter. Moreover, the tissue can be modelled as a media with uniform distribution of identical scattering particles as $\mu_s = \rho\sigma_s$, where ρ is the density and μ_s is the scattering coefficient. Thus, we will have an equation of scattering mean free length l_s as

$$l_s = \frac{1}{\mu_s}, \qquad \text{Equation 1-9}$$

which is the same as the equation of absorption free length. Therefore, the total attenuation length will be the adding of scattering and absorption with the length l_e as

$$l_e = \left(\frac{1}{l_a} + \frac{1}{l_s}\right)^{-1}. \qquad \text{Equation 1-10}$$

Scattering can be classified as elastic scattering (without energy loss) and inelastic scattering (with energy loss). Inelastic scattering is also known as Raman scattering, which has two types of scattering as Strokes and anti-Strokes scattering corresponding to the photon energy changing direction [87]. Raman is an approximation for particles that are small with

respect to the wavelength. Raman scattering is essential for spectral analysis and has been applied to image single-molecule dynamics [88].

Elastic scattering can be classified as Rayleigh, and Mie scattering depending on the size ratio of the scatters and the frequency of light [89]. For small particles, whose size is less than one-tenth of the wavelength, Rayleigh scattering will become the dominant scattering effect which is proportional to the $1/\lambda^4$ (derived from integrating the scattering coefficient), λ is the illumination wavelength [90]. Mie scattering exists in extensive situations, and it will overwhelm the other scattering effects when the particle size is comparable to the wavelength. Structure of cell components, sub-compartments, and extracellular components are Rayleigh limit. The schematic diagram of these two scatterings is shown in Figure 1-12 [91]. In which, Mie scattering pattern is more in a forward direction along with the light propagation pathway, while Rayleigh is isotropic without preference of scattering direction but only for one single polarization state. At longer illumination wavelength, the scattering is less. Therefore multiphoton microscope has a deeper imaging depth, for example, illumination beam with 800 nm wavelength for TPA will have about a one-tenth scattering of the 450 nm wavelength beam for single-photon absorption, which is one significant advantage of the multiphoton effect.

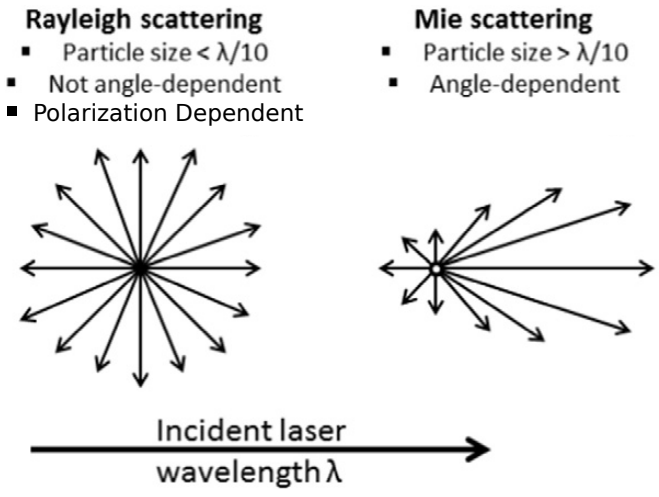

Figure 1-12 Schematic diagram of Rayleigh and Mie scattering. This image is adapted from [91] with permission.

For multiphoton microscopes, which are working at the NIR bandwidth, the so-called "therapeutic window", both scattering and absorption are low. Nevertheless, for millimetres deep imaging, the scattering effect is the primary limiting factor that affected the attenuation of illumination and fluorescence light. Furthermore, the light that penetrates the tissue to generate the nonlinear effect is assumed to be the ballistic light (unscattered). The losing of contrast between the out of focus fluorescence and the perifocal region is the fundamental limit of imaging depth [92]. One way of increasing the depth is modulating the pulse laser to increase the TPA probability. For example, the use of high energy low repetition frequency laser pulses can improve the depth of TPA to 5 times of scattering mean free path [92]. Moreover, another method is the use of the 1700 nm bandwidth light of 3-photon absorption had improved the penetration depth to 1.5 mm depth in brain tissue [93]. On the other hand, there are phase modulation methods that can compensate for optical path length difference in the sample, especially the low order distortion such as refractive index mismatch, AO for phase conjugation correction can cancel out the distortion of light beam thus to refocus back into deep tissues [94].

1.5 Instrumentation

As discussed, the two significant features of TPA are spatially more confined PSF and increased depth of beam travelling in scattering tissues. Therefore, these two features make TPA an ideal method for intravital imaging. Applying the TPA effect to imaging requires scanning the high temporospatial concentrated photons over the target area, called multiphoton laser scanning microscope (MPLSM). MPLSM is similar to the confocal microscope in terms of the architecture of scanning, but for MPLSM, the pinhole is not necessary anymore in the fluorescence detection path, same to the descanning requirement. Besides, in MPLSM design, mirror and lens coatings should be adapted to the NIR wavelength range, and objective with specific chromatic aberration correction should be concerned.

A typical MPLSM setup is shown in Figure 1-13, in which the light source is an infrared femtosecond mode-lock Ti:Sapphire laser, monitored by a spectral analyzer for specific laser tuning. The intensity modulation module usually using EOM to tune the laser power for a

balance between image quality and photodamage. Telescope module will expand the laser beam and then followed by a beam scanner for raster scanning the beam into an area. A high NA objective lens will be used to collect the integrated scattered fluorescence signals then transferred and amplified to electrons by detectors. A current to voltage converter is used to generate a discrete electrical signal which will be binarized by a workstation for displaying them in a time sequence synchronized with the scanners, real-time processing and analysis of the data will be provided with a graphic user interface.

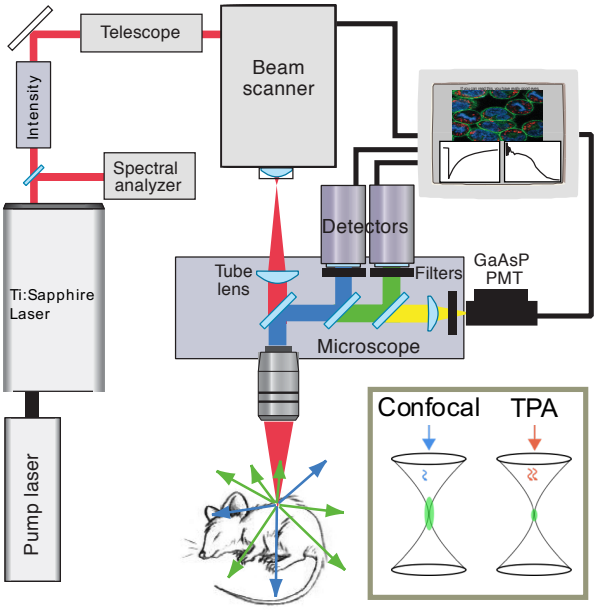

Figure 1-13 Schematic of a general multiphoton microscope for intravital imaging. Adapted from [70] with permission.

1.5.1 Lasers

Light sources used for TPA are mostly by Kerr-lens mode-locking laser with the ability to compress the light in temporal into discrete pulses [95]. Mode locking is a technique that synchronized the phase of laser modes so to compress all the laser modes and generate a pulse with the extreme photon density. The ideal laser source should have a high peak power (~ MW), broad wavelength tuning capability (~ nanometers), and short pulse duration (~ femtoseconds) for minimizing cross-talking of fluorophores [69]. There are quite a few options

of lasers for generating the ultrashort laser pulses, such as dye laser [96] and fibre lasers [97]. Currently, Titanium: Sapphire ($Ti:Al_2O_3$) crystal laser is the most popular choice for multiphoton imaging with its high average laser power capability, broad tuning range, short pulse duration as well as reliable and robust operation [98]. Temporal compensation modules will be required for maintaining the contraction of laser pulses due to the dispersion during the light propagation in microscope setup and imaging tissues [99]. Especially for keeping the ballistic light beam confined after the scattering from the inhomogeneous sample.

1.5.2 Laser Beam Scanners

Scanning devices can be classified as reflection and diffraction devices. Reflection devices include galvanometer mirrors, resonant galvanometer mirrors, and polygon mirrors. While for diffraction devices, it includes spatial light modulators (SLM), acousto-optic modulators (AOM) and digital micromirror devices (DMD). The primary factors that contribute to the choice of scanning devices are scanning speed, scanning angle, scanning accuracy (scanning angle variation per scanning point) and scanning efficiency. The particular properties are shown in Table 1-2 [100]. From the table, the polygon scanner has a full advantage in NA, scanning angle, resolvable scanning pints, velocity, response time and efficiency while comparing to other scanners. The major limitation of the polygon is its scanning area, which is fixed. This fixed scanning area cannot conduct random-access scanning comparing to other scanners. However, through integrated designing with other scanners, a combined system can still achieve the fast switching between raster scanning and random access scanning [101]. The other drawback of the polygon is its relative low scanning accuracy, but through either a passive reflective scanning trigger or an active scanning mirror compensation with a lookup table, the scanning accuracy can be improved. The building and designing of a polygon multiphoton microscope will be presented in the following chapters.

Table 1-2 – Parameters comparison of different scanners [100].

Scanning technology	Aperture [mm]	Max. deflection angle [rad] (Number of resolvable spots N)	Max. velocity [10^3 rad/s] (Rate of resolvable spots N [10^6])	Accuracy [μrad] (Accuracy per resolvable spot [%])	Response time [μs]	Efficiency or Reflectivity
Galvo scanner	7 ~ 30	0.5 ~ 1 (3000 ~ 8000)	0.1 (0.5 ~ 1)	< 2 (< 5)	10^3	> 95%
Polygon scanner	2 ~ 12	0.6 ~ 1 (2000 ~ 7000)	1 ~ 10 (5 ~ 40)	~ 200 (~ 120)	10^3	> 90%
Piezo scanner	10 ~ 25	0.01 ~ 0.1 (100 ~ 1000)	0.01 ~ 0.1 (0.1 ~ 1)	~ 1 (~ 1)	10^3	> 95%
MEMS scanner-static	1 ~ 25	0.5 (200 ~ 1000)	0.1 ~ 1 (0.1 ~ 1)	n/a	10^3	> 90%
MEMS scanner-resonant	1	0.5 ~ 1 (500 ~ 1000)	10 ~ 30 (5 ~ 20)	n/a	10^3	>90%
EOD (Pockels effect)	2	0.001 (2)	2 ~ 20 (3 ~ 30)	~ 1 (~ 0.2)	0.04 ~ 1	>85%
EOD (Kerr effect)	0.5	0.2 (50)	40 (15)	n/a	10	>90%
AOD	1 ~ 10	0.01 ~ 0.05 (10 ~ 500)	5 ~ 250 (20 ~ 80)	0.1 (0.1)	0.5 ~ 15	60% ~ 80%

1.5.3 Objective Lens

In MPLSM, usually, the scanned beam is relayed to the back focal plane (BFP) of the objective lens, for concentration the laser beams with minimal vignette. Since a multiphoton microscope is used mostly for thick tissues that exhibit strong scattering, the detection geometry in a multiphoton microscope is epi-illumination rather than trans-illumination. In epi-illumination, the objective lens will work both as the illumination condensing lens and the fluorescence collection lens. In this case, the objective lens should retain both a large FOV (low magnification) for in terms of collecting efficiency and also high NA for a high-level concentration of the photons. However, a low magnification objective lens will induce a corresponding decreasing in NA, which will degrade the spatial resolution and imaging performance. Currently, only a few commercial objective lenses with specific optimization for MPLSM application are available for usages. The main parameters of the objective lens in multiphoton imaging is 1.0 NA, water immersion, 20x magnification, and specially designed achromatic correction for a broad band of light [102].

1.5.4 Detectors

The detection path design in MPLSM does not require pinhole or descanning geometry. The collection efficiency can be maintained by conjugating the BFP of the objective lens to the sensing area of the detector. Therefore, the ideal detecting devices suited for MPLSM should have enough active area (~mm^2) and high quantum efficiency for collecting the scattered fluorescence signals as much as possible with both high sensitivity and low background noises. There are several detector options for multiphoton imaging, such as wide-field high sensitivity cameras (e.g. electron multiplying charge-coupled device, EMCCD), point detecting devices like avalanche photodiodes (APD) [103] and photomultiplier tubes (PMT). For MPLSM wide-field pixelated detectors with simultaneous multisite stimulation can increase the imaging speed, but the cross talk of signals between pixels will lower image contrast when imaging deep into tissue [104]. APD has superior quantum efficiency (~80%) but tiny sensing area and low internal amplifying ratio followed by the excess noise, which therefore is limited to apply in MPLSM. PMT has comparably large sensing areas, high internal amplification rate and reasonable quantum efficiency (~30%), GaAsP PMT can even have a 40% quantum efficiency. These features make PMT a right choice for fluorescence signal detection [105].

1.5.5 Control and Imaging Electronics

The whole laser scanning intravital microscope will include imaging and controlling electronics as well. A typical setup has been shown in Figure 1-14. A host computer is being used to display the signal obtained from the PMT. The vital part in generating this image is the synchronization of signals to the position of the beams, which will map the acquitted point by point signal sequence into an image. The image can be displayed as 2D images or 3D images by this reconstruction. The gathered information will be saved in and stored by digital hardcopy and backup as well. In addition to image digitizing and video display, this host computer will also be responsible for microscope devices control, such as the controlling of scanning mirrors, stepper motor stages, laser powers, and filter wheels. Together, all these components integrate into a whole system of laser scanning intravital microscope.

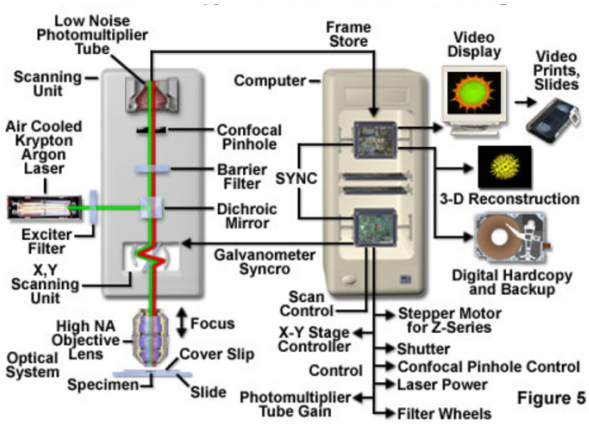

Figure 1-14 Schematic diagram of a laser scanning microscope with control and digitizing parts. The figure is adapted from [106].

1.6 MPLSM – an Integrated Engineering Platform

All in all, IVM system is a highly sophisticated design framework that requires electronics, optics and laser control. To further improve and optimise the MPLSM for reaching versatile biological imaging conditions, some efforts had been tried in terms of instrumentation level. Such as miniature two-photon microscope [107-109], three-photon microscope [93], temporal multiplexing multiphoton microscope [26], large FOV multiphoton microscope (“mesoscope”) [110], Bessel beam multiphoton microscope [111] and AO multiphoton microscope [112]. In the next chapter, I shall explain why beam engineering is crucial in multiphoton microscopy and demonstrate the detail of designing and building of polygon scanner based multiphoton microscope.

Chapter 2 Polygon Based Multiphoton Microscope

In this chapter, I shall primarily centre my discussion on the polygon mirror-based laser beam engineering multiphoton microscope. The first part of this chapter is current existing methods for improving scanning efficiency and speed, include random scanning, multiplexing scanning and volume scanning. Then, the detail of design and building a polygon based multiphoton microscope is demonstrated, followed in both hardware and software aspects. The last part will be the test and application of this customized laser scanning multiphoton microscope, including imaging of beads and pollens, neuron signals measurements of rat brain slices and quantitative blood dynamics study.

2.1 Laser Beam Engineering in Multiphoton Microscope

There are four critical parameters in laser scanning microscopes, which are laser beam's amplitude, frequency, wavefront and location. Mostly modern microscopy techniques are about devising and modifying these parameters to optimize microscopes' outcomes, in which the ability to manipulate the laser beam is crucial for designing and building customized multiphoton microscope.

As discussed at the end of Chapter 1, besides the regular raster scanning multiphoton microscope, a variety of beam shaping techniques had been developed for improving and extending the multiphoton microscope's capabilities, such as spatial resolution, temporal resolution, imaging depth and phototoxicity. However, there is a direct trade-off among these four capabilities, which are induced by the limited budget of photons in the fluorescence microscope [113]. Photon budget means the finite amount of photons generated from limited fluorophore labelling density and detecting time before the photobleaching happens. Therefore,

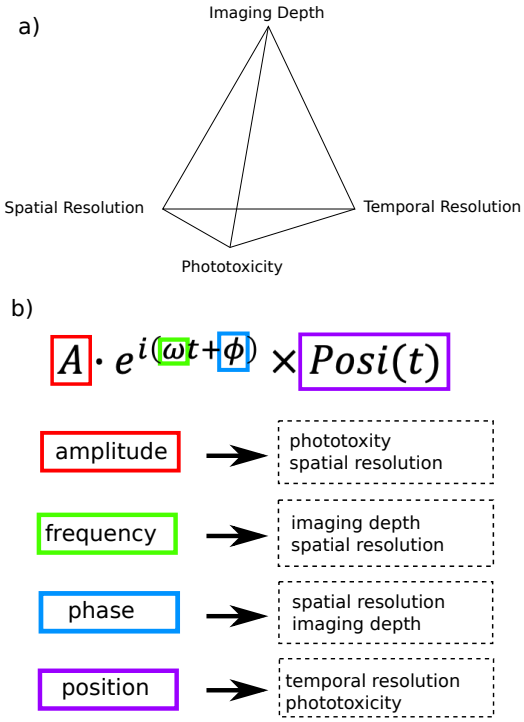

Figure 2-1 Limitation factors and beam engineering of fluorescence microscopy. a) Photon budget pyramid, four constraints are at the four vertexes. b) Light beam engineering function and corresponding potential effects of varying the four constraints in figure a).

the use of laser beam engineering should be balanced with the tradeoffs amongst temporal resolution, spatial resolution, imaging depth and phototoxicity, as shown in Figure 2-1 a). These four parameters are drawn at the four vertexes of a pyramid that constrains the performance limitation it can achieve. The possible beam engineering approaches are demonstrated in Figure 2-1 b), in which the light beam is illustrated as a function of wave multiplied by the time-dependent position function, the four beam factors that can be manipulated are amplitude (power), frequency (wavelength), phase (wavefront) and position (scanning). For example, in a weak fluorescent sample, the increase of power by increasing imaging contrast, but will also increase the risk of phototoxicity. One can also modulate the wavefront of the beam to remove aberrations which increases imaging resolution and depth, but measurement time taken for each wavefront increases the risk of photobleaching. Therefore, all the parameters are coupled with each other; there is no single ideal solution to solve them all, but can only be optimized with the mind of extracting information as much as possible

under the photon budget. Since the imaging depth of fluorescence microscope has been increased by the using of multiphoton technique as we discussed in Chapter 1, in this chapter, we will mainly discuss the methods of laser engineering in terms of speed resolution, spatial resolution and phototoxicity control.

2.2 Rapid Point Scanning Methods

The dwell time of the laser beam is perhaps one of the key limiting factors of the temporal resolution in the multiphoton microscope because of the restrictions of the absorption efficiency and fluorescence lifetime [114]. Scanning is a direct and straightforward method to control the dwelling time of the laser. The major scanning strategies in the multiphoton microscope are point scanning [60] and multi-focal scanning [115], as demonstrated in Figure 2-2. Video-rate scanning multiphoton microscope based on point scanning require fast scanning devices (e.g. mirrors, diffractive grating). For point scanning system, a triple mirror design (a pair of galvanometer mirrors (GM), one fast scanning mirror and one slow mirror [41]), called tandem scanning provides both fast imaging as well as targeted imaging sites [116].

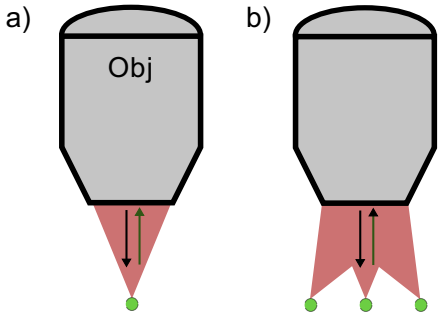

Figure 2-2 Schematic diagram of different scanning strategies. a) point scanning. b) multi-focal point scanning.

Next, I shall introduce the laser beam engineering techniques of speed enhancement in multiphoton microscope, such as scanning by non-mechanic scanning devices (e.g. AOD or electrically tunable lens) [117], non-scanning illumination by holography and diffractive optics [118, 119], targeted path scanning (Lissajous path) [120] and beam multiplexing technique [26,

115]. Moreover, the beam shaping techniques that extend the depth of field with elongated PSF for video-rate volumetric imaging rates will be discussed [111, 121, 122].

2.2.1 Random-access Point Scanning

Random access scanning means the imaging ROI can be accessed randomly in three dimensions. In random scanning, AOD is the most used scanning device due to its inertial free property with 20 to 30 kHz frequency of beam position shift [123], which can achieve a volume of 250 x 250 x 250 µm at 40 Hz speed [124]. This technique had been applied to capture the highly dynamic physiology events such as action potential transients [125]. The schematic diagram of AOD based random scanning is shown in Figure 2-3[126]. The AOD is driven by an acoustic signal which generates a periodic pattern inside the acousto-optic medium, thus the refractive index is being modulated to a periodic grating structure according to the given signal [124, 127]. Light has been diffracted, and the first-order beam has been used with a related and controllable diffraction angle with a range of 0.05 rad [100].

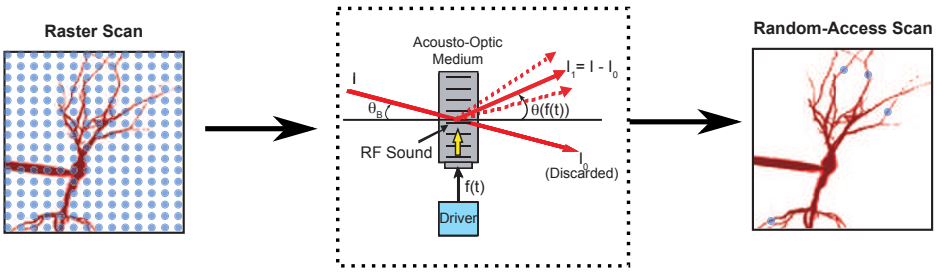

Figure 2-3 Principle of random scanning imaging. The left image is the image of a sample under raster scanning. The middle part is the schematic diagram of the AOD based scanning principle. The illustration of the sample with random access scan is shown on the right. The picture is adapted from [126] with permission.

2.2.2 Multiplexing / Multisite Point Scanning

The physiological event that the microscope need to capture might be fast and simultaneous, despite the development of scanning devices, there is still an intrinsic limit of the scanning speed, restricted to millisecond timescale response time, which is not that “simultaneous”.

Multiplexing the laser beam of illumination is another approach towards increasing temporal resolution in times of the number of multiplexing, so to make the laser scanning microscope more “simultaneous” within nanoseconds scale.

Temporal beam multiplexing can be done through the implementation of polarization beam splitter sequentially in the optical train, followed by different delay length to separate the light beam in a timescale of nanoseconds [26, 128-130]. And then these time difference signal together with the laser pulse clock are used as the demultiplexing signals to extract the signal from different paths in the photon detectors like PMT. The schematic process is drawn in Figure 2-4 a). From which, the light is delayed in integer times of 8 ns. These signals are then being used to do scanning in an either lateral or axial direction.

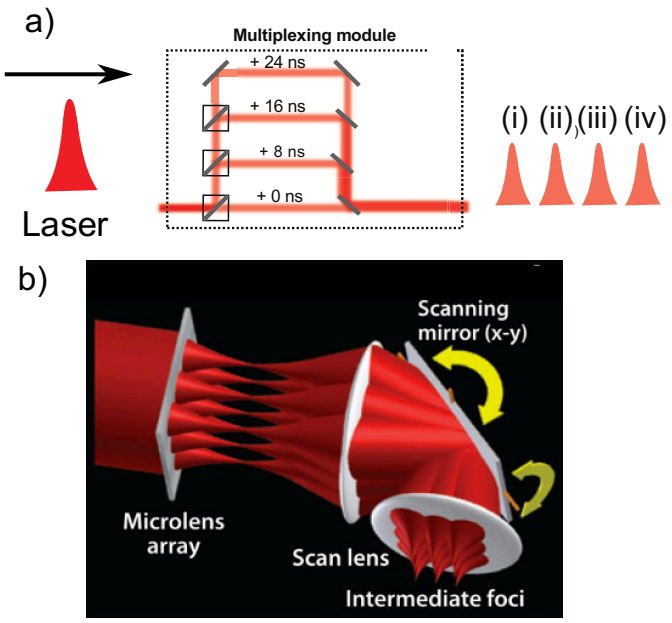

Figure 2-4 Principle of laser beam multiplexing. a) Temporal beam multiplexing by the beam splitter and delay path. b) Spatial multiplexing by the microlens array. This figure is adapted from [130] with permission and [131]with permission.

The time interval of the detected signal in temporal multiplexing will be overlapping correspondingly to the multiplexing of laser beams. This shows that the number of multiplexing cannot be arbitrarily increasing. The number of multiplexing multiply the period of pulsed laser should be longer than the decay time of the fluorophore so that the spatially distinct beam is

still distinguishable after detected. Obviously, in the multiplexing multiphoton microscope, short fluorescence lifetime dyes should be used. For example, 1 ns lifetime Fluo-4 dye had been used in a 4-beam multiplexing system with 80 MHz repetition rate (~ 10 ns) pulsed laser [26]. SLM had also been applied to achieve multiplex multiphoton microscope [132, 133], by modulating the phase profile of incoming laser beam to produce the desired beam splitting.

Another way of enhancing temporal resolution is to use spatial multiplexing, e.g. holography, microlens array to replace the laser scanning progress [119, 134]. The handling of the microlens array to achieve multisite focusing on focus plane has been shown in Figure 2-4 b). The multisite SLM imaging principle is based on the pioneering holographic work by Gabor [135], who used interference to reconstruct the shape of the object. In these imaging setups, the SLM is located at the back focal plane conjugated to the image plane through Fourier transform. Therefore, the relation of the desired pattern on the imaging plane and the phase profile at the SLM can be calculated through the phase retrieval algorithm [136]. The diffraction pattern is then used to do fast monitoring, stimulating and activation of neuron cells. In addition, by combining with the temporal focusing technique, 3-dimensional scan less holographic imaging and manipulation at the cellular level have been achieved, called sculpting light technology, which enabled the decoupling of light in the lateral and axial direction [137]. Despite the imaging speed enhancement, there is an unavoidable loss of laser power due to only the first order of light are being used in the diffraction effect. Compared to point detectors (PMT), the using wide-field CCD camera will degrade the contrast and resolution due to the cross talking of photons in the nearby area [138].

2.2.3 Axial Wavefront Shaping for Volumetric Imaging

Many critical biological processes happened in three-dimensional tissue scale at a millisecond time scale, such as blood cell flow in vessels and action potentials in the brain. There are several methods to extend the 2D scanning into 3D without losing temporal resolution [139]. Among them, the representative methods include temporal focusing [140-142], extended depth of field by elongated beam like Bessel beam [111, 121, 122, 143] and defocus imaging by deformable mirror [144] or electrical tunable lens [145].

The comparison of volumetric imaging methods is shown in Figure 2-5. Through the engineering of beam pattern at the pupil plane, volumetric imaging can be done by fast axial scanning (~kHz) with defocus aberration (parabolic shape) generated by deformable mirror [144], or extended depth of field by Bessel beam through ring shape illumination [146]. The unwanted signal from the defocus aberration is suppressed by the localized nonlinear absorption effect, so the PSF is still maintained with minimal aberration within a 100 μm axial scanning range. In the case of Bessel beam imaging, the depth of field can be extended flexibly from 15 ~ 400 μm without degrading the temporal resolution while achieving volumetric imaging by lateral scanning. However, it loses the axial sectioning which limited its application to only sparsely labelled samples. The methods mentioned above are still under the limitation factors, as shown in Figure 2-1.

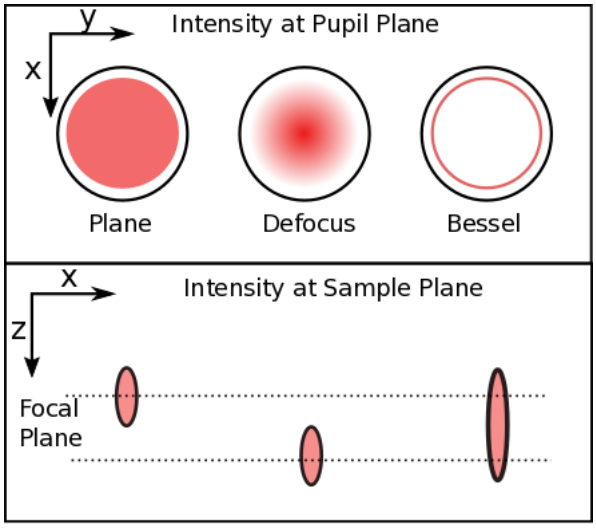

Figure 2-5 Volumetric Imaging Methods. In the top inset, from left to right, are using plane/Gaussian beam, defocused beam and annular ring at the BFP of the objective. In the bottom inset, from left to right are the PSF of each beam correspondingly.

In this following sections of this chapter, I will introduce highly flexible polygon laser scanning multiphoton microscope, which is suitable to a breadth of biological applications especially in highly scattering thick tissues with high photon efficiency and low optical dispersion [105].

2.3 Polygon Scanning Multiphoton Microscope

There are groups of commercial multiphoton microscopes with integrated graphical user interface (GUI) control and data-analysis software available for purchase. Those commercial systems provide an easy-access tool for biology researchers. However, the convenience of having a commercial GUI comes with a drawback, the cost of the product. Building a self-designed multiphoton microscope, not only can save the cost. However, most importantly can provide the flexibility and extendibility to a customized platform for various investigation targets which cannot be achieved simultaneously from the market by using off-the-shelf components. There are lots of examples of using self-made two-photon microscopes in the neuron science area. But access to building customize multiphoton microscope with extended flexibility is still limited to many laboratories in fields like cancer biology to reach out the versatile and unique questions. Both hardware and software efforts and technological innovations have been made, to build a highly flexible multiphoton microscope with both high spatial and temporal resolution integrated with a customized control system. Also, novel real-time AO techniques have been designed and utilized. High contrast volumetric imaging with photomanipulation function has been developed and applied to different biological scenarios to demonstrate its reliability and performance.

There are kinds of literature about how to construct customized multiphoton microscopes, from the choice of the lasers to the optical train of lenses and detectors [102, 116, 147]. As we mentioned before, the advantage of the self-made multiphoton microscope is high flexibility, and scanning device and scanning strategy are the crucial factors of flexibility. Typical scanning strategies are raster scanning, random access scanning, Bessel sheet scanning and SCAPE scanning. Among them, the traditional raster scanning can be improved by switching between the fast scanner and slow scanner (tandem scan) and has its advantage in its balancing of speed, optical sectioning and efficiency even though it has a disadvantage of inflexibility but can be improved with design strategies. The random access scanning will have the ability of selective ROIs but lack of energy transmission efficiency of fs laser pulses due to the dispersion and diffraction effect. Since multiphoton absorption is nonlinearly dependent on the

light intensity, this will cause a severe problem in terms of image performance. So in our design, to construct a widely useable multiphoton microscope, sticking to the rule of thumb “less is more” in multiphoton microscope design, we choose raster scanning as our scanning strategy.

Another important aspect is to identify matching scanning devices. The four significant types of scanning devices are galvanometer mirror (GM), polygon mirror, resonant galvanometer mirror and acousto-optic deflector (AOD). We have discussed their features in Table 1-2. Reflective mirror scanners (GM, polygon and resonant GM) have overwhelmed performance in efficiency and quality comparing to diffractive scanners (AOD). In terms of scanning speed, polygon and AOD stand out due to their high speed and scanning range. Nevertheless, comparing AOD and polygon, the polygon has a scan angle, two orders larger than AODs. Polygon mirror can operate over a broad dynamic range of scanning speeds from 2 kHz to 100 kHz [148] and retain optical quality and efficiency over AODs. Among reflective devices, the polygon has advantages in its flexibility of speed control and large scanning angle and linearity comparing to resonant GM, which has a fixed scanning speed and nonlinear (sinusoidal) scanning range. Therefore, polygon mirror as the scanning device has the potential for delivering high-resolution laser beams with flexibility in rate.

There are quite a few polygon based laser scanning microscopes had been developed, but with a single control and limited programmable software. The imaging of biological dynamic biological process would require active control of the polygon. For example, imaging speed can be varied from 5 FPS for tracking of T-cell to the 100 FPS for capturing neuron calcium transients and up to the 1000 FPS for red blood cell measurements. However, all the previous polygon microscopes only supported imaging with 100 FPS or so for specific applications, as shown in Figure 2-6. All in all, currently, there has not been a flexible, programmable and controllable framework both in hardware and software for polygon scanner microscope, which can fully utilize the dynamic scanning properties.

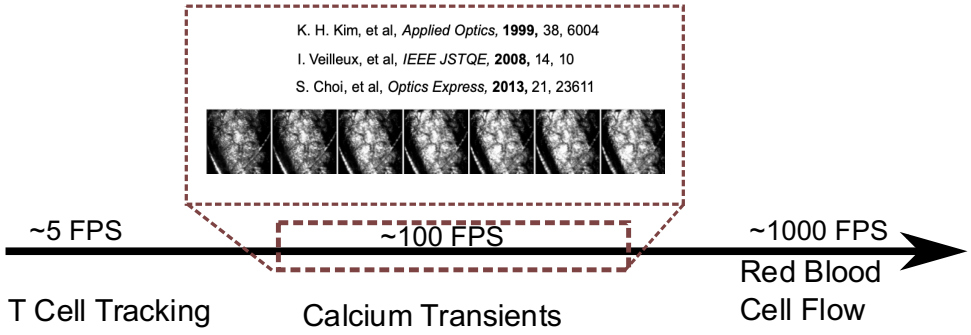

Figure 2-6 Schematic image of polygon laser scanning microscopes' and biological events' speed, in which, the horizontal axis indicates the speed required for observing different types of events. The data of the polygon microscope is from the literature [148-150]. Inset figure is adapted from [148] with permission.

Here the detail of how to build a polygon based multiphoton microscope with multi-channel detection and flexible imaging control will be present. It will apply to both brain slices imaging and blood flow rate measurement, as an example of its feasibility. First, the detail explanation of building the 4f system using the achromatic lens for conjugating the polygon pupil plane will be given, followed with constraints optimization in the design of the multiphoton microscope. Then, the control schematic and the results of the measurements will be introduced. All animal experiments in this chapter were performed using procedures approved by the Australian National University Standing Committee for Ethical Research Using Animals (protocol 2015/46).

Polygon mirror is a mirror with multiple facets installed on a spinning cylinder driven by a magnetic motor. Polygon scanning setup was firstly used in a video-rate confocal ophthalmoscope [151]. The basic structure is using the polygon mirror as the faster scanning axis and synchronizing its reflection signal as an HSYNC trigger. The light incident on the polygon mirror will be reflected periodically, as described in Figure 2-7. Here the input beam has an oblique angle of $\theta + \alpha$, where α is the half-angle of the polygon mirror to the number of facets. The total reflection angle is time-varying which relates to the speed of rotation ω; the equation is

$$reflection\ angle = 2(\theta + \alpha - \omega t), t \sim [0, {}^{2\pi}/_{n\omega}) \qquad \text{Equation 2-1}$$

where n is the number of facets. The period for each facet is T=$^{2\pi}/_{n\omega}$.

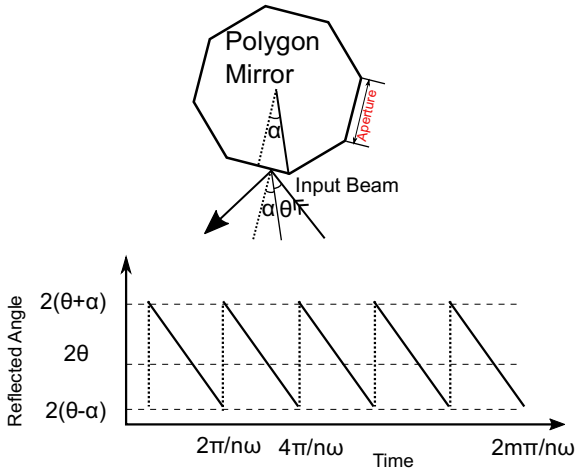

Figure 2-7 Geometry of polygon mirror as a scanner with a deflection angle varying over time. The reflection angle is periodic variable refers to the speed of rotation and number of facets.

In order to deliver this line scanned laser beam into the objective without truncating by the boundary of the pupil (vignetting), the 4f system needs to be used. The essential logic is using objective to translate the scanned angle of collimated input beam into the position of diffraction limited point at the focal plane. The schematic is shown in Figure 2-8.

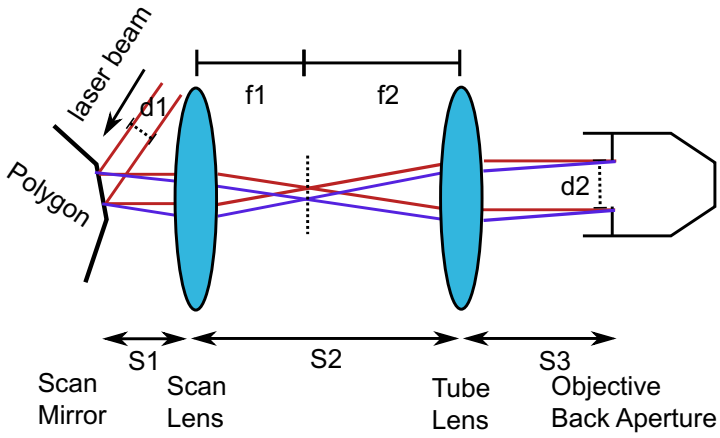

Figure 2-8: Side view of a schematic of the 4f system for delivering the laser beam to the objective without truncation. From left to right, the reflected after the polygon light goes through the scan lens

and tube lens sequentially. The value of distance *S1*, *S2* and *S3* should make the aperture of polygon be imaged at the back aperture of the objective.

4f system with a collimated input beam gives the advantage of telecentricity, which is essential for the infinity-corrected objective. The 4f system is based on the theory that the image plane and focal plane of an ideal lens is determined by Fourier transform, so with 2 lenses allocating in a 4f configuration, the second lens will function as a reverse Fourier transform to the image of the first lens. Hence the final image of the second lens is a conjugate image of the input image of the first lens. 4f system has been broadly used in the laser scanning system. In our design, the imaging of polygon aperture plane will be relayed to the objective's back focal plane by a sequence of 4f operations.

After we got the 4f system principle, aligning a 4f system requires the considering of effect of the unsymmetrical lens shape. Since the lens used in optical microscope setup is the achromatic lens with different front and rear curvatures, the front and back focal length will be different as well. The solution to this is using the datasheet of the lens provided by the manufacturer. For example, the achromatic doublet lens has the schematic as shown in Figure 2-9,

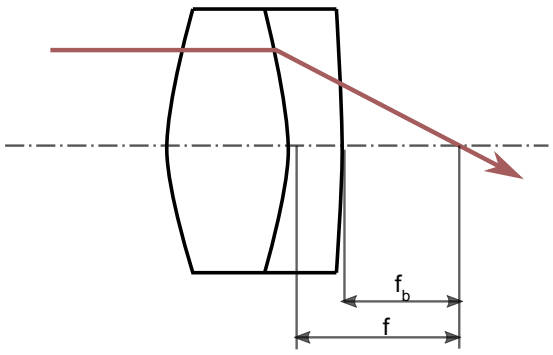

Figure 2-9 Geometry of achromatic lens. The right-angled line indicates the light beam direction.

in which f_b is the back focal length. Usually, f_b can be acquired from the datasheet with unprovided front focal length. One solution is using ray-tracing simulation software to simulate the value. Otherwise, "pair to pair" alignment will be helpful through removing one of the

lenses in the 4f system and observing the divergence of the beam to get the location of the front focal plane.

Here we have discussed how to construct a laser scanning setup reliably. However, one thing left is choosing the right focal length for the optical train. Based on simple lens formula, we know that the diameter of the laser beam can be collimated up or down with the ratio of $f2/f1$. The question is in a polygon laser scanning microscope, which is the right value of the lens. Besides, constrains of FOV need to be concerned. In terms of FOV, there is one optical invariant at the back aperture and the polygon aperture [152], which is

$$I = r \cdot sin(\varphi) = NA_{effect} \cdot r_{FOV}, \qquad \text{Equation 2-2}$$

where NA_{effect} denotes the effective numerical aperture of the objective, r_{FOV} denotes the radius of the FOV, and r and φ denote the radius of the and incident angle of the collimated beam at the aperture plane. The equation of NA_{effect} is,

$$NA_{effect} = NA \cdot \frac{d_{laser}}{d_{BFP}}, \qquad \text{Equation 2-3}$$

in which, d_{laser} is the diameter of the laser beam, usually is the full half-width maximum (FHWM) of the Gaussian beam, d_{BFP} is the diameter of the back focal plane.

This constraint gives the maximum FOV of a system can achieve, in other words, since usually, we want the FOV as big as possible, then this equation can guide our choice of the focal length of a lens. Another constraint on the polygon mirror is the duty cycle of scanning, which is the ratio of active scanning time and the total laser beam dwelling time. The maximum scan angle, therefore, will be

$$\phi_m = \frac{2\pi}{n}\left(1 - \frac{d_p}{W_p}\right) = \frac{2\pi}{n}\left(1 - \frac{3r_p}{W_p cos(\alpha+\theta)}\right), \qquad \text{Equation 2-4}$$

where ϕ_m denotes the maximum scanned angle, n is the number of facets, d_p denotes the diameter of the beam, W_p denotes the width of the aperture of polygon, r_p denotes the input beam radium, and $\alpha + \theta$ is the incident angle of the beam to the polygon, the same as the

geometry in Figure 2-7. So the maximum of optical invariant will be $I = \phi_m \times r_p$, which is a quadratic equation of the value r_p, so there is a maximum point of the *I* when the derivative of *I* to r_p is 0. That value is

$$r_p = \frac{2\pi}{n} \cdot \frac{W_p cos(\alpha+\theta)}{3} . \qquad \text{Equation 2-5}$$

In our case, the polygon mirror we use is a 36 facets polygon mirror (Lincoln Laser, US, DT - 36 - 250 - 025) with an aperture size of 4.8 mm × 5.0 mm. The input angle here we choose is about 30° considering the mechanic dimensions, then substituted these values into Equation 4-6 we get the optimal radius is about 1.42 mm, so the diameter is 2.84 mm under the optimization constraints in our case.

The total optical setup is shown in below Figure 2-10, the lens focus and spacing distance for alignment are listed in Table 2-1. The beam diameter out from the Tsunami femtosecond laser (Spectra Physics, US) is less than 2 mm; it was then collimated up to 10 mm after the expansion of L1 and L2. After L3 and L4, it was collimated down to 2.33 mm before the polygon aperture, then expanded to 4.66 mm after L5 and L6 for fully passing through the aperture of GM (Cambridge Technology: 6220H, 7 mm × 5 mm). Then it delivered to the scan lens (L9) by another 4f system of L7 and L8. The focal length of the tube lens used for this work is 150 mm, so the final diameter of the laser beam was 15.53 mm. The objective here I employ has a 16.5 mm BFP (Zeiss: 20x 1.0 NA Apochromatic). All the lens are Thorlabs achromatic doublets. I used a power meter to measure the output laser power, and the output power is set to be 100 mW after the laser. The laser power dropped to 82 mW and 75 mW before and after the polygon mirror. Then it decreased to 65 mW after the GM, and the final output power after the objective is 41 mW, so the transmission efficiency of our system is about 41%.

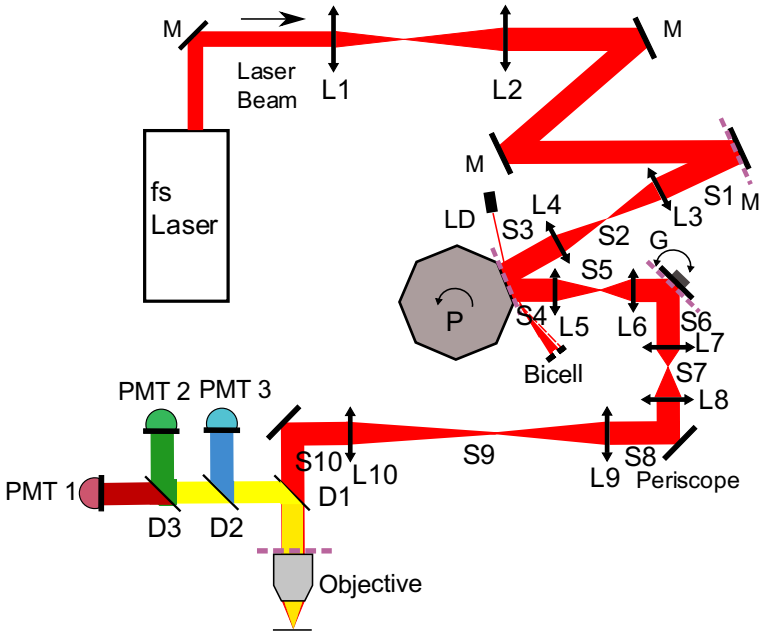

Figure 2-10 The optical schematic of polygon multiphoton microscope. L denotes the lens, M denotes mirrors, P denotes polygon mirror, d denotes spacing distance, LD denotes laser diode, G denotes GM, and D denotes dichroic mirrors. There are three PMTs being used in this design, including blue, green and red channels

Table 2-1 Parameters of lens and distances in the setup.

L1	50 mm	S1	156.9 mm
L2	300 mm	S2	173 mm
L3	150 mm	S3	75.3 mm
L4	35 mm	S4	72 mm
L5	30 mm	S5	78.8 mm
L6	60 mm	S6	67.7 mm
L7	60 mm	S7	152.9 mm
L8	100 mm	S8	210.4 mm
L9	125 mm	S9	212 mm
L10	150 mm	S10	208 mm

The back emanated photons were detected by the same objective through epi-fluorescence detection. D1 is a multiphoton single-edge dichroic beam splitter (Semrock, FF665-Di02), D2 denotes a 488 nm long-pass edge filter (Semrock, FF488 – Di02) and D3 denotes a standard dichroic beam splitter (Semrock, FF562-Di03) are with steep edges at the high reflection and transmission bands. The red channel detector is a highly sensitive GaAsP PMT (Hamamatsu, H7422-40) with 40% quantum efficiency, blue and green channels are multialkali PMTs (Hamamatsu, R3896) with about 20% quantum efficiency. Depending on the ratio of the PMT FOV to the size of BFP, high NA collection lens might be allocated in front of the PMTs.

2.4 Control System of Polygon Scanning Microscope

After building up the optical train of the polygon microscope, the other aspect is developing the control system. The control system is composed of a high-speed frame grabber with PCIe slot from Matrox (Helios eA/XA), a generic programmable DAQ board from National Instruments (PCI6110) providing the digital synchronization signal and analogue wave signal, as well as a customized PCB board for generating horizontal synchronization signal (HSYNC) from the polygon. The frame grabber here uses FPGA based analogue television technique, which means the mapping of pixels is based on the horizontal synchronization signal (HSYNC) and vertical synchronization signal (VSYNC). With these synchronization signals, time jittering artefacts and accompanied image aliasing are suppressed and optimized by the professional frame grabbing card, the synchronization between frame grabber's pixel clock and laser's repetition rate is not necessary. There are other options of frame grabbing, e.g. using a high-speed analogue to digital converter (ADC) (AlazarTech, ATS9440), which can provide up to 125 MS/s sampling rate, while the Helios eA/XA can only offer a 65 MHz pixel clock. However, compared to the ADC, the advantage of a professional frame grabber is in its libraries (MIL) and its easy configuration in imaging task (DCF), as well as its further extendibility to advanced graphics processing, like machine vision and computer vision. Therefore, choosing a frame grabber card provides performance and flexibility, which is well associated with the motivation of building a customized multiphoton microscope.

PCI 6110 is a PCI slot-based multifunctional I/O card, which can to simultaneously sample four channels at 5 MS/s with 12-bit resolution. It has two analogue output channels (AOC), which will be used to drive the two GMs in our design. It also retains two 24-bit counter outputs (Ctr 0 and Ctr1), one will be used to provide the VSYNC signal synchronized with the AOC as the start of the frame, the other one will be used as the driven signal for the polygon driver (BMC-7). There are other options for this as well, for example, using Arduino Due to as the controller [153] or using a microcontroller [150] to do the control. However, again, the use of a generic PCI board provides the best flexibility with graphic programming language LabVIEW, and interfaces with all the other hardware which will be used to enhance its functionality. Hence the choice of the PCI 6110 board matches with our motivation to build a flexible and easily extendable multiphoton microscope.

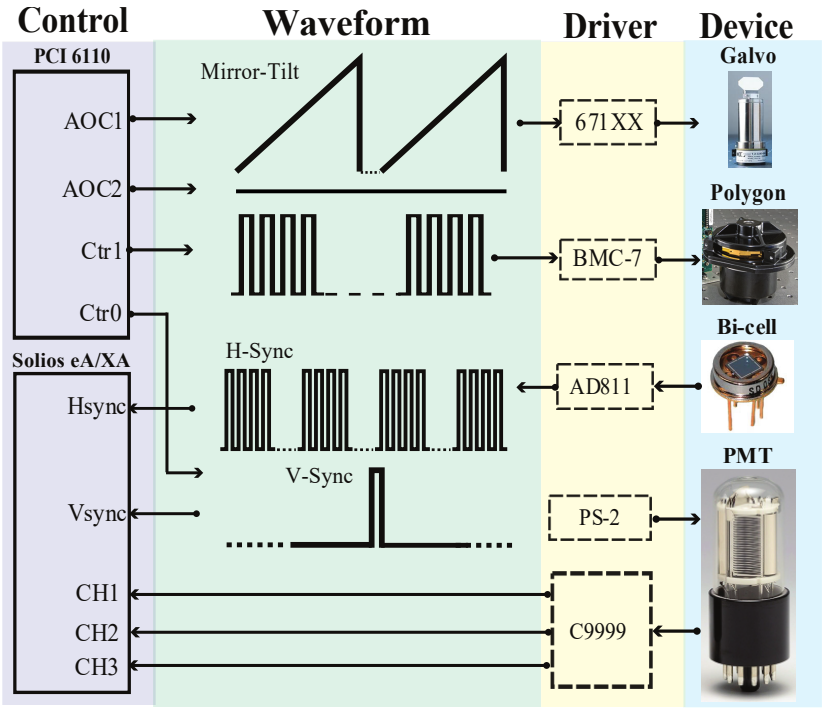

Figure 2-11 Schematic of the control system. From left to right are the control electronics, control signal, drivers and devices.

The whole control schematic is shown below in Figure 2-11, in which both the PCI 6110 and Solios eA/XA are installed on a work station (Dell: T3600). PCI 6110 uses a sawtooth signal to drive the GM through a driver 671XX from Cambridge Tech. The Ctr1 drove the

polygon mirror with TTL signal, and Ctr0 is used to send VSYNC signal to the frame grabber. The collected photons are converted to electricity by PMTs and are then amplified and converted to voltage signals. The first three channels are used to grab the red, green and blue signals separately, which can be combined as an RGB image.

Here one of the differences in our control system is that we used a TTL signal to control the rotation speed of the polygon. Therefore we can achieve different scanning rates while at its fast axis, which has not been made before in a polygon microscope. This degree of flexibility is one of the most useful features that the polygon mirror has compared to other scanner options such as the resonant galvanometer scanner. There are two factors associated with the scanning speed, which sometimes would be neglected in the laser scanning microscope design. First, the scanning speed is related to the laser dwelling time, which is associated with the photodamage like photobleaching and phototoxicity as we mentioned before. The photon detection efficiency of each pixel is shown in the below equation,

$$I_{pixel} = \delta \cdot \rho \cdot E_{pulse} \cdot n_p, \qquad \text{Equation 2-6}$$

in which, I_{pixel} denotes the intensity of the pixel, δ denotes the detection efficiency, ρ denotes the multiphoton absorption efficiency, E_{pulse} is the energy of single laser pulse, n_p means the number of pulses during the pixel dwelling time. In order to improve the signal intensity, considering the detection and absorption efficiency are mostly determined by the detectors and chemical probes, the easy tuning option is to strengthen the pulse energy or say laser power. However, the photodamage is a high order relation with laser power; the effects of the resulting photodamage would outweigh any improvement in the signal that could be expected. Therefore the laser power is preferred to be as low as possible. The only option left is to increase pixel dwelling time t_{pixel} as an alternative option to increase the signal, which can be controlled by the polygon scanning rate and will be useful when the signal is weak, and probes are photon sensitive.

Second, the scanning speed affects the spatial-bandwidth product (SBP), which is the number of pixels in one frame, and this value will affect the spatial resolution that the system

can achieve. The information delivered by the whole opto-electro system without aliasing requires that the sampling pixel length is smaller or equal to half of the PSF, the equation is

$$SBP = (\frac{\sqrt{2}r_{FOV}}{0.5 \cdot r_{PSF}})^2 = 8(\frac{r_{FOV}}{r_{PSF}})^2, \quad \text{Equation 2-7}$$

where r_{FOV} denotes the radius of FOV, r_{PSF} denotes the FWHM of the PSF. From this equation, for an 800 nm wavelength two-photon microscope with 512 x 512 μm, the SBP is about 2 megapixels. And since the SBP also equals

$$SBP = \left(\frac{T_H}{f_P}\right) \cdot N_H, \quad \text{Equation 2-8}$$

in which T_H denotes the time for one horizontal (fast) line scanning which is determined by the polygon rotation rate, f_p denotes the frequency of pixel clock, and N_H denotes the number of horizontal lines per frame. The scanning speed and pixel clock constrain the SBP, and these two factors are both able to be easily tuned in our design. So our system can to control SBP using one scanning facility instead of using backup scanning devices like in other resonant GM systems. Moreover, this flexible control of SBP breaks the limitation of camera-based imaging with a fixed number of photodetectors.

The speed of polygon is based on the frequency of the TTL signal to the driver board, the equation is

$$f_H = L_H * fps * 2/n, \quad \text{Equation 2-9}$$

where n is the number of facets, L_H is the number of desired horizontal lines, f_H is the driving frequency. The coefficient 2 comes from the number of effective poles in the BMC-7 driver board datasheet. Then the schematic of the dynamic of control of polygon and corresponding SBP image is shown in Figure 2-12.

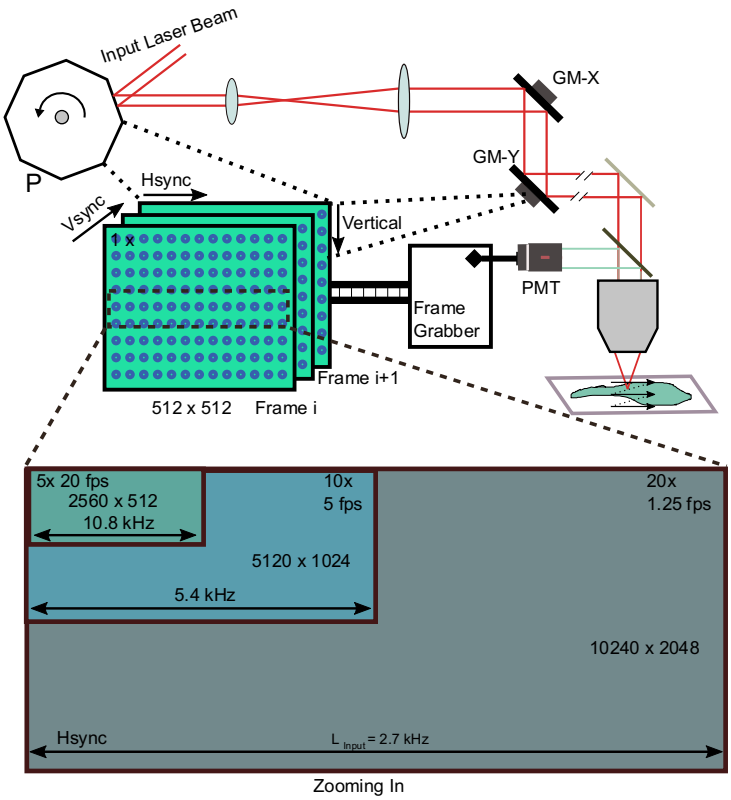

Figure 2-12 The schematic of polygon scanning and frame grabbing. Frame grabber generates the frame based on the sync signal from the polygon and the vertical galvanometer scanner (GM-Y). The image frame is flexible with SBP by changing polygon and pixel clock, achieved the optical zooming, which was considered not possible by polygon scanner before.

2.5 Multiphoton Microscope Control Software

In addition to making the microscope as flexible as possible at the hardware level, at the system level, a demand for a flexible, customized control software is also intensive. The software in a customized microscope is sometimes being neglected by both the microscopists who build the microscope and the biologists who use the microscope [154, 155]. The current trend in microscope development is to integrate more and more devices to enable the microscope to be a platform with more functions than just imaging, such as a multi-modality bio-photonics system and being able to switch between different imaging targets. For example, the most recent state of the art microscope, multimodal optical scope with adaptive imaging correction

(MOSAIC), used both a deformable mirror and spatial light modulator (SLM) as wavefront modulators and wavefront correction devices, and a group of semiconductor lasers and a femtosecond laser for illumination and guide star laser, for multiple imaging modalities of widefield, light sheet and multiphoton excitation [156, 157].

Another example is a multi-mode multiphoton microscope with both two-photon and three-photon imaging at the same time and high-speed temporal multiplexed imaging capability of axial or lateral stitching, for extensive volumetric imaging of brains *in vivo* [130]. There are also other types of high accuracy beam shaping microscopes, like time-reversed ultrasonically encoded (TRUE) light focusing, which uses high pixel count SLMs to modulate the beam to conjugate to a more in-depth focus point [158]. All these states of art microscopes showed that microscopes are fashioned to be more and more powerful with unprecedented performance at the cost of applying dedicate and sophisticated devices. So it is not hard to imagine, that using those type of microscopes for general users to achieve specific biology experiment is not easy and straight forward process. Therefore, in order to make the microscope accessible and release its real power in biological applications, friendly control software combined with customized function modules is essential [159]. However, in most of the current microscope designs, the controlling part has just been neglected, the control software and the graphical user interface (GUI), has not been included even in the supplementary. With the current trend of increasing complexity in microscopes, the software that provides the interface between users and microscope will become more and more critical. Therefore, it is crucial, and it is the right time for current microscope researchers to start thinking about customized software design while building novel microscopes.

Here we mentioned the importance of software design in microscopes. The most important thing is that control software will be a milestone for the whole system. In other words, this software will facilitate the further development of microscope hardware. The software will be able to be extended and quickly iterate, to the adding of new devices for new functions or new imaging experiment protocols. The software should have a framework that is extendable and adaptable, in consideration of the microscope would be more complicated after years of

developing. In summary, the rule of thumb is choosing a suitable program language with expandability and easy maintenance to the developers.

Another critical factor in developing this software is the matching and orientation towards the microscope hardware. Because it is still a hardware control software rather than pure software, the software will have complex interfaces to different devices. Therefore, a system that works with most standard devices is demanded.

Lastly, an open-source software requires the distribution to the broader microscope community as much as possible. However, there are still issues with the open-source software for hardware control, because the hardware of microscope is still not unified to an industry-standard as what happened in the computer industry, so how useful and how accessible the open-source microscope control software could be is still unknown. So, in this case, there are more efforts need to be made both in the open-source software and hardware, since useful open source software can only be based on the standard and established devices.

Due to the time limit in the live animal imaging, the customized control software should be designed for the smooth manipulation of the polygon system but retains its unique feature. At the time when we were building our polygon microscope, there was no such open-source control software that supports the polygon scanner for microscope control in a flexible way. So here, the polygon microscope is developed to reach the target of a fully flexible custom microscope system with ability and capability of conducting different biology experiments and available to most general users.

Here in this section, I will first introduce some of the existing open-source control software, and then explain the framework and constitution of our self-designed polygon microscope control software, PScan. Then a discussion of how to extend the PScan software with more function modules will be made. This subchapter about software will complete our hardware discussion in the previous content so to finish the design of the customized polygon microscope as a real interaction system.

2.5.1 Existing Standalone Software

There is quite a few open-source microscope control software available for the community, developed for different purposes by people from different backgrounds [160]. Among those open source software, the representative microscope control programs are HelioScan, Scan Image and Micro-Manager [161-164]. All of them have some unique features which will be introduced from aspects of programming language, application expendabilities, accessibility and reliability.

HelioScan is a LabVIEW (National Instruments, US) based control software, designed mainly for multiphoton microscope control, with object-oriented programming, and a library of hardware support for different applications depending on the imaging targets. One of its most prominent features is that even though it is based on LabVIEW, it does not have a fixed GUI. However, a flexible GUI generated automatically by the user's choice of imaging functions and modules, which provides enormous flexibility for reaching the different requirements of different biological areas for the customized microscope control.

The core idea of HelioScan is to maintain the usability of microscope software to different users and successor developers. One major problem is the limited access to the self-developed control software from the general users, the different using manner and habit which might induce run errors, and the potentially incompatible versions developed by various follow-ups. To solve the above problems, HelioScan adopted the self-defined run-time framework, with a main virtual instrument (VI) as the user interface, and customized components which can be selected from a library of LabVIEW classes to consist the content of GUI. Each class has the same interface and constituted by the same function devices. To further formalize the class, top-level components (TLCs) and subcomponents are distinguished. The structure of HelioScan is shown in Figure 2-13, in which, a) is the schematic of a constructed HelioScan user interface, with the selected components for instancing and dispatching the user interface. b) is the generated GUI from HelioScan.

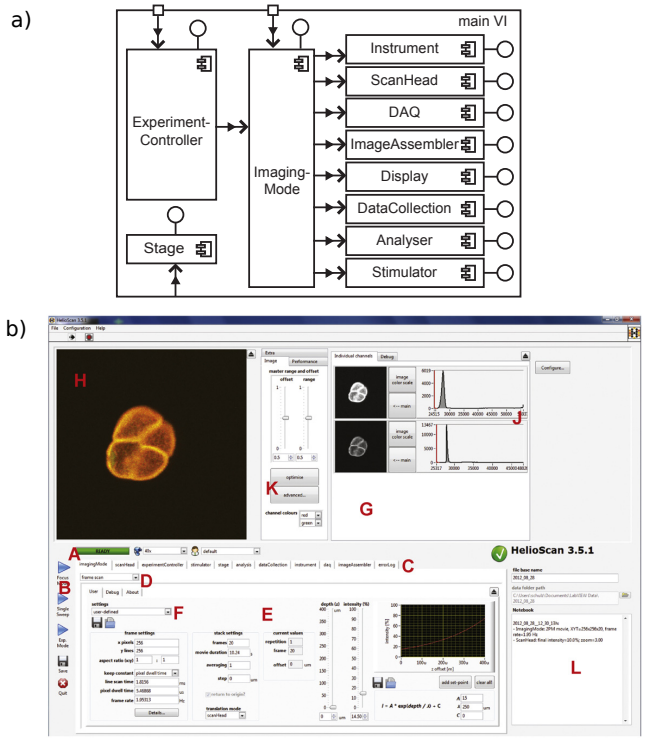

Figure 2-13 Schematic of HelioScan. a) The structure of HelioScan dispatching. b) The generated GUI of HelioScan. The red capital character labelled different functional modules of the HelioScan GUI. This image is adapted from [161] with permission.

Figure 2-13 shows a completed GUI with functions of both imaging display and quantitative analysis tool. To use this powerful control software, a fully installed LabVIEW is required, with quite a few extra libraries, even including XML support module. The use of HelioScan requires the user to be familiar with the hardware components for the selection of the right parts from a big list. In general, HelioScan provides a potent control software option with broad applications from intrinsic optical imaging, to two-photon imaging with different scanning devices and scanning strategies. It can do raster scanning, circular scanning, and volumetric scanning. It supports most of the LabVIEW based devices, including high-speed FPGA device as well.

Another popular control software is ScanImage, which is based on the MATLAB program, designed for multiphoton imaging microscope system as well. It also supports multi-channel imaging and volumetric image acquisition, with supports of different scanning devices and

high-speed analogue to digital conversion (ADC) devices. ScanImage also has a flexible user interface by configuring the initial user file when launching it for the first time. The structure and sample user interface are shown in Figure 2-14. ScanImage will ask to read the previous configuration file saved or configure a new file before initialising the GUIs. Then it will read the user file to set up the configuration of the system. With the reading of the configuration file, ScanImage will be readily able to respond to users' control so that image acquisition will begin. In this process, ScanImage shows its relative simplicity compared to other control software. Moreover, most of the microscope users in academic are familiar with the MATLAB software, and MATLAB software is relatively simple to install without requiring of additional packages for running ScanImage, which is one of the most significant advantages of ScanImage, for its simplicity. In addition, ScanImage provides clear help documentation on a specific website, maintained by Vidrio Technologies (US), which thus is more user-friendly towards to beginners in multiphoton microscope area, or people without the background of professional software developing experience.

The GUI of ScanImage is shown in Figure 2-14, in which multiple small control and parameter setting windows are opened during usage. In this case, the ScanImage will be more like a separated window-based GUI rather than a single integrated GUI, which might affect the using efficiency in an elaborate biological experiment. So in general, ScanImage provides easy access to the control of sophisticated multiphoton microscope without the specific requirement of programming, which makes it very popular in the custom multiphoton microscope developing area, and more and more users are using it to control their microscope, almost 600 applications utilized ScanImage by 2014. It is indeed a successful control software so far.

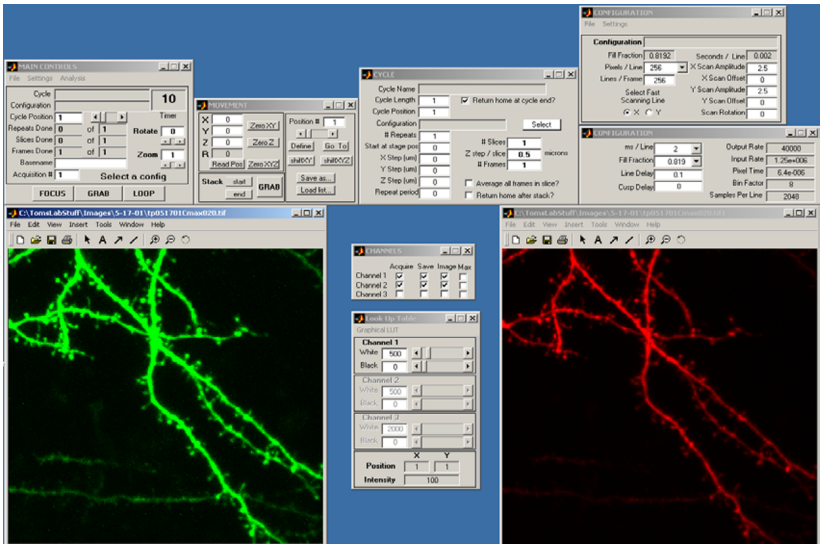

Figure 2-14 A snapshot of ScanImage's control panels. It is adapted from [162] with permission.

The last example of open-source microscope control software is Java-based micro-manager (μManager). μManager is an executable software with highly integrated and tidy installing packages which provides instrumental version to all the operation systems, from MacOS to Windows and Ubuntu/Debian Linux. μManager has a public graphic user interface (GUI) similar to the previous mentioned ScanImage and HelioScan, with a fixed everyday layout to general users but advanced customization tools as well. And also, since μManager is designed as a plugin for the ImageJ software, it inherited and maintained the simple style of ImageJ. Therefore, comparing to other open-source microscope control software, μManager has a higher degree of the package and a concise panel, makes it very easy to install like other commercial software, which stands it out at the easy to use aspect.

μManager provides universal supports to a comprehensive list of devices, including cameras, stages, microscopes and other peripheral equipment. μManager concludes several different modules, including a collection of device adapters libraries for hardware component controlling, a framework for the hardware control system, a window-based GUI to configure and coordinate these components, a script panel for writing customized control protocol commands, and a plugin mechanism for additional using in extended applications. The extendibility of μManager is achieved through the idea of accessing application programming

interfaces (API). The developers can, therefore, add their own devices through API to reach the control of all hardware. At the user interface layer, the Java-based GUI will be used to manipulate the microscope. And this GUI is accessible with the μManager Script panel, MATLAB and Python programming language as well. Therefore, it has a similar function of flexibility in GUI customization. μManager is a simple and easy to use control software, which works well with camera-based microscope system. However, for most of the multiphoton microscope, which uses PMTs, μManager currently does not support well.

2.5.2 Polygon Microscope Control Software: PScan

Here we showed the current popular open-source software for microscope control, each of them has their features and advantages, but for the polygon microscope system, all the software mentioned above do not provide support to the polygon scanner. Therefore, a control software that can match the benefits of the hardware design is desired, the flexibility that polygon mirror retained. The biggest motivation in developing a customized control software is to match the unique requirements which cannot be made by the available tools, rather than recreating the wheels.

Second, all the above software, are more or less constrained to one specific programming language, and lacking interoperation among different user interfaces. For example, LabVIEW programming is good at hardware control and suitable for synchronization and triggering; however, weak at data analysis and intricate iteration design. While MATLAB is professional with extensive size data calculation and manipulation, but less support to do hardware control and high precision parallel synchronization control. While Java is a compelling and useful language, but with a complexity of writing and developing personal scripts for general users without a professional computer background. So here in our customized control software design, we want to make full usage of different programming languages without relying on one specific style, so to find a way of balancing and compromising the performance and easy access. Which means, this software not only should have multiple interfaces to different languages, to have the state of the art support to the hardware control but also maintains a

simple, integrated and straight forward GUI for general users, as well as upgradable extendibility for versatile functionalities and future follow-up developers.

We named the proposed control software as PScan software, for its purpose of polygon scanning control. The hardest thing in developing customized software for such a complex microscope system to meet the flexibility control requirement is always about the framework. Once the framework is settled, all the others of functions are just add-ons. So here, the building and structure of PScan framework will be demonstrated to verify the feasibility of our proposal about such software. Its function modules, within which the alignment module will be explained in detail for its importance for *in vivo* imaging applications.

2.5.3 PScan Framework

The first obstacle that the PScan software needs to solve is how to coordinate the groups of a wide range of different types of hardware devices and software packages and libraries. It is a process that decreases the entropy of the whole system into an organized hierarchized, ordered entity that provides the window both for general users and professional developers. Here the relations among users to microscope are drawn in Figure 2-15 a), by spherical diagram with the connection of software package and hardware device. In this figure, the complexity for users to get control of the microscope is displayed. In order to gain power of the microscope, the users need to pass through layers of software language and function packages from the computer level, to the hardware control software level, then through the hardware components driver in the microscope, before finally touching the microscope. In our setup, the things are more complicated, because we need to use high-speed professional FPGA frame grabber to achieve flexible control of the imaging, and programmable generic hardware control software LabVIEW, as well as multiple function modules from other software packages, such as ImageJ, both for saving time and maintain performance reliability. And we can see that the diversity of connection types among those modules in the figure, from C/C++ language to MEX file and DAQ communication, as well as DLL and ActiveX interfaces. Therefore, a frame structure that could communicate the hardware and offer the general users easy access is desired.

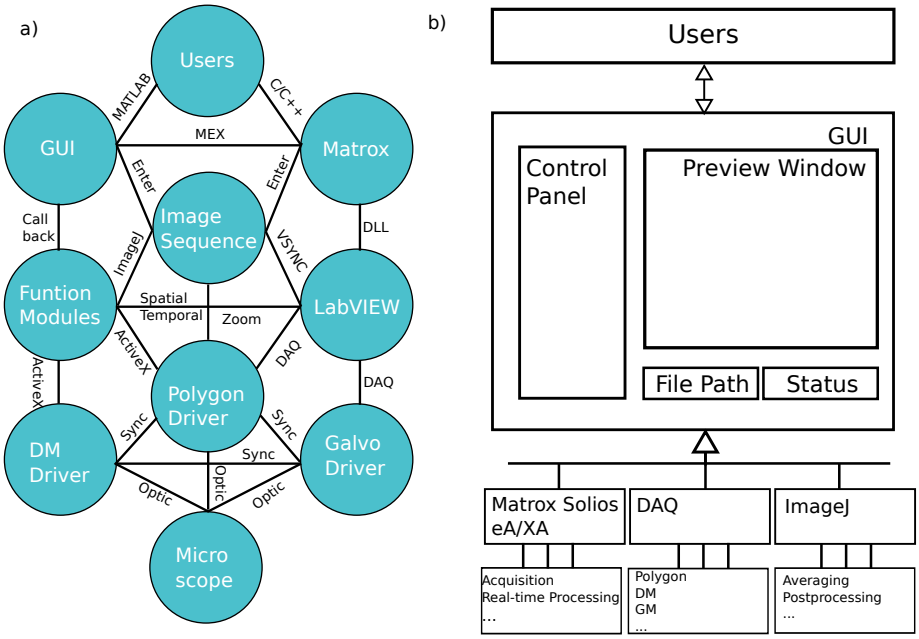

Figure 2-15 Schematic of the polygon microscope system. a) The schematic of relations among users and microscope control. b) The proposed design schematic of PScan software. It is a simplification process of rescheduling the relationships in a) into an ordered hierarchy structure.

In PScan, in order to retain the simplicity and precision, a combinational software structure design is chosen, to take advantage of both LabVIEW and MATLAB. In this case, we used MATLAB as the primary top-level GUI language, for its easy accessibility and high performance in extensive size data processing, uniquely the matrix, which is the image volume. More, for the low-level hardware control, we chose LabVIEW to do this work. Since LabVIEW provides excellent support to broad types of devices communication, and easily programmable instrument control by through graphical programming. For image postprocessing, ImageJ provides a substantial standard package of image analysis tools; therefore, so we chose ImageJ as our support postprocessing software. The working operating system is based on Windows, considering its market occupancy, especially the support to most of the available hardware. Then the schematic of our PScan framework looks like Figure 2-15 b). In which, the users directly interact the GUI with straightforward functions to manipulate the microscope in real-time without any delay, and the GUI has multiple interfaces to different hardware under it to communicate the microscope, but still with accessibility either by buttons or script panel on the GUI. In this way, the complex polygon microscope system turns into easy access and secure

manipulation system, for high throughput, high efficiency and high-quality biological information acquisition microscope platform, for broad users without prerequisite requirement of background knowledge of polygon hardware or software experience.

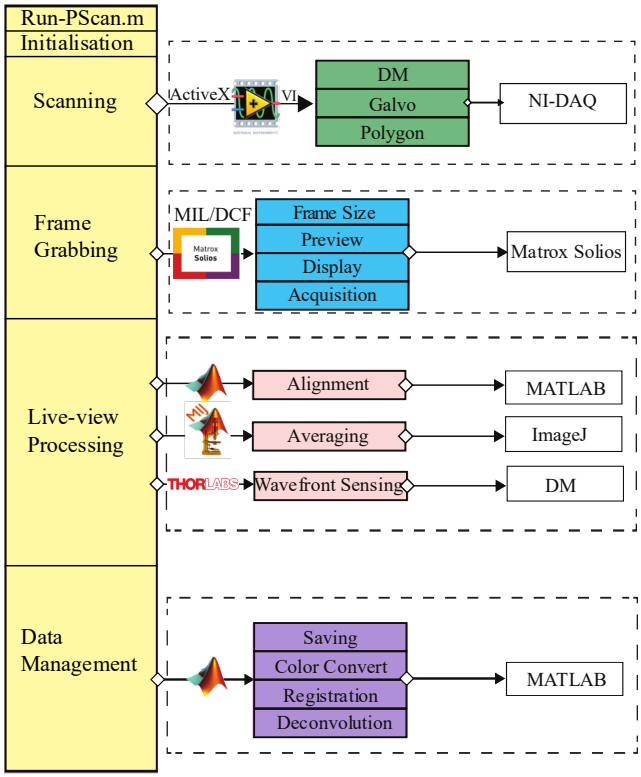

Figure 2-16 The main framework of PScan and its interfaces to different modules for microscope imaging control.

This detail of the structure and communication interface of PScan is shown in Figure 2-16, in which, the complex structure in Figure 2-15 a) has been ordered into a linear arrangement with direct relation to each target functions or devices. In other words, the entangled device functions and imaging performance are decoupled. For example, the synchronization among the three crucial scanning hardware devices, polygon, galvo and DM are complex in hardware level, which is almost impossible for the users, without a suitable software, to manipulate by hand. However, in the PScan software structure, all the hardware driver level control, are integrated into a LabVIEW project package, with front panel parameters open to the PScan

GUI through ActiveX protocol, which enabled the synchronization control at the GUI level for general users.

Here the design detail of the PScan software will be explained. In the left yellow colour square, it is the structure of PScan software. From top to bottom, are the sequence of running and using PScan. First, because PScan is based on MATLAB, so the primary function is a MATLAB M file, which can be executed directly in the MATLAB environment. After the running of the PScan, it will initialize its functions, especially setting the calling function from ImageJ by MIJ, the initial value setting of imaging speed and display color threshold, and the default saving place. In the following, it comes to the function modules that PScan provides, which we grouped into four groups, as scanning group, frame grabbing group, live-view processing group and the data management group. These four groups can be seen as the classes in object-oriented programming. Through this group, the control manipulations operation is decoupled so that change values or settings in different groups will not affect the functionalities in different groups. For example, when doing imaging experiment in biological experiments, changing the values in scanning for achieving different zooming will not affect the real-time display in the live-view processing group, which guaranteed the imaging experiment would not be disturbed by operating the PScan. Besides, this decoupled design increased the robustness of PScan and decreased the breakdown or crashing probability, and it can reliably respond to different running orders from the users with unusual using habit.

In the scanning part, PScan gets access to the different scanning mirrors by ActiveX protocol to call the LabVIEW VI program written for the NI-DAQ equipment. Here in our current design, it is a PCI6110 device that does the DAQ function. The scanning module includes a polygon mirror, a deformable mirror (DM) and a virtual conjugated GM pair. The role that the DM played in our system will be explained in detail in the following AO chapter and the volumetric imaging subchapter.

In the frame grabbing part, PScan gets access to the Matrox Solios eA/XA board through a DCF file. Because Matrox provides a library (MIL) provides a library of functions for image grabbing and analysis, PScan can also directly read the executable file written in C/C++ for

specific imaging tasks. For example, the high SBP image requires a separate display window and direct control of the frame grabber, so PScan will enter into C/C++ executable file environment when we apply the zoom function. Otherwise, for standard SBP image (512 x 512) PScan will use MATLAB GUI's image axis function to display the results. The settings in the image grabbing group are about frame size formatting, real-time preview control, display color bar formatting and acquisition length control. All these functions are supported by the Matrox board, due to its specific design for professional image capture, which saves time and effort in image formatting compared to using only high-speed ADC devices.

In the live-view processing part, it includes three critical functions, which are image alignment, image averaging and wavefront sensing for aberration correction. The image alignment is for compensating the jittering and shift during in vivo imaging experiment caused by the breath and heartbeat of the animal. So, it is a necessary module for in vivo imaging experiments. Here in PScan, we achieved it through the MATLAB script, taking usage of MATLAB's powerful matrix calculation ability and concise programming style. The detail of this function will be introduced in the next subchapter. The second function in this group is the averaging function. This function is essential since, during the imaging process, noise from the background stimulated fluorescence and electronic stochastic noises from the detectors, contribute a background noise that would lower the contrast, thus making the image unresolved or even covered by the background. Most of this noise is generally Gaussian distributed so that averaging processing can eliminate most of the background noises. The live-view averaging ability is crucial in searching for the target area in the sample with weak fluorescence signal, which always happens in high scattering specimens. Thus, averaging is a crucial function in the multiphoton microscope, and here we used a standard averaging function package from ImageJ software. The interface between MATLAB and ImageJ is a third-party package called MIJ, and this interface bridges our PScan and ImageJ, which leaves a massive potential for extendibility for PScan in future applications. The third important function is the wavefront sensing module, in which we used a DM to achieve the iterative retrieval of wavefront information from the image. Recovery of the lost wavefront phase from a single detected

intensity image is a significant problem in modern optics research [165]. This question intrinsically is an ill-posed reverse problem in mathematics.

In order to get a robust solution, a sequence of external disturbances and corresponding measurements are necessary. Here through the introduction of different aberration pattern generated by the DM, a quality matrix can be built, and the wavefront can be reconstructed from that matrix. The detail of this process will be introduced in the AO chapter. This function will be used for the following AO correction to cancel out the distortion caused mostly by the homogeneous sample. The function interface is through the serial communication port and driver software based on LabVIEW provided by the Thorlabs (US) company.

The last part of PScan is the data management function group. After obtaining the data generated by the microscope, there is a requirement to convert the raw data into the desired data format is clear and efficient, especially for our high speed, high SBP polygon microscope, which usually generates data sizes of tens of gigabytes after one in vivo experiment. A high-efficiency data management with some simple postprocessing will save a vast amount of time and facilitate further analysis of the data. Here in this group, the element four functions are saving, color conversion (gray to RGB), registration (sub-pixel alignment with fixed reference image), and deconvolution (blind deconvolution with the size of PSF). The saving structure in PScan is achieved through two independent saving routes in terms of saving time and increasing efficiency. One way is a fixed address, and it is a hidden string unreadable from the GUI, which will be the default route for the video acquisition process. The other route is a readable and writable string on the GUI, entirely determined by the user, and it will only work when the user chooses to save the file after the acquisition. It will then change the most recent acquired data into the desired address. This configuration facilitates the PScan progress without concern of addresses for each trial of acquisition. It leaves the decision after finishing the video grabbing process, thus providing enough flexibility in video capturing to save time lost due to the copying command, which will cost much time when the file size is big. Color conversion is because the raw data obtained by the Matrox is in grayscale. There is an automatic batch processing to convert all the files and subfolders in the main folder into an RGB colored file, which is more suitable for display.

The registration function here is designed for subpixel accuracy registration, which will cost more time compared to the live-view processing, but with improved performance. The details for this process will be explained in the following subchapter. The last function is deconvolution, which is a process of using the PSF information to redistribute the intensity of each pixel, thus to have a sharper image. This process is beneficial especially for multiphoton fluorescence microscope because TPA event is spatially confined. Thus deconvolution can be used to recover the model with more localized centres which make the image better represents the object with minimized blurring. If the fluorescence can be decoupled in the temporal domain, each retrieved fluorophore centre can be used to reconstruct the super-resolution image [9, 10], which is the principle of PALM/STORM microscope.

Finally, PScan's first version GUI is shown in Figure 2-17, here we called it version 1.0 to mean that it is the first version of the developing software, and there are following versions with increased functions and interfaces of other devices, for example, the extra AO correction for polygon microscope. Here in our PScan 1.0 GUI, the image display area has four windows, which are red channel on the top left, a green channel on the top right, combined two-color channel on the bottom left and averaged channel on the bottom right. The control panel is on the left side of the GUI window, which includes functions of acquisition group from the top, followed by color bar tuning slides, and interested digital ROI choosing, then the acquisition length and repetition rate control, then the scanning control of the GM, then the imaging formats, which varied from 512 x 512 to 32 x 512 pixels. The button group on the left side below the imaging display video are for controlling the imaging speed and polygon rotation speed. The right side is the data management button group, which is used to convert the saved gray folder of files into RGB files. In the bottom area of the GUI, the left side is the saving address area, with the top string input bar for writing address, the bottom string bar for the name of each file. Here the folder name will be automatically set to the date of the experiment time, and each saved file will have prefix indicating the time stamp of the file, thus automatically making the file distinguishable without requiring explicit naming. The right side of the bottom area is for status display, the string bar showed the last saved file's name and

address, and below that bar is the FPS rate, the system's current time and the working status (the progress of acquisition).

Here I discussed the design idea of PScan software, which is mainly based on MATLAB and LabVIEW, for achieving the purpose of a high accuracy control software. This process decoupled the functions and grouped them into different function classes, thus enabling the manipulation for a complex polygon microscope system through a tidy graphical user interface without configuration requirement. In the next subchapter, I will discuss the packages of different function modules in PScan and the detail of the image registration function.

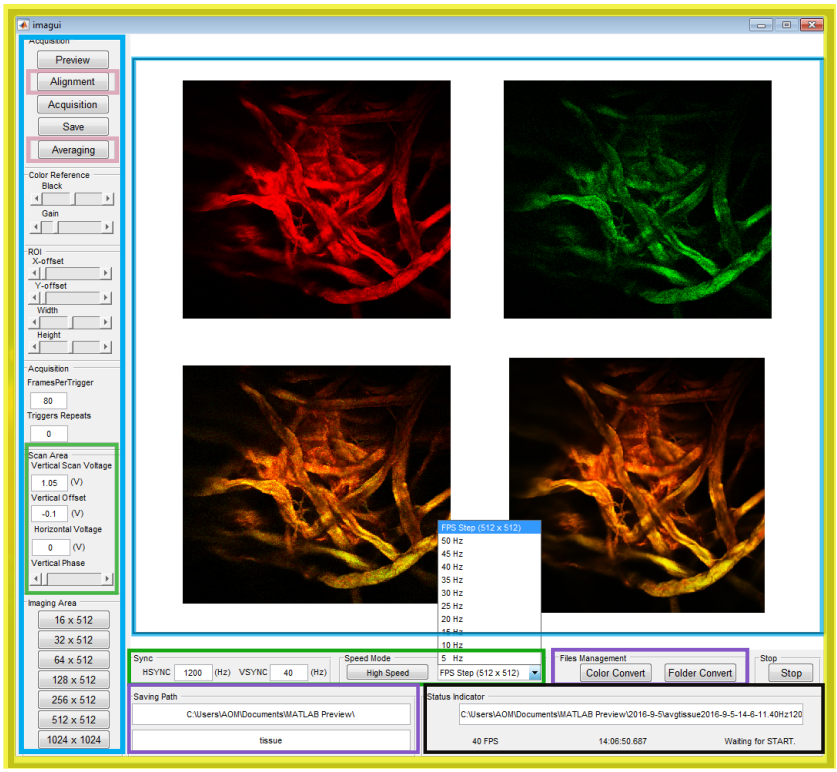

Figure 2-17 The GUI of PScan 1.0. The four channels are display as red, green, combined and averaging channels.

2.5.4 PScan Packages

After building up the PScan framework, the supporting packages will provide the ability to extending to more functions. The basic idea is to make the framework as the trunk and the extra

add-on functions as the branches. Together they constitute an adaptable control software system. The method of building and integrating the packages into PScan is based on simple oriented programming process, through the using of the “call back” function inherited in the MATLAB GUI compiling environment. MATLAB provides the property setting of component types and behaviours for the design. Each object on the GUI has the corresponding call back function as in the MATLAB script. So with the developing of microscope hardware, adding new packages of function can be easily achieved without affecting other existing functions or components.

There are several essential function packages in PScan. These are the averaging function, the deconvolution function, the image registration function, the wavefront sensing function, and the AO correction function. Some of these have been discussed in the framework section, while the wavefront sensing and AO correction function will be discussed in the next AO chapter. Here in this part, I will introduce the image registration function, which is a demanding function required for in vivo experiments. The physiological motion caused by native contexts such as heartbeat, respiration and peristalsis will degrade the in vivo imaging performance significantly, especially in the imaging mode which needs long integration time for constructing a single image like fluorescence lifetime imaging (FLIM) [166]. There are a few possible solutions, such as fixing the body by external constraints. One straightforward way is to increase the imaging speed to video-rate so that the motion effect for every single frame is small enough, and the frames with a jump shift induced by each heartbeat event can be dropped off from the image sequence frame without losing temporal information. In some commercial microscope systems, the heartbeat is monitored and used as the trigger signal for imaging acquisition to avoid the movement window. On the other hand, without relying on stabilization tools or external hardware monitoring circuits, the use of registration algorithm provides an alternative option to remove the motion artefacts at even subpixel precision [167].

The basic principle of image registration we used in PScan is based on cross-correlation, which can be done by using the Fourier transform. The cross-correlation processing will give rise to a coordinate of the shift value, in terms of the image pixels. After this, the coordinate is used to align the image back to remove the lateral shift. One factor that will affect the

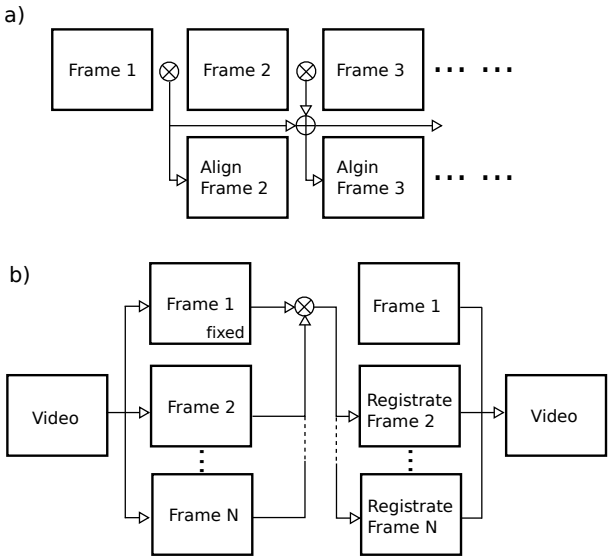

Figure 2-18 Principle of image registration function in PScan. a) Flexible reference image registration for live-view processing. b) Fixed reference image registration for high accuracy alignment in post-processing.

registration performance is the choice of image frame as the reference. Here in PScan, we used two different references for image registration. The two schemes are shown in Figure 2-18, which act as a refreshed or non-refreshed reference. For the refreshed registration frame, as shown in Figure 2-18 a), each time, the cross-correlation process is conducted between the two sequence frame, and the value used to align the frame is an accumulated value with the previous cross-correlation results. This type of registration will have the ability to track movement with the flexibility of being adaptive to purposed movements, like in following the stage movement to reach to the interested imaging area, while still smoothing the jittering shift for sample stabilizing. This process is assumed as a Markov process, which means the required registration is only related to the current state, without concern of the initial time point or future time point. Thus it is well suited for real-time live-view imaging. Another registration scheme in our PScan uses a fixed image frame as the reference frame, and all the other frames in the sequence are cross-correlated and aligned to that single frame. In this process, since the reference frame is fixed, the registration will give a static output without the tracking ability to any external movement, which means it will have a better stabilizing performance but does not respond to

dynamic FOV searching movement, so it is mostly used in the post-processing with a clear reference target.

The registration processing results are shown in Figure 2-19. The imaging specimen is a rhodamine dye injection labelled blood vessel in B6 wildtype mouse in vivo. During the observation process, the imaging speed is 40 FPS, at a length of 22 s. During this imaging experiment, in addition to the physiological movement, we also moved the sample through the stage to give a rapid and intensive shift to test our PScan registration schemes packages. Here in subpicture a), image shifts in X and Y direction with a unit of μm over the time are recorded. We can see that in addition to small repetitional jittering from the native context, at the time point of 11 s and 18 s, an intensive X and Y direction movement are introduced respectively. The averaged results of the whole captured image are shown in b), the visualisation is blurred and have a noticeable ghosting effect. c) is the image results using the flexible reference registration, it shows that there is still a trend in the movement during the imaging process, but not in a fast way. d) is the averaged process result from c), which again is blurred, but the ghosting effect is much less than b), which proves the feasibility of registration ability in the flexible scheme. e) is the results by fixed reference image registration, the movement effect has all been eliminated, with only jittering of a few hundred nanometres left. The averaged result is shown in f), with this level of registration, all the movement are compensated, and a sharp image of blood vessel is obtained. Without explicitly mentioning it, all the *in vivo* results shown in the following chapters in this thesis are processes with this fixed reference image registration method.

Overall, PScan software has reached our assumption of constructing a flexible control software with state of the art packages and imaging performance, which became the integal part of the system. PScan facilitated all the following biological experiments, allowing generation and capture of image datasets in a straightforward and efficient way.

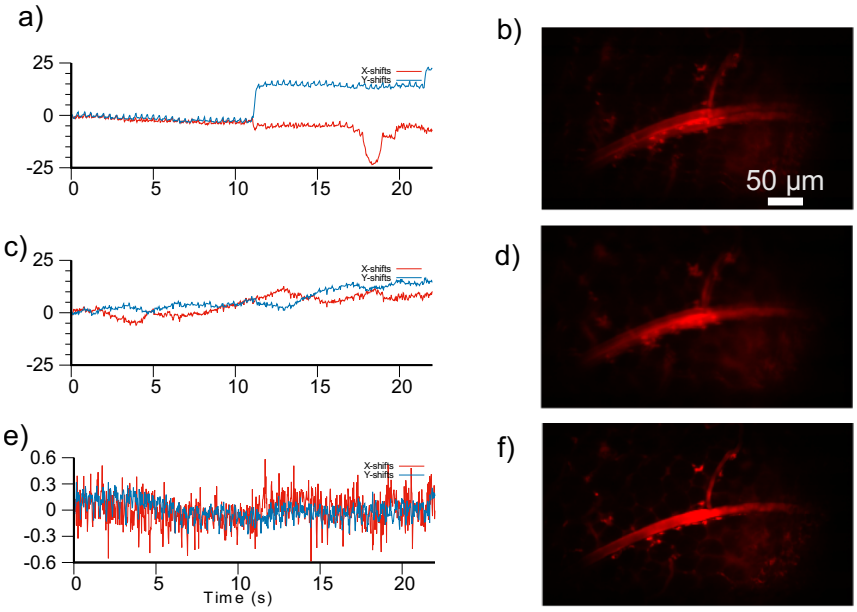

Figure 2-19 Image registration results. The data is from a blood vessel in vivo imaging video experiment. a) The calculated image shift of the acquired video by cross-correlation, with the unit of μm, over 22 seconds length time. b) Averaged image from the source file without registration. c) Calculated image shift of the same video after flexible reference image registration. d) Averaged image results after the flexible registration process. e) Determined image shift of the same video after fixed reference image registration. f) Averaged image results after the fixed registration process.

2.6 Imaging Results of Polygon Multiphoton Microscope

In this subchapter, I will show some of the results and the images we obtained. First, we used 210 nm beads to measure the PSF of our polygon multiphoton microscope. The illumination wavelength is set to 800 nm; the measured FWHM is about 0.75 μm. The results are shown in Figure 2-20.

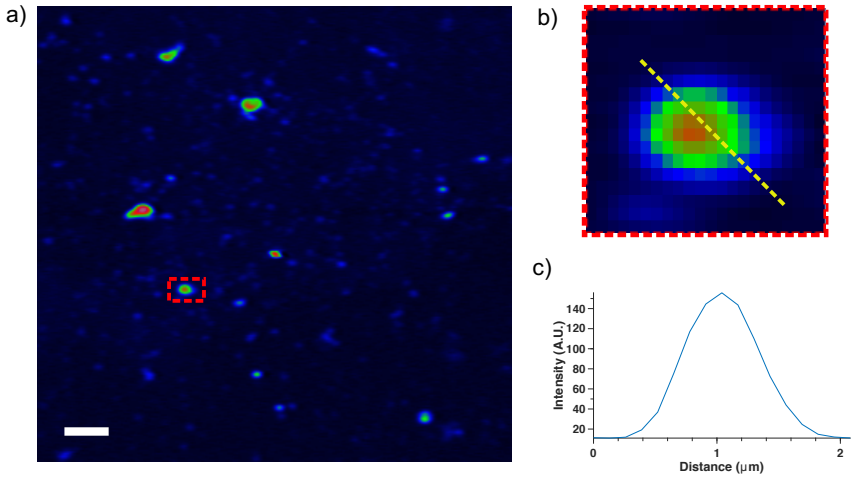

Figure 2-20 PSF measurements of polygon microscope. a) is the image of 210 nm beads. b) is the zooming image of the square area. c) is the intensity line plot corresponding to the yellow dash line in b). Scale bar is 5 μm.

Then we use pollen grains as a static sample to test the flexibility of our microscope. As we discussed before, the significant flexibility of polygon scanner and customized control system provides us with the optical zooming, dynamic scanning imaging speed and sectioning speed control. They are shown in Figure 2-21. The optical zooming is done by slowing down the scanning speed while keeping the pixel clock the same value, and this will generate more pixels. In default speed, we set FPS to be 40, and with 512 lines in vertical to constitute the image, plus 38 lines as the back and front porch as well as the synchronisation lines, therefore 540 lines in total, which is an integer of the 36 facets, thus the lines are sync to the image. In horizontal, we set 512 pixels for each line. The rotation speed of the polygon is 600 r/s (revolutions per second). The pixel clock is about 20 MHz, and will be generated from the grabber intrinsically. Currently, 5 times, 10 times, and 20 times magnifications are selectable. The scanning speed for each one is 300 r/s, 150 r/s and 75 r/s. The pixel clock frequency is 30 MHz for all of them. When the speed is slowing from average value 600 r/s down to 75 r/s, the pixel number of horizontal line are multiplied by 5 to 20 depending on how slow the speed can be, and at the same time, the vertical scanning voltage of GM are decreased by the corresponding times of 5.

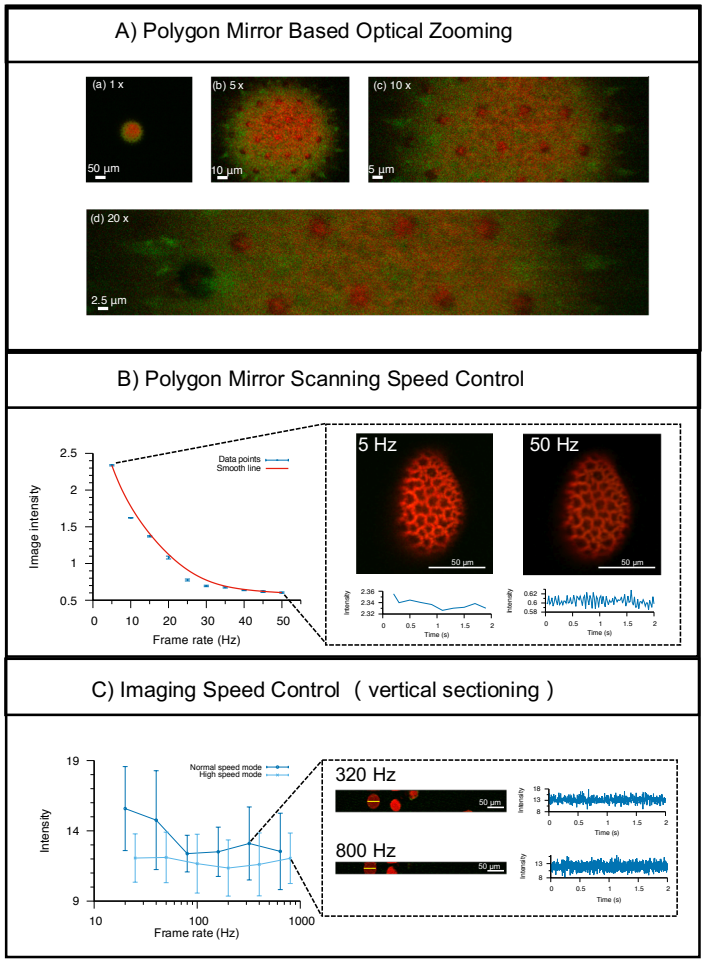

Figure 2-21 Imaging flexibilities of the customised polygon microscope. (A) is the optical zooming results, with sub-images from magnification rate increased from 5 to 20 corresponding to insets a) to d). (B) The image with different polygon scanning speed. The 2s averaged image intensity are plotted. Subset showed the averaged image of pollen sample at 5 FPS and 50 FPS. The intensity of single frame over 2 s duration acquisition is shown below the image. (C) The imaging speed control results of pollen sample by changing the GM and VSYNC. The intensity plot shows two lines of different polygon scanning speed. One is average speed, the other is high speed. With changing of frame rate, even if the frame rate changed a lot, the intensity maintained in a level determined by the polygon speed. The inset demonstrates the averaged images of 320 Hz and 800 frame rate at normal polygon speed and high polygon speed respectively. On the right, intensity plot of time sequence during the 2 s period are plotted.

In this way, we achieved the zooming of the image, and the results are shown in Figure 2-21 (A). The zooming function is an anamorphic scale zooming, which means for one single

frame, more pixels are mapped on the polygon scanner direction rather than the vertical GM scanning direction. Image FOV can be expanded through assigning the GM scanning a step waveform voltage signal with a step value of amplitude and return after integer steps based on the size of the interested imaging area. Zoomed images represent the increasing of sampling points of the fluorescence signal from the PMT. The zoomed image in our system is different from digital camera zooming; it is not an empty magnification. The most significant difference is that the zoomed function does not shrink the FOV. Hence there is additional information, one straight forward-thinking of this is it increased the number of measurements, and the more the measures, the higher the certainty. With more measures, the system's noise can be suppressed more easily with the following image processing method, such as deconvolution, in which high pixel count image will generate a better-resolved image. Besides, in terms of achieving the potential highest resolution of the system, one of the necessary condition is that the pixel size needs to be at least not more prominent than half of the estimated resolution (Nyquist Sampling Criterion). Cause the zoomed image has the same FOV, it means the pixel is getting smaller in the corresponding scale. Therefore, this zoomed image is helpful for potential super-resolution imaging requirement.

The dynamic control of the polygon scanning speed enabled the flexible imaging quality by varying the dwelling time of the laser, which allowed to get more photons in case of weak fluorescence or photon sensitive fluorophores, the results are shown in Figure 2-21 (B). The frame rate is changed from 5 FPS to 50 FPS by changing the rotation speed of polygon from 75 r/s to 750 r/s; the maximum can be up to 900 r/s with 60 FPS rate. The pixel clock frequency is also changed from 2 MHz to 20 MHz correspondingly. The average image intensity decreased from 2.5 to 0.5; the intensity shows a linear relation with scanning time from the section of 5 FPS to 25 FPS part. Without changing the bandwidth of the trans-impedance amplifier, averaging of frame acquired at full speed scanning at the same time interval will have the same performance in terms of signal to noise ratio. However, the benefit of varying scanning speed is it provides the flexibility for other specific applications, in which laser dwelling time per pixel is essential. Such as laser induced heating effect or optogenetic stimulation. In those cases, a slow-scanning will increase the dwelling time, which allowed

delivering more pulses per pixel. While at high-speed mode, cause the laser repetition rate is fixed, the pulse per pixel is less, this lack of laser pulse will depress the stimulation efficiency. But for specific applications, like the total dwelling time is a sensitive factor, then slowing down the scanning to increase the dwelling time per pixel will be necessary. For example, for laser induced heating effect or optogenetics application.

In addition to the polygon scanning speed control, the dynamic control of GM scanning amplitude and programmable format of frame grabber enabled the flexibility in imaging area and imaging speed. This function can change the image speed at the ratio of the portion of the area. This function is vital in the microscope to observe the biological process at the different temporal resolution. This is what we called “temporal zooming”. The results are shown in Figure 2-21 (C). The imaging speed is increased from 5 FPS to 800 FPS linearly to the ratio of the vertical scanning area. There are two lines in the plot, for each line, the polygon speed is the same, but a difference between them in polygon speed. So we assumed the same scanning speed would keep the image intensity at the equal value average value, but high-speed scanning polygon line will be less than the slow one. The results exactly showed this phenomenon. This stability in intensity and flexibility in imaging formats is an essential function which I will use in the following multi-segment AO correction.

Another imaging result of the sample slide is shown in Figure 2-22. Mouse kidney slide was imaged by default 512 x 512 imaging mode and 10240 x 10240 pixels mode respectively. It shows that through the control of polygon scanning speed and pixel clock rate, combined with GM vertical stepping control, high contrast image is obtained with less time than the fixed control. It also shows that deconvolution improves the image performance in high SBP mode; the super high SBP provides the potential of further extendibility to super-resolution processing abilities [168].

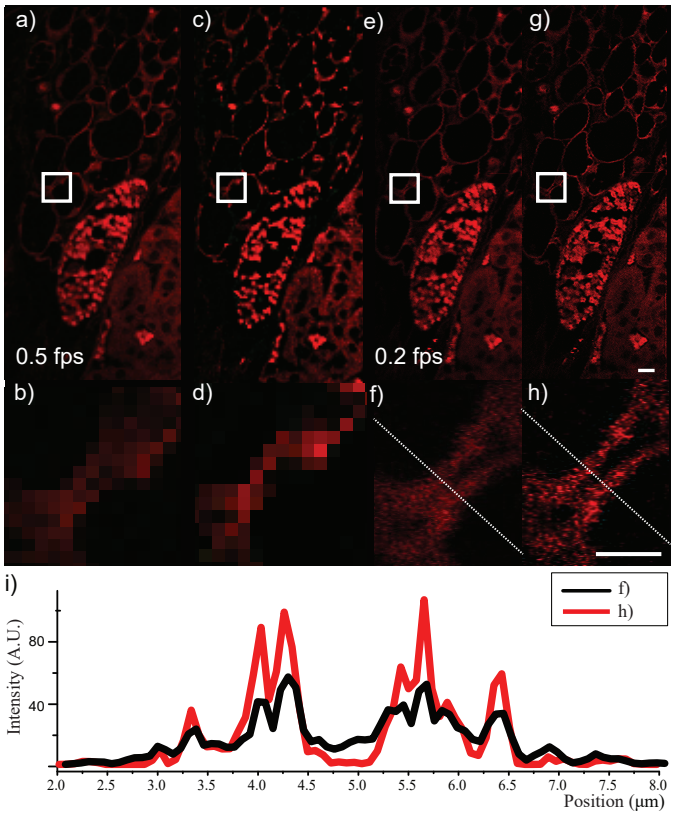

Figure 2-22 The high contrast image of the rhodamine stained mouse kidney slide. a) The 2s averaged image of the sample at default mode with 512 x 512 pixels and 20 FPS rate. b) The zoomed image of the white square area. c) blind deconvolution of a). d) The zoomed image of the white square area in c). e) A single image of 20 x magnification imaging mode, 20 images are weaved into the same FOV by the vertical scanning control of GM. Pixel size is 10240 x 10240 at 0.2 FPS rate. f) Zoomed image of the white square in e). g) Blind deconvolution of e). h) Zoomed image of the white square in g). i) Line plot of the intensity of the dashed line in f) and h).

Now we have shown the flexibility of the system in the control spatial resolution, temporal resolution and phototoxicity. Here we applied it to live biological samples. The potential actions of neurons from brain slices were imaged. The brain slice is cut from a rat, stained with cal520AM dyes. The results are shown in Figure 2-23 (A). In Figure 2-23 (A), we imaged the brain slice at 40 FPS over 3 minutes and extracted the time serial neuron calcium signal intensity, the ratio of relative intensity over baseline intensity is drawn.

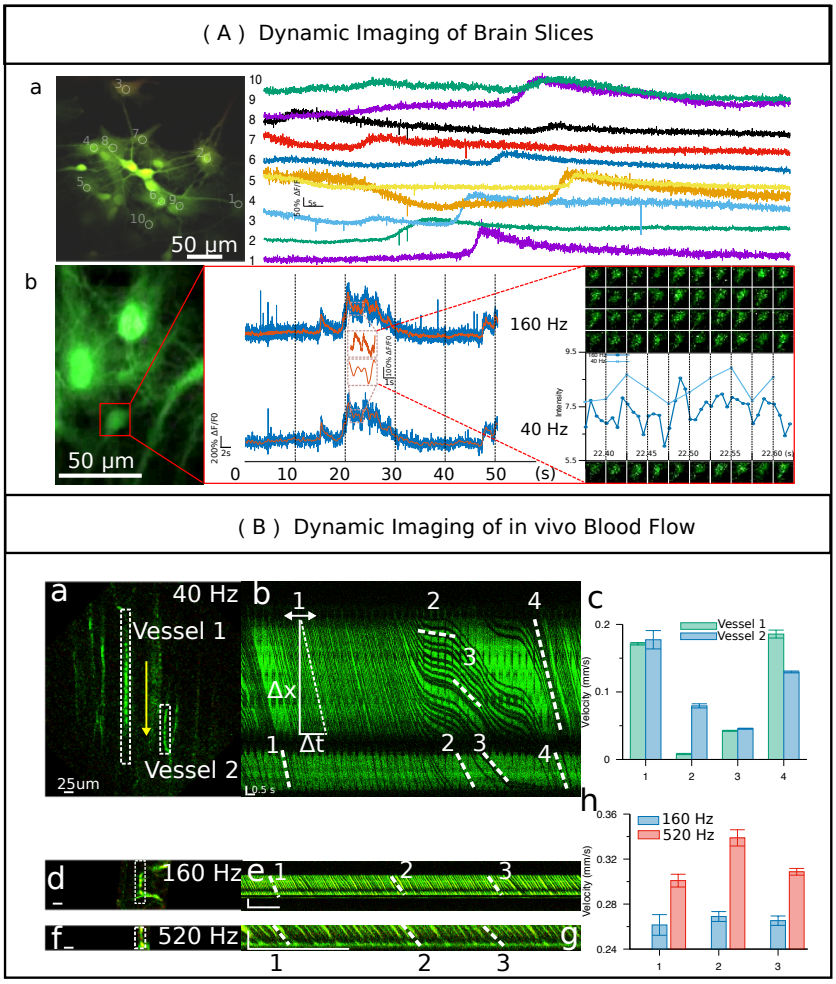

Figure 2-23 (A) Imaging of rat brain slices with different imaging speed. a) The imaging with 40 FPS and 10 neurons are selected with relative intensity plot on the right. b) The imagery with 160 Hz of the same brain slice. Line plot of bot the raw 160 Hz speed and decreased sampling rate of 40 Hz are shown in the middle. It shows that lower imaging frame rate will get lost of the neuron signals. (B) Imaging of in-vivo mice blood vessels. a) The capillaries imaging with 40 FPS. Two vessels are chosen. b) The line plot of the selected areas, label 1, 2, 3, 4 are the four chosen slopes being used to measure the speed. c) The bar plot of the measured RBC velocities from the four selected sections of the two blood vessels. d) The same mice with imaging rate at 160 FPS. e) The line plot of the chosen area. f) The image of the same area in d) but with 520 FPS speed. g) Line plot of the selected area in f). h) The bar plot of the measured RGB velocities from the three segments labelled in e) and g).

In Figure 2-23 (A) b, we narrowed down the scanning area to achieve temporal zooming, since we want to get more calcium signals rather than the morphology. We use 160 FPS

imaging speed to record a 1-minute video, extracted the chosen dendrites area intensity plot over time, and also draw another line with 40 FPS by decreasing the sampling rate of the raw signal, and the results showed that some of the transient signals is lost in low imaging speed. In (B), we implement our microscope to look at the blood flow of mice in-vivo. The mice are anaesthetized by ketamine solution through intraperitoneal injection (IP), FITC dextran is injected through retro-orbital injection to the vessels of the eye. Imaging speeds are 40 FPS, 160 FPS and 520 FPS. Blood flow speed was measured, the increase in speed increased the slope in the line plot, which therefore enhanced the speed measurement accuracy. The measured red blood cell (RBC) velocities in the capillaries have a range from about 0.1 mm/s to 0.3 mm/s, which is well-matched with the blood flow rate of mice [169, 170]. The measurement is done by getting the line plot of the vessel over the frame time sequence, so to get an image with the time as x-axis and distance as y-axis. Then the slope of the cell tracking line is the velocity.

Comparing to the commercial polygon scanning microscope, such as bliQ's Video-rate Microscopy System, which has adjustable line scanning rate from 9 to 18 kHz with frame rate varied from 35 FPS to 562 FPS at pixel count of 1024 x 512 and 1024 x 32 respectively [171]. Our PScan polygon microscope has a broader line scanning rate (2.7 kHz to 32.4 kHz), flexible spatial-temporal zooming function with pixel count up to 10240 per line, which is 10 times larger than the current commercial system.

Here we showed how to design and build a flexible polygon based multiphoton microscope. This microscope can be tuned with flexibilities in spatial zooming, temporal zooming and phototoxicity control. Currently, due to the occurrence of different fluorophores and optical genetics technique, flexible imaging speed and controllable laser dwelling time is becoming more and more critical. Such as the recently published kilo Hertz imaging methods [172]. The control of laser dwelling time and imaging speed will be the parameter that a laser scanning microscope should be able to change. For our polygon microscope, the flexibility of scanning time, with up to 32.4 kHz line rate and linear scanning area, outperforms the most used resonant scanner, which has fixed scanning speed and nonlinear scanning speed. Besides, polygon's smooth stitching and extending ability will be easier to integrate with other fast

imaging technique to increase its imaging speed more. In the next, I will demonstrate how this polygon scanning microscope be extended to video-rate AO correction and working at extended large FOV.

2.7 Contributions

Woei Ming Lee supervised the polygon microscope project. Vini Gautam and Vincent Daria provided the brain slice specimen. Cathy Gillespie provided the mice kidney sample.

Chapter 3 Raster Adaptive Optics for Multiphoton Microscope

As discussed in Chapter 1, scattering tissues distort light beam travelling into the sample and distort the final image. This effect will give rise to the constraints of spatial resolution and imaging depth. However, the measuring and correction of aberration might introduce extra exposure time, thus consume the photon budget. In this chapter, I shall present the AO technique, which is an aberration correction method that seen success in telescope technology development. However, it is essential to note that there are significant technical differences between the telescope and microscope on the types of aberration sources and the correction method. Hence, there are still challenges to be addressed before AO technology can be widely used in the microscope.

Theoretically, the resolution of a microscope is the Abbe diffraction limit,

$$d = {\lambda}/{2NA}, \qquad \text{Equation 3-1}$$

where d is the resolvable distance, λ is the wavelength of light, NA is the numerical aperture of the objective. The microscope that can reach this limit is called the diffraction limit system, which indicates that the wave nature of light determines the resolution. However, the diffraction limited system can only happen in theory, the imperfection of lens and alignment, as well as the sample heterogeneity, will always break the diffraction system condition. One way of improving the imaging performance is using AO, to actively compensate the aberrations both from the system and the sample. The purpose of AO is just to refocus the light beam back to the focal point to generate a compact PSF after the objective by modulating the wavefront

of light according to the different imaging samples. Based on the Fourier optics, the PSF is a Fourier transform of the objective's pupil function of objective, as

$$PSF = |\mathcal{F}[\Psi(x,y)]|^2, \quad \text{Equation 3-2}$$

where $\Psi(\mathrm{x},\mathrm{y})$ is the pupil function. In ideal condition without aberration, the pupil function is a purely 2-dimensional circular function $Pupil(x,y)$ defined by the physical shape of the lens. However, in the real system, the pupil function will become a complex item with the phase component as

$$\Psi(x,y) = Pupil(x,y)\exp[ikW(x,y)], \quad \text{Equation 3-3}$$

where k is the wavenumber and $W(x,y)$ is the aberrated wavefront need to be compensated. If the pupil is circular, then $W(x,y)$ can be expressed as the vector of Zernike modes as we explained in chapter 3. Noted that this wavefront is a spatial variant value conjugated to the pupil of objective. Therefore a pupil plane conjugated AOE can be used to cancel out the aberration in the imaging process, which is a standard method of AO in the microscope.

But there are few limitations in pupil plane conjugated AO microscope, one problem is the shift-invariant is not maintained during the scanning process [173]. In other words, the wavefront at the pupil plane is time dependant value corresponding to the different spatial positions at the image FOV, single correction pattern cannot work with varying scanning angles, and also separate sample area introduces various aberrations to distort the beam differently. The area size with the same planarity is called isoplanatic patches. So the propagation of light will be shifted at a different time and different FOV thus the correction wavefront need to updated corresponding otherwise the whole imaging performance will be dropped, AO can even worsen the imaging quality if being misused. So, a static wavefront correction cannot meet the target of aberration correction for optical microscopes. There are several methods for solving this method, for example, the use of image plane conjugated microscope [174], or pupil segmented microscope [175]. But all require high accuracy alignment and careful tuning of the system, which is hard to achieve in most of the current existing microscope systems.

Here I proposed a method, that not only can solve the practical FOV problem but also can be allocated efficiently into current laser scanning microscope. I called this technique RAO, short for raster adaptive optics. RAO is a method that can work at video-rate, with imaging performance improvement over full FOV (450 μm x 450 μm), which fulfilled the most working requirement for current laser scanning fluorescence microscope. Moreover, further extended FOV can be achieved by integrating RAO and GM steering, with corrected objective aberration. In the following sections, I will first introduce the background knowledge about AO. Then I will demonstrate the implementation of pupil conjugated AO into polygon microscope, and add the indirect wavefront sensing method we used for wavefront correction. The RAO methods will be presented in the last subchapter.

3.1 Removal of Optical Aberrations

The shape of the focus of multiphoton microscopy is determined by diffraction effect and nonlinear absorption, as shown in Figure 1-9. However, diffraction limited spot can only be achieved at the ideal condition. The actual resolution is limited by the induced aberration from both the optical system and the imaging sample. The imperfections during the optical components manufacturing and optical system alignment result in the system aberration, and varying refraction index over time and space in the inhomogeneous biological tissue induces the sample aberration.

System aberration can be analyzed by ray tracking and corrected by lens design [176]. Scan lens and objective lens are both designed with consideration of field curvature correction, which is related to the spherical aberration. Objective lenses, the most crucial device in the microscope, are also being designed in consideration of chromatic aberration. For example, the widely-used Zeiss W "Plan-Apochromat" 20X (1.0 NA) objective, can correct field curvature and spherical aberration over different colors (3~4). System aberration is usually stable over the experiment. However, sample aberration is highly dynamic and will vary in time and space [177]. Therefore, suppressing sample aberration requires the correction method to be active and rapid.

Adaptive optics (AO) is a technique to remove sample induced aberration. Babcock first conceived it in 1953. Its initial target is compensating the atmospheric disturbance in telescope [178]. Now AO has become a standard configuration in modern observatories, especially for the giant telescopes with scale size of over a few meters [179]. Despite the extreme success of AO in astronomy, its application in the microscope has still been under-explored and not routinely available in biology labs. There are a few reasons for this. First, the aberration in the microscope is fundamentally different from the telescope. In telescopic application, most of the optical aberrations in the atmosphere are highly dynamic in time [180], while in the microscope, the majority sample aberration is varied mostly over the space [181]. Second, the positioning of wavefront sensor in the microscope is hard to achieve, there is no way of putting a wavefront sensing device between the sample tissue and the objective like what the AO in telescope does [112, 182, 183]. The differences between telescope and microscope in imaging and encountered distortion are shown in Figure 3-1. In Figure 3-1 a), the atmospheric turbulence was varying at ms time scale and distorted the star image captured by the telescope. In Figure 3-1 b), in the microscope area, the heterogeneity changing over micrometre gives rise to the aberrated tissue image.

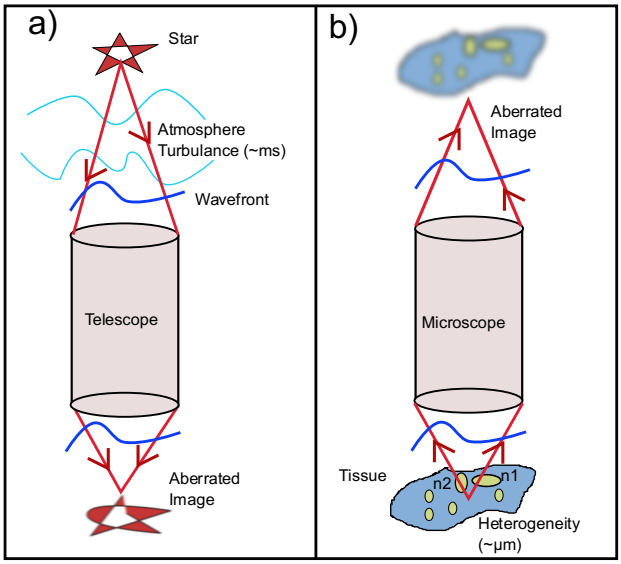

Figure 3-1 Schematic plot of imaging aberration in telescope and microscope scenario, in which the significant difference is aberration source in the telescope (a) is atmospheric turbulence which varied

fast in the temporal domain, while biological aberration in microscope (b) is from the heterogeneity in the tissue which changed rapidly in the spatial domain.

3.1.1 Aberration Measurement

The aberration in the optical system can be illustrated by generalised pupil function [184] as,

$$Pupil(\rho,\theta) = A(\rho,\theta)\exp\left(i\Phi(\rho,\theta)\right). \quad \text{Equation 3-4}$$

In which, ρ,θ are the coordinates, A is the amplitude, Φ is the phase of is the total wave value at the unit pupil plane. This wavefront can be described by Zernike polynomials [185] as,

$$\Phi(\rho,\theta) = \sum_{n,m} a_n^m Z_n^m, \quad \text{Equation 3-5}$$

here a_n^m is the Zernike expansion coefficient, n and m are the radial and azimuthal orders of Zernike polynomial Z_n^m. Zernike polynomial is a complete unit orthogonal basis in the form of a product of the radial polynomial and trigonometric function as

$$Z_n^m = c_n^m R_n^m(\rho)\Theta(m\theta), \quad \text{Equation 3-6}$$

where c_n^m is the normalization factor, $R_n^m(\rho)$, $\Theta(m\theta)$ are the radial and angular function on the exit pupil. The n and m should obey to n-$|m| \geq 0$ and be even. The Zernike polynomials represent the classical aberrations, for example, Z_2^{-2} , Z_2^0, and Z_2^{-2} are astigmatism, defocus and oblique astigmatism aberration respectively. For circular symmetry imaging system, the wavefront distortions can be adequately described by a vector of expansion coefficients $\{a_n^m\}$, as the combination of the aberration modes. In a perfect imaging system, the Zernike coefficients vector modulus should be 0, so the value of Zernike coefficients can be used to compare the severity of different aberrations. The two widely used indicators are variance and root mean square (RMS) of the wavefront, fortunately, with the orthogonality and normalization properties of Zernike polynomials, they can be simply calculated as

$$Variance(\Phi) = \sum(a_n^m)^2\,,\quad RMS(\Phi) = \sqrt{\sum(a_n^m)^2}, \qquad \text{Equation 3-7}$$

with a unit of rad. Zernike polynomial has been successfully applied to recover optical distortions in biological tissues such as neuronal tissues [165, 186, 187].

The wavefront measurement method in the microscope can be grouped as direct wavefront sensing and indirect wavefront sensing [112]. Direct wavefront sensing is based on the using of wavefront sensors. The representative wavefront sensor is the Shack-Hartmann wavefront sensor (SHWS) [188]. SHWS uses an array of small lenses (lenslet) to segment the pupil of an imaging detector (camera), the camera will then get the focus of each small lens, the lateral shift of the focus image from the precalibrated centre, will be used as an estimation of the wavefront slope. The integration of the slope will reconstruct the shape of the wavefront. The working principle of SHWS has been shown in Figure 3-2.

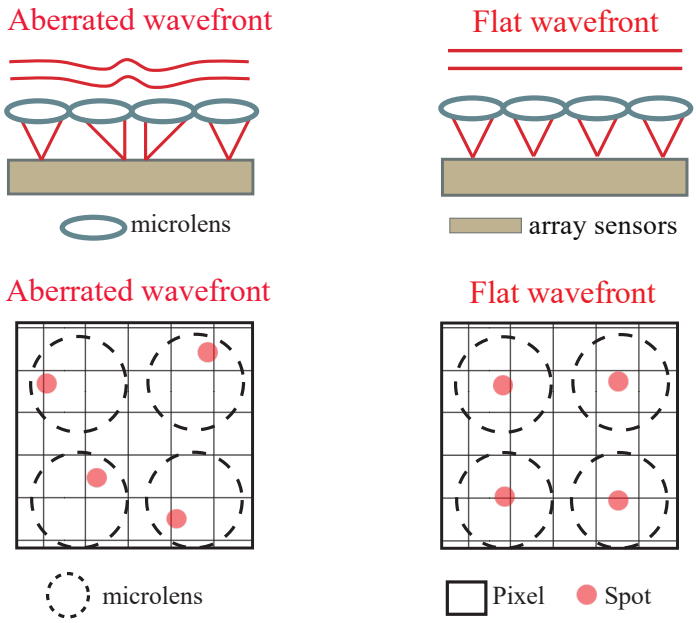

Figure 3-2 Schematic diagram of the SHWS Principle, in which the flat wavefront is the reference wavefront, its focus position after the microlens will be calibrated as the centre. For aberrated

wavefront, the focused beam after the microlens will shift away from the precalibrated centre, which provides the quantitative information of wavefront shape.

SHWS has been broadly applied to the telescope with its advantage of high detection bandwidth, with the capability of close-loop working with wavefront modulators. It has been applied to different types of microscopes, such as confocal, multiphoton and lattice light sheet [156, 189-191]. However, SHWS requires a guide star for the measurements, either using fluorescence protein [189], exogenously introduced beads [190] or TPA guide stars [192]. Moreover, the SHWS wavefront sensing cannot resolve light from different depth, which will affect the measurement accuracy in thick tissues, especially when the fluorescent signal is weak.

Given this, the alternative solution is indirect wavefront sensing, which estimates the phase of light from intensity image itself through the iteration process [112]. There are few methods proposed, one is using the image metric (brightness, e.g.) as the optimization guide, and make the wavefront modulator like deformable mirror (DM) to introduce different types of Zernike polynomials sequentially, through hill-climbing algorithm, the coefficients vector with peak value of the image metric will be reached [193-195]. This method has been applied to the multiphoton microscope [196] to look at embryos with improved image quality. Alternatively, segmenting the BFP by masking the SLM, then retrieve the wavefront slope from the deviation of the sample from the desired place [197]. This method had been applied to AO multiphoton microscope looking at mouse cortex *in vivo* [198]. The limitation of indirect sensing is the iteration process costs extra exposure and increases the risk of photobleaching.

3.1.2 Aberration Correction

For correcting the measured wavefront aberration process, usually, a one-step feedback compensation are delivered to an adaptive optics element (AOE), with the reverse value of measured aberration coefficients vector $\{a_n^m\}$ [199, 200]. Since the aberration is modelled at the exit pupil, the AOE will be positioned at the conjugated pupil plane as well. The allocation of AOE can also be different in different types of microscopes. For example, in the lattice light sheet, the excitation path aberration is corrected by an image plane conjugated SLM [156].

DM and SLM are the two prime AOEs for aberration correction. The working principle of DM is imprinting a wavefront (path length difference) onto the incoming optical beam by changing the shape of the mirror [201]. There are a range of DMs each differ by the number of actuators and also actuation types such as microelectromechanical systems (MEMS) [202], magnetic [203] or piezoelectric [202]. These deformable mirrors can come either in the form of segmented mirror [201] or a continuous thin layer of the reflective membrane [202]. With low inertia of the mirror, DM could achieve high-speed actuation of up to tens of kHz with little chromatic aberration that is then suitable for video-rate laser scanning fluorescence microscope. For DM, the mechanical coupling between neighbouring actuators affects the fidelity of the overall wavefront, and each actuator has a limited height that can be achieved, known as the stroke. The typical stroke for DM goes from 3.5 μm to 50 μm. Most DMs are shaped to match the "negative" measured wavefront characterized by Zernike modes to remove the aberrations.

Spatial light modulators (SLM) is another popular AOE [204]. The phase retardation is achieved by summing the extraordinary and ordinary refractive index from programmable liquid crystal molecules. The alignment and tilting of liquid crystals, housed in the individual block (~ μm^2) are controlled using electrical currents. Each block of liquid crystals acts as a "phase pixel". Each "phase pixel" is distinct from each other and is around a few micrometres in area. Existing electrically addressed SLMs can provide millions of "phase pixels" that covers the entire laser beam of a diameter of tens of millimetres.

Furthermore, the combination of holographic projection methods (phase wrapping) with SLM provides almost limitless control over the magnitude of each stroke. Since there are no mechanical parts and minimal cross-talk between individual "phase pixels", SLMs are a suitable choice for high-resolution optical wavefront shaping. While each "phase pixel" is inertia-free, the rate of the orientation of each liquid crystal block takes time. The wavefront refresh rate of SLM takes around 10 to 100 Hz, which is several orders of magnitude slower than DM. A significant advantage of SLM over DM is the number of phase elements available. DMs have phase element ranging from 40 ~ 140 that is tailor to create Zernike modes, whereas SLM can project very intricate phase patterns that do not conform to the Zernike modes [187].

Aside from DM and SLM, there is a third class of micro-optical devices known as digital micro-mirror devices (DMD). DMD is a digital controlled programmable reflective mirror array; where each micro-mirror can be freely pivoted amount its principal axis through a twisting action. While DMD can accumulate a high density of mirrors as much as the number of "phase pixel" in SLM, it does not provide real phase retardation. Instead, DMD generates rapid amplitude change across any given incident optical beam by deflecting different parts of the beam away from the principal optical axis. This deflection creates a binary type phase hologram [205]. By imposing a binary set of holographic patterns, the outgoing higher-order diffraction pattern would possess an intended phase change, i.e. binary Lee hologram [206]. Overall, the final wavefront of the beam is a function of the distance from the DMD and the modulated complex amplitude [207]. Since the number of actuators on DMD is comparable to SLM and the switching speed is similar to the micromechanical actuators as DM, it can generate more complex wavefront shaping than DMs. A significant drawback of the technique is the diffractive nature of DMD, which reduces the overall optical efficiency by more than 40% [208]. DMD-based AO correction is typically used in single-photon fluorescence imaging where monochromatic laser source have minimal chromatic dispersion due to diffraction [209].

In AO multiphoton microscope, AOE is simply positioned at the excitation path, instead both detection and excitation correction in other microscopes like light sheet microscope [156]. The choice of AOE can be either SLM for high accuracy correction or DM for high-speed update. Both configurations of SHWS based direct sensing and image-based indirect sensing AO have been achieved in the multiphoton microscope [191, 210]. For direct wavefront sensing microscope, Joel Kubby and his co-workers built direct wavefront sensing multiphoton microscopes using either autofluorescence or fluorescence protein guide stars [211]; Eric Betzig and his co-workers utilized two-photon stimulated nonlinear guide stars with descanning strategy for high SNR wavefront sensing working at 14 ms update rate [191, 210]. On the other hand, in terms of indirect wavefront sensing, Martin Booth and his co-workers put forward the multiphoton microscope using image brightness as the metric, with minimum $2Zn+1$ or $Zn+1$ iterations for Zernike polynomials recover [195, 196, 212]. And both

fluorescence image and autofluorescence image are being able to use for correction metric [213].

All the AO methods mentioned above require using photons emitted from the sample as guide stars for the correction. Denk and his co-workers put forward the using of scattered illumination light with gated selection and interference measurement of the wavefront for AO correction [214, 215]. The principle is scattered light from different depth will have different arriving time to the detector, and the ultrashort pulsed laser source used in multiphoton microscope retains a temporal gate to filter out the scattered light from the focus plane.

A significant limitation in AO application is the working FOV (isoplanatic patch), which is dependent on the phase structure of aberration [173]. In the astronomy area, multi-conjugate AO (MPAO) was suggested for correcting the distortion of different atmosphere layers, thus to extend the FOV [216, 217]. In microscope area, model-based study and simulation results showed that MPAO could also improve the FOV of microscope [218, 219]. There are two reasons for applying wide FOV AO in the multiphoton microscope. First one single wavefront correction pattern cannot be applied to different areas, especially in the highly heterogeneous tissue sample. Second, the correction pattern at the pupil plane will be decorrelated by the sample's structure during the scanning. So even the sample is flat, beam with different scanning angle will have different wavefront, thus degrade the AO performance. Meng Cui and his co-workers tried both image plane conjugate AO multiphoton microscope and multi-pupil correction AO microscope to extend the FOV [174, 175]. In image plane conjugate AO, an SLM was allocated to conjugate the thick skull, microglia cell was resolved through the integrated skull without thinning it. Another approach is using a prism to split the beam to different areas of SLM at the pupil plane, as shown in Figure 3-2. In this way, the pupil plane is segmented into 3 x 3 grid; each grid corrects one area of the image of the same 3 x 3 grid. A 450 x 450 μm working FOV with maximum projection ability from different focus plane was done.

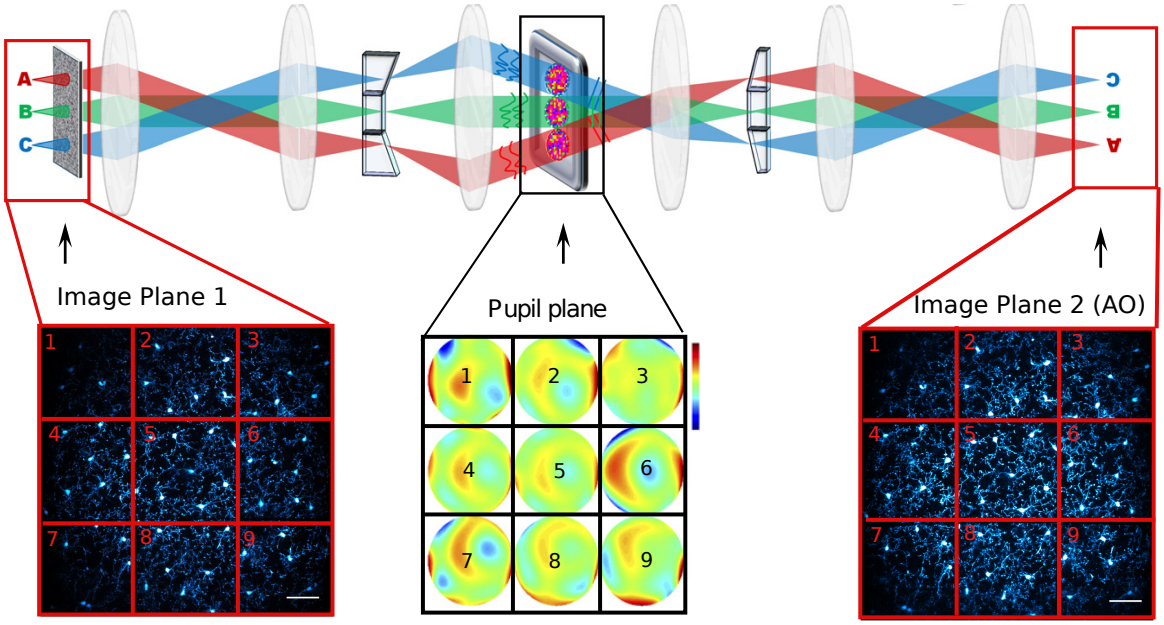

Figure 3-3 Schematic diagram of multi-pupil correction AO microscope, in which light from the image plane was split by a prism into a 3 x 3 grid and pass through different areas of the pupil. AOE is positioned at the pupil plane for aberration correction, and the prism will recombine these beams back to the image plane and compensate the dispersion as well. Image is adapted from [175] with permission.

AO technique is assumed can increase the imaging depth over hundreds of μm [94]. However, until now, AO has not been a standard technique in microscope area yet, it is still only accessible to optical expertise rather than the broad biological researchers. In order to make it accepted by more and more general users, the new AO method should be simple, efficient, reliable and robust [220].

3.2 Wavefront Sensor Based AO System

The basic structure of AO system in the telescope is shown in Figure 3-4 a) [221], in which light the telescope is relayed to an AOE, usually a DM due to its speed and efficiency. The wavefront of the light is detected by inserting a beam splitter, to partially send some of the light to a wavefront sensor (e.g. SHWS), before being collected by the imaging sensor (e.g. camera). And the detected wavefront information will be used to control the shape of the AOE through

a feedback loop, with pre-calibrated coefficients of Zernike polynomial. Here the wavefront is the wavefront at the pupil plane, and the light from the star can be seen as from infinity, so ideally the light should have flat wavefront. As we know, the lens will transform the flat wavefront into parabolic wavefront for converging the beam into focus. Thus any deviation breaks the flatness will degrade the focus performance. So AO will keep the wavefront to be flat before collected by the imaging sensor.

It is relatively simple to start AO microscope from building an AO telescope first. There are few benefits of doing this. First, this step is a learning process that decoupled the sophisticated laser scanning AO to basic modules. Second, this setup can be used to calibrate the devices and estimate performance and reliability. Then after the building and testing of telescope AO, in next step, this setup will be transplanted and integrated into the existing polygon laser scanning microscope.

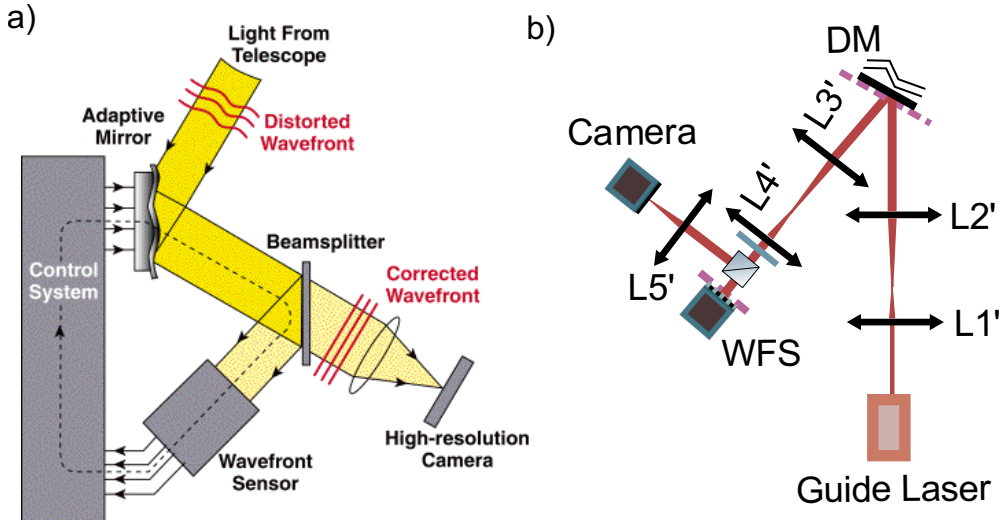

Figure 3-4 Schematic of AO setup. a) A scheme for telescope application. Adapted from [222] with permission. b) Syestem of self-built AO testing setup.

The AO testing setup is shown in Figure 3-4 b), in which a 660 nm wavelength guide laser (OBIS, Coherent Company, US) has been used as the light source. The 1 mm ($1/e^2$) width laser beam was first extended to 10 mm by a telescope, which is built by a pair of doublets achromatic lens with 30 mm and 300 mm focus length lens (Thorlabs, US) respectively. The extended beam incident on a piezoelectric DM (DMP40, Thorlabs, US) with an oblique angle

for reflection. This tilted allocation of DM decreased the loss of power during the transmission, comparing vertical angle reflection alignment, which requires addition beam splitter and waveplate. After the DM, the light beam will be relayed and contracted to 3.3 mm width by a 4f system, 300 mm and 100 mm focus length for L3' and L4' (Thorlabs, US) respectively. The relayed light will pass through a 0.1 optical density neutral density (ND) filter (Thorlabs, US) and a 50:50 beam splitter (Thorlabs, US). One branch of the beam is focused by a 50 mm lens L5' (Thorlabs, US) to a CMOS camera (DCC1645C, Thorlabs, US) for imaging the laser beam, while the other branch goes to an SHWS (WFS150-5C, Thorlabs, US). The microlens array plane of SHWS is conjugated to the DM mirror plane so that the detected wavefront is the wavefront at the pupil plane of the DM. Through this design, the laser beam fills both the pupil of DM and SHWS, so the measured aberration from the wavefront sensor and the correction of the adaptive mirror are matched. The using of the ND filter would avoid the overexposure of imaging instruments in the experiment, for protecting the imaging instruments and keep the measurement accuracy. This optical layout mimics an AO telescope on the bench and will be used to quantitively characterize the mirrors working range and testify the AO performance.

The schematic drawing of the DM we used is shown in Figure 3-5 a) [223]. It has a continuous reflective surface with 40 segmented electrodes at the backside of the glass substrate with a glued piezoelectric disk. The 40 rear electrodes control 40 independent mirror segments by the value of the control voltage. The control voltage range is from 0 to 200 V, and 100 V is the reference point with the flat mirror surface. If applied a voltage less or more than 100 V, the piezoelectric area of the corresponding electrode will expand or shrink, thus leading to a local concave or convex bending. This feature will be used to compensate the aberrated wavefront by independently changing the voltages of the electrodes. The pupil plane is 10 mm, therefore to make usage of the whole range of the mirror, the beam width should be 10 mm that fulfil the pupil of the DM. This consideration of pupil geometrical size is critical in the AO system design, because the boundary of the pupil is corresponding to the high-frequency component of the light, and the image quality in the microscope is sensitive to the high-frequency component of light. So, the rule of thumb in AO microscope designing is choosing

the lens with the right focal length for fulfilling the pupil of the DM and passing through the optical train without blocking of the beam boundary after the DM.

This DM supports the first 15th Zernike modes, and Thorlabs has provided a pre-calibrated unified tuning range of each of them (-1 to +1). The calibrated stroke ranges of the supported Zernike modes are varied with different Zernike modes, from the minimum $\pm 1\ \mu m$ (maximum peak to valley, PV) at the third-order spherical aberration to the $\pm 6.8\ \mu m$ of astigmatism. The tuning range is decreasing with the increasing of Zernike modes. The SHWS used here is a combination of microlens array with 150 µm pitch size and a CMOS camera, already calibrated at the Thorlabs factory. The SHWS provides application software to operate the measurements with multiple imaging panels to display the results, which include beam intensity panel, wavefront panel and Zernike modes panel.

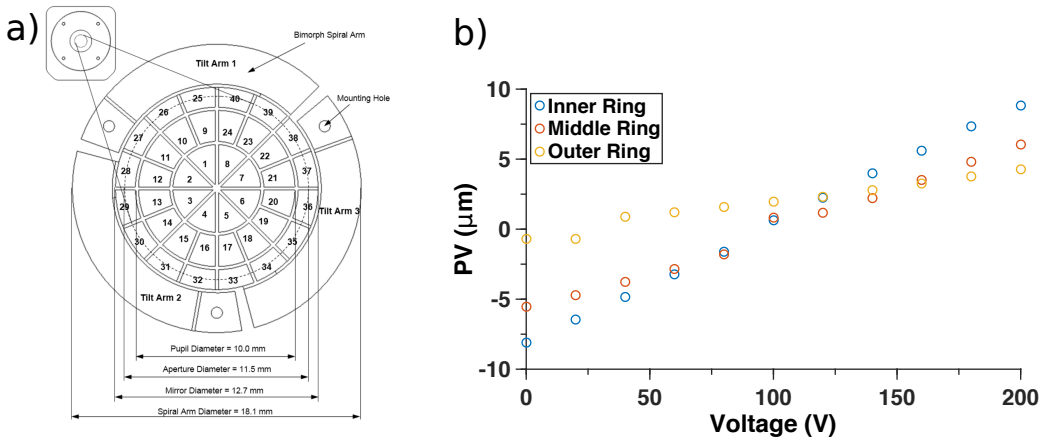

Figure 3-5 The calibration results of DM. a) The layout of DM segments and geometry [223]. b) The plot of segments stroke value (PV) over the different supply voltage, with a step value of 20 V.

SHWS will display a few wavefront statistical data, e.g. PV, RMS, radius of curvature (RoS) in units of µm or wavelength. Here we chose PV as the parameter to characterize the DM instrument. The measurement results are shown in Figure 3-5 b). The segments of the DM has been grouped as three annular bands, as inner ring, middle ring and out ring in the figure legend. The results are obtained from applying different voltages of the corresponding segments from 0 to 200 V. The measured PV shows good linearity between the input voltage and output stroke with a range about ±8 µm for the inner ring mirror segments, ±5.5 µm for

the middle ring segments and ±1.2 μm for the outer ring segments. The results showed the PV range is different for different segments even with the same control voltage, which means if applied the same voltage to all the four segments, instead of getting a flat wavefront, it will lead to a spherical wavefront. However, the GUI of the DM software only displays the applied voltage to the mirror, not the PV value, so this characterization helps to evaluate the real effect of the DM when applied voltages onto it.

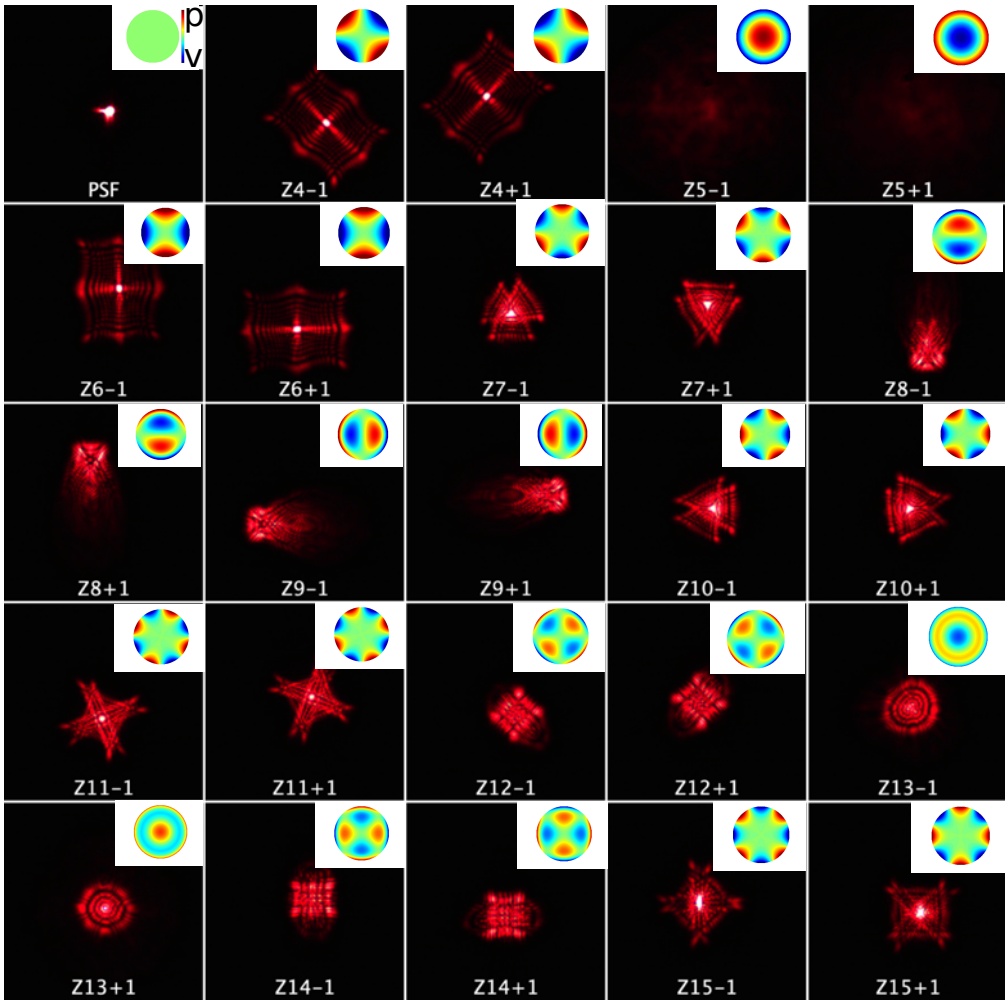

Figure 3-6 The available PSF images of the first 15th Zernike modes (except the piston) from the testing setup. The initial PSF without any aberration is on the top left, then PSF with different Zernike modes of the maximum and minimum coefficients (±1) are shown in sequence. The label Z at the bottom means Zernike, followed by the number indicating the mode and signed integer

indicating the coefficient. The inset plot on the corner in each PSF is the corresponding Zernike phase pattern.

The measured PSFs with the first 15th Zernike aberration generated by the DM are shown in Figure 3-6, from the reference PSF with a flat DM surface, to different Zernike modes with normalized coefficient at both ends of -1 and +1. In Figure 3-6, Z4 and Z6 are corresponding to oblique and vertical astigmatism aberrations, Z5 is the defocus aberration, Z7 and Z10 represent vertical trefoil and horizontal trefoil aberrations, Z8 and Z9 denote the vertical and horizontal coma aberrations, Z11 and Z15 are the pair of tetrafoil aberrations, Z12 and Z14 are the secondary astigmatism aberrations, and Z13 is the third-order spherical aberration. These results demonstrate the ability to use DM to create the corresponding PSF with programmed Zernike coefficients, which will be used in the following AO correction.

Currently, the hardware part of AO has been finished, but to constitute an AO system, a control loop need to be established between the DM and SHWS. However, commercial AO control loop software (DataSocket, Thorlabs, US [223]) is provided by the manufacturer . With the help of this software, the orientation of the beam along the DM to the SHWS and the maximum achievable stroke of each Zernike coefficient will also be calibrated automatically before AO correction starts. Now the AO system is finally ready to use, in order to testify its ability of correction, a coverslip was inserted into the beam path, so part of the light passed through the coverslip, and the other part did not. The distorted laser beam result is shown in

Figure 3-7 a), in which the focus spot has been broken into two discontinues parts due to its wavefront has been interrupted by the coverslip. After 0.4 seconds (2.5 Hz correction bandwidth) in the automatic AO correction loop, the beam was recovered back to a regular point, as shown in Figure 3-7 b), and the phase mask on the DM was plotted in the inset, which also has a corresponding wavefront shape to the distortion of beam. The intensity profile of the focus has been drawn in Figure 3-7 c). The residual aberration is mostly from the measurement accuracy of the wavefront sensor and path difference between the image camera and SHWS.

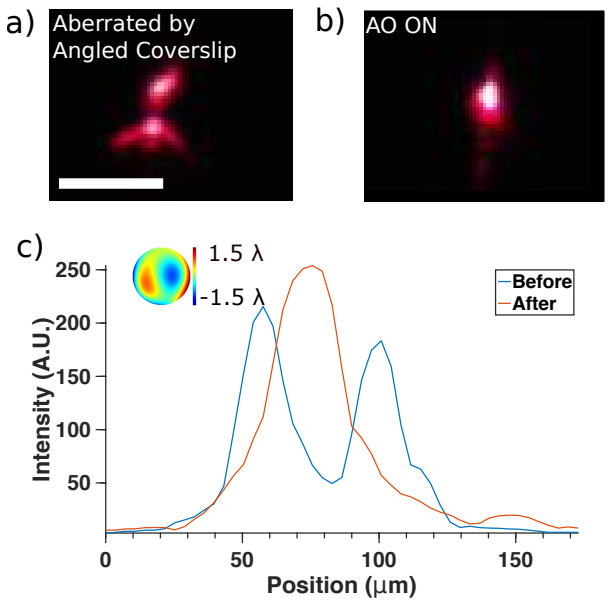

Figure 3-7 The AO correction results. a) The PSF before AO. b) After AO correction. c) Intensity profile of the cross diameter line. Scale bar, 50 μm.

Now, the building process of AO correction system, calibration of DM and testification of close-loop performance measurement results are demonstrated. This results proved that this AO system can correct and compensate the insensitive random distortions that the light might encounter during the propagation. So next is integrating this AO system into the polygon laser scanning multiphoton microscope. However, there are a few limitations that need to be concerned before adding AO to the microscope. First, the allocation of SHWS in a multiphoton microscope is not straight forward, if use it measures the wavefront of fluorescence wavefront it will inevitably cost the photon budget and hard to work with weak fluorescence sample. Second, the positioning of DM can be either at different planes, such as image plane and pupil plane; each of them has their advantages and disadvantages [173]. The guidelines are that the location of DM should have high accuracy and efficiency in terms of correction and match its device parameters. With consideration of all these factors, in our AO polygon microscope, the DM was allocated to the pupil conjugate plane before the polygon mirror. Due to the geometry constraints and working limitations in microscope area, here in our setup, SHWS was used for inspection of DM performance rather than sample aberration measurement. It was allocated

between the tube lens and objective lens, for achieving the ability to monitor the whole optical train.

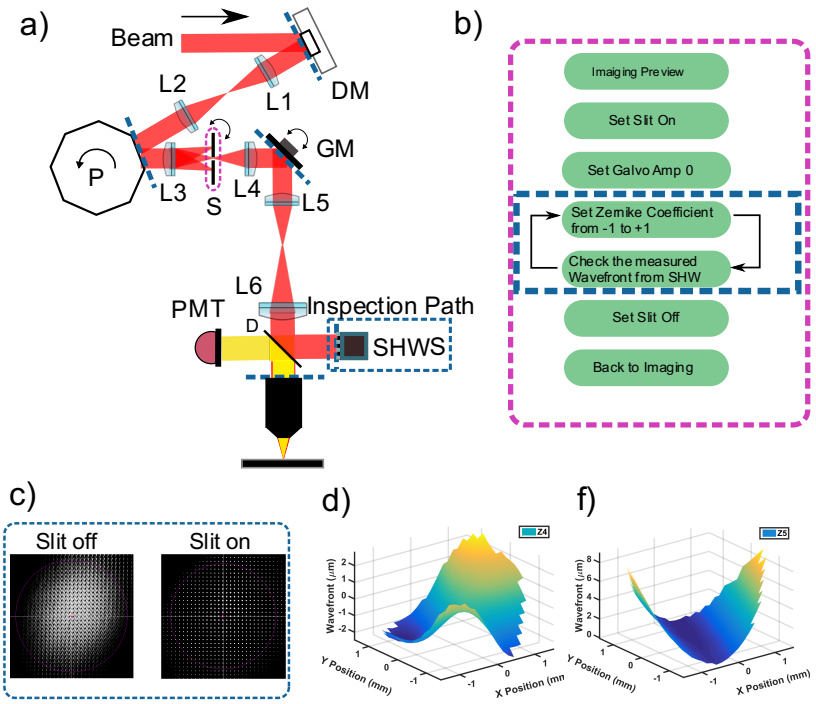

Figure 3-8 The integration of AO with a polygon laser scanning microscope. a) The simplified layout of AO polygon multiphoton microscope. L denotes apochromatic lens, DM denotes deformable mirror, P denotes polygon scanner, G denotes galvanometer mirror, S denotes flip-flopper slit with 200 μm width. D means diachronic mirror. SHWS means Shack-Hartmann wavefront sensor. b) The flowchart of using slit to calibrate the DM without stopping the polygon mirror. c) The spot measurement results of SHWS through switching the slit on and off without stopping the polygon. d) Measured astigmatism range from SHWS with normalized Zernike amplitude from -1 to +1 by adjusting the DM. f) Measured defocus range in the same way as d).

Given this, the final schematic diagram of our AO polygon microscope setup is shown in Figure 3-8 a). DM was put before the scanning devices so that the beam at the DM would be static, and the applied DM correction mask would also have a relatively stable modulation for the phase of the laser beam. Second, the DM was conjugated to the pupil plane, pupil plane AO has high correction accuracy but localised practical FOV (isoplanatic patch) comparing to the image plane AO. Time multiplexing technique will be deployed to solve the working FOV problem, which will be explained in detail in the following RAO subchapter. Lastly, as a

monitoring device to inspect the DM alignment, SHWS was put after the dichroic mirror, this allocation not only saved the photon budget by using the scattered reflected photons, but also could inspect the whole system. The procedure of alignment the DM will be discussed after the illustration of the setup.

The technical details of this set up is, DM (Thorlabs, NJ, USA: DMP40, 10 mm x 10 mm) was conjugated to both a 36-facets polygon mirror (PM) (Lincoln Laser, MA, USA: DT-36-250-025, 4.8 mm × 5.0 mm) and virtual conjugated galvanometer mirror (GM) pairs (Cambridge Technology, MA, USA: 6220H, 7 mm × 5 mm), which all were conjugated to the back focal plane of a low magnification objective (Zeiss, Germany: 20×, 1.00 NA/water). The Ti-Sapphire two-photon illuminating pulsed laser (Spectra Physics: Tsunami, CA, USA) pumped by a 5 W diode-pumped solid-state laser (Spectra Physics: Millennia, CA, USA), was first expanded to a $1/e^2$ diameter of 10 mm by a telescope (f 50 mm and f 300 mm length) before incidents onto the DM which has an aperture of 10 mm as well. In this way, all the segments of DM could play a role in modulating the laser wavefront. Then the laser was contracted by a 4f system to a diameter of 2.67 mm to the PM. The PM was imaged to GM by a 4f system (f 30 mm and f 60 mm). The GM was then imaged into the back focal plane of the objective by another 4f system (f 100 mm, f 200 mm). Before getting into the objective, the laser beam went through a dichroic long-pass filter (D) (Semrock, NJ, USA: FF665-Di02) first. This filter was not only used to separate the emitted fluorescence signal but also reflected part of the laser beam to an SHWS (Thorlabs, NJ, USA: WFS30-5C) as an inspecting camera for alignment. The emitted fluorescence is collected by the same objective, reflected by the dichroic mirror and then detected by PMT (Hamamatsu, Japan: R3896 or H7422-40) with corresponding spectral filter for desired fluorescence.

The alignment procedure of this system is shown in Figure 3-8 b). This schematic of using SHWS as an inspecting camera is due to the fine alignment requirement of the DM. DM is not a simple flat mirror which can be aligned by two pinholes directing to the targeted path, it is a group of tiny segmented mirrors which will keep changing the surface shape for AO correction , and this process will inevitably skew the beam angle and degrade the alignment from its flat shape state especially in scanning situation with other devices. Therefore, adjustment of DM

should keep the beam spot staying at the same position during the whole range of stroke. Therefore a WFS conjugated to the DM and close to the objective gives us the ability to monitor the entire system alignment, especially for the DM. A motorized filter flip (Thorlabs, NJ, USA: MFF101) with a 200 μm width slit (S) was put at the focus plane. Setting 0 to GM amplitude and putting slit on will only leave the centre beam come through the system which makes the wavefront is clear enough for WFS to monitor. The spot image of SHWS before and after slit is shown in Figure 3-8 c). The wavefront range of Zernike Z4 (astigmatism) and Z5 (defocus) from the normalized coefficients of -1 to +1 are measured and shown in Figure 3-8 d) and f) respectively, their peak to valley (PV) values are around 8 μm, corresponding to 10-wavelength in 800 nm wavelength light. The using of all reflective scanning devices in our design provides two advantages. The first is it maintains the imaging performance by minimum group dispersion comparing to diffractive scanning devices; second is the linearity of reflective tandem scanning enabled the high accuracy segments scanning for the RAO.

Now the hardware design of AO polygon microscope has been discussed. But to enable AO correction, the wavefront information is still missing in this setup. In the next subchapter, the method of indirect wavefront sensing for retrieving the aberration without guide stars will be demonstrated, in which the image metric will be used as the source to reconstruct the Zernike coefficients vector for AO correction. And the testing results of image metric based wavefront sensing in this polygon AO multiphoton microscope will be shown.

3.3 Image Metric Based Wavefront Sensing

There are few limitations of using SHWS as the wavefront sensor, first SHWS works for the pointed light source, and it cannot distinguish the detected wavefront from different focus planes. Second, the measurement performance is sensitive to the light's coherence and background noise, if the light signal is weak, then SHWS cannot obtain the wavefront information. Lastly, its measurement accuracy is limited by the fabrication precision of microlens array, which means it has a fixed wavefront measurement resolution, thus lacking flexibility. As we all know, in microscope application area, especially in the live tissue imaging

field, the biological sample is highly scattering with very complex and unregular inhomogeneous structure, so usually in most of the cases there is natural guide star in the imaging, and also even if there is a guide star in the biological sample by external stimulation or beads injection [190, 191], the light will be scattered a lot during the propagation route. Thus the measured wavefront is contaminated by the unwanted photons from different layers, which will affect the measurement precision. And also, the using of SHWS will add the cost and increase the complexity of the system, which usually requiring extra high accuracy alignment and calibration.

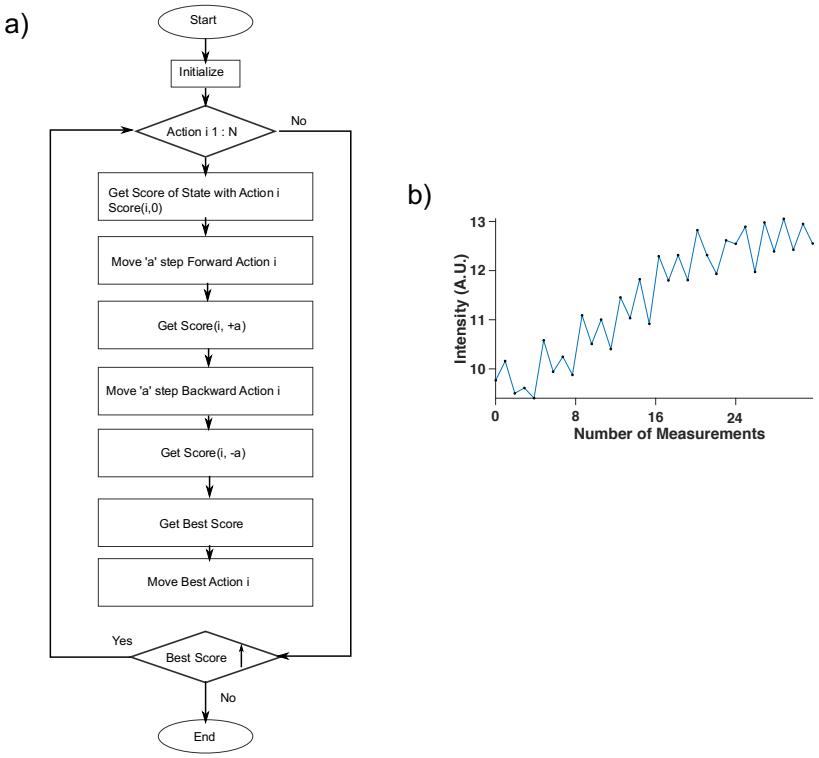

Figure 3-9 Image metric based wavefront sensing progress. a) The flow chart of sensorless wavefront sensing program. b) The intensity plot during the iteration process of sensorless aberration measurement.

To solve the above problem, image metric based wavefront sensing for AO correction had put forward [195]. The necessary process is using image metric as a function of the Zernike coefficients, so with positive and negative Zernike bias, the polarity and amount of metric change will indicate the optimal value of Zernike modes for getting the extremum image

performance. Since the phase information has lost with a single intensity image, novel information must be introduced to recover the wavefront information. The novel information is the artificially induced biased Zernike modes, usually through manipulation the adaptive mirror. The aberration in microscopy is dominated only by the first few Zernike modes [224], which decreased the number of measurements to a reasonable level. For multiphoton microscope, signal intensity is a good and straightforward metric works well in most of the biology samples [196], this is because the intensity of emitted fluorescence in multiphoton absorption process is highly confined to the focus area in quadratic relation, the less the aberration, the higher the concentration of power, and the more the fluorophores signal will emit. The image signal intensity will be used as the metric for wavefront correction in our polygon AO microscope.

The indirect wavefront sensing process applied in the our polygon microscope is shown in

Figure 3-9 a), it is a sequence loop with the loop number named “Action”, which equals to the number of Zernike modes expected for correction. The DM we used only supports the first 15 Zernike modes, so the action number of the loop is 12 after getting rid of the first three piston Zernike modes. “Score” denotes the metric of an image, here in the multiphoton microscope, we set it as the averaged intensity of the selected FOV. The step value ‘a’ is a bias added to the Zernike coefficient ranging from -1 to +1, which can be tuned to control the conversion speed and accuracy. Currently, the current default step value is 0.05 for all the Zernike modes. The step value will be added to both directions initially, and the direction of increasing metric will be chosen, and then a hill climb algorithm is applied, the process will stop until it reaches the best score (maximum value of metric). The result of this iteration loop is shown in

Figure 3-9 b). In which, the metric score reaches the plateau after 24 times of measurements, which is a representative measurement process in indirect wavefront sensing.

A 3 μm bead, aberrated by the immersion medium, is used to test the AO correction performance, and the experiment results are demonstrated in Figure 3-10. The nearby area of single bead was chosen as the interested FOV, after the AO iteration correction based on the

metric of averaged intensity, the aberrated image is refocused to an integrated bead. The bead before and after AO correction are shown in Figure 3-10 a) and b) respectively. The intensity profile of the yellow dashed line area is plotted in Figure 3-10 c), and measured aberration phase pattern is shown in the inset.

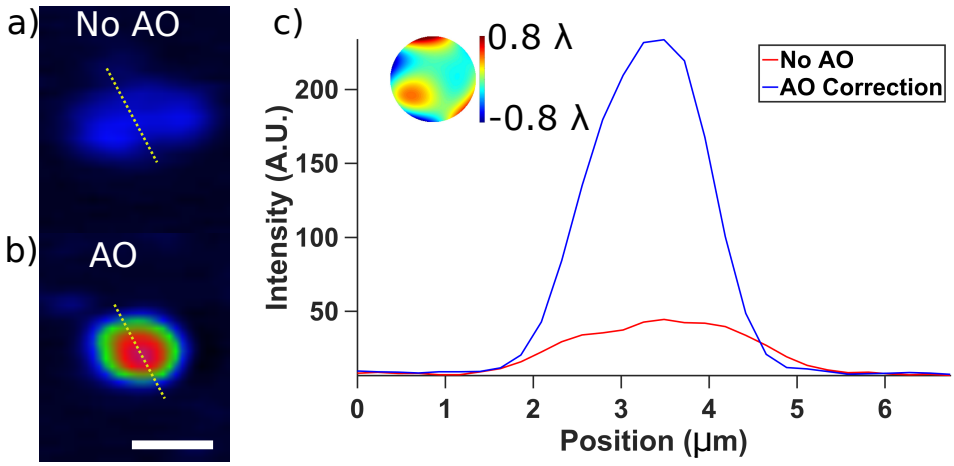

Figure 3-10 The testing result of 3 μm bead-based image metric AO correction in the polygon multiphoton microscope. a) Aberrated bead before AO. b) Bead after the AO correction. c) Intensity profile of the dashed yellow line in a) and b) for quantitative comparison. Inset is the correction phase pattern obtained from this image metric-based measurement process. Scale bar, 5 μm.

Besides, this indirect wavefront sensing AO correction method was applied to pollen grains. The results are shown in Figure 3-11. The FOV area for metric measurement is chosen as the boundary of the pollen. The results of AO and deconvolution after AO are shown in Figure 3-11 b) and c) respectively. After deconvolution process, image sharpness was further improved to a certain level, with a resolved internal structure of the pollen. Deconvolution is a method of compensation the diffraction effect, by redistributing the diffracted photons back to the centre of focus based on the PSF information[225]. Therefore, the better the image closes the diffraction limit, the more the enhancement of deconvolution can be. Given this, images after AO correction provide an ideal application scenario for deconvolution processing.

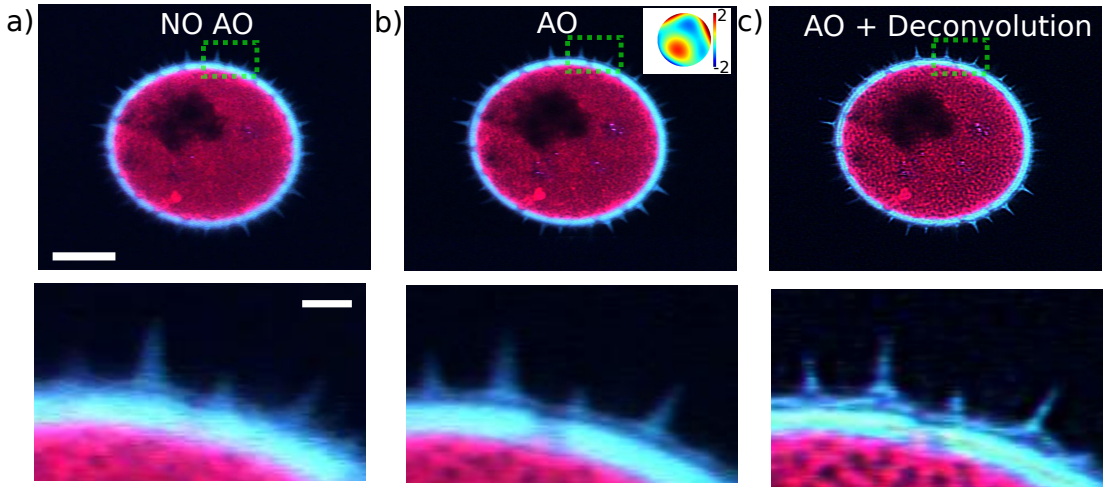

Figure 3-11 AO results of the pollen grain. a) Single pollen image before AO. b) After AO correction. Inset is the phase pattern for correction, at the unit of wavelength. c) Image of AO plus deconvolution, obtained with blind deconvolution process of b). Scale bar, 10 μm, 1 μm.

Until now, we have shown the availability of AO correction with image metric based indirect wavefront sensing. However, there are still several limitations inherited in this method. First, this image metric based wavefront sensing performance is FOV dependent, which is why the results showed are single bead and pollen in a small area rather than the full FOV. And this FOV dependent effect also degrades the repeatability and reliability of AO correction cause metric field needs to be explicitly chosen. Second, it requires a stack of measurements for wavefront retrieving, which increases the risk of photo damaging and slows the wavefront correction speed. Lastly, because the sample is highly inhomogeneous, even if the retrieved wavefront is good enough, the correction phase mask added on the beam would still be deteriorated with different scanning angles and different FOV, which will degenerate the AO performance. To solve these problems, I put forward the time-multiplexed RAO for achieving correction over different isoplanatic patches. Also, this method will also be used to extend the system FOV by compensating the curvature distortion over the limitations of lens diameter.

3.4 Raster Adaptive Optics (RAO)

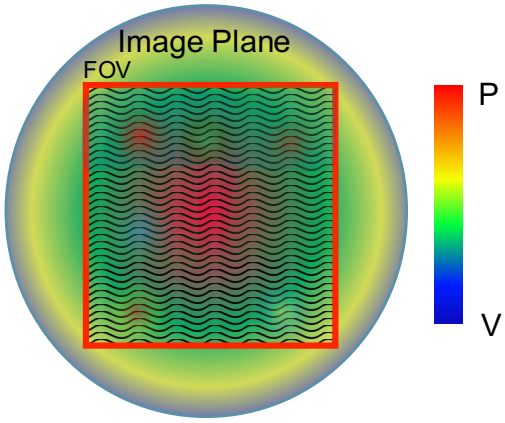

Figure 3-12 Illustration plot of the field dependant aberration over the image plane, in which the colour code denotes the wavefront.

The illustration of field dependant aberration, also known as the non-uniform spatially varying aberration, is shown in Figure 3-12, in which the aberration's phase pattern are demonstrated as modifying over the FOV. The sphere area is the objective lens' of vision of the field, and the boundary has a strong sphere aberration that limits the FOV. And inside the red square is where the efficient FOV can be obtained by the microscope, in which the wavy line denotes the ideal correlated uniform wavefront, and the colourful gradient presents the changing of wavefront structure in practice, which will break the correlation and produces the isoplanatic patches. All these aberrations are varying over the image plane, which will have different wavefront at the pupil plane (by Fourier transform). So for the pupil plane AO, a single pattern cannot compensate all these aberrations. Image conjugate AO is possible but limits one aberration layer only which restricts its full applications.

However, in laser scanning microscope, the sample is being illuminated in sequence, so the time interval among different areas of image during the scanning provides the possibility of correcting the field-dependent aberration in corresponding scanning time. In an ideal situation, each image pixel should be corrected, and the trial of using a lookup table to fix every single pixel had been done[193]. However, in video-rate laser scanning microscopes, pixel-based correction would require an AOE with 50 ns response time, while most available devices'

response time is from ms to μs [193]. Second, the correction efficiency is low if using single-pixel signal, which would be easily affected by the stochastic background signals and quantum noises. Lastly, the isoplanatic patch, determined by the phase structure [173], is different in different samples, so it is not necessary to correct each pixel with a different wavefront pattern.

Given this, correction of segments rather than the pixel is put forward, which is called RAO. The proposed idea is shown in Figure 3-13, in which the image is segmented the in rectangular areas by dividing through the slow axis of the scanning geometry. This segments will have ms duration, so to provide enough update time for off-the-shelf DMs. And for each segment, image metric based wavefront sensing will be applied to retrieve the Zernike vectors for compensation. The measured Zernike vectors will be sent to the pupil conjugated DM in sequent, and be in synchronizing with the scanning devices as well. Through this, not only the field-dependent aberration can be corrected, but also the correction bandwidth is maintained. In raster scanning, the frame rate is inversely proportional to the scanning area. So even if segments correction requires measurements of aberration pattern for each segment, the total exposure time is still the same. Therefore it will not cause extra photodamage.

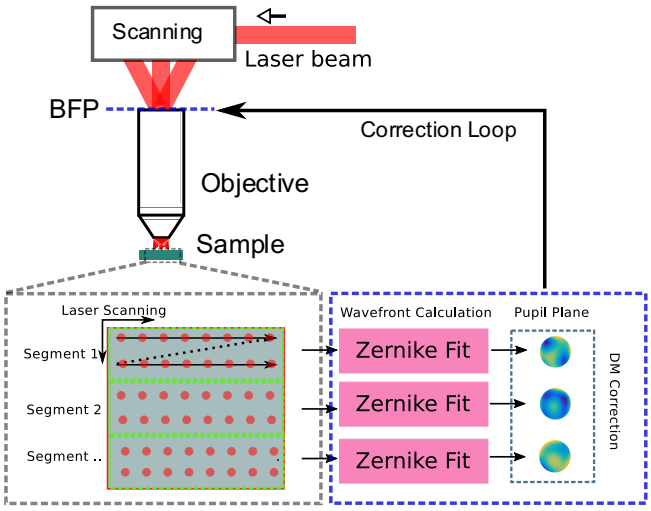

Figure 3-13 Schematic diagram of RAO, in which the image plane is tandem scanned towards fast and slow axes. Aberration wavefront of each segment will be retrieved based on the image metric

indirect sensing method, and the wavefront information will be sent to DM in sequence for correction. DM is conjugated to the BFP of the objective.

The optical layout of the RAO in polygon microscope is drawn in Figure 3-14 a). In which, DM, polygon mirror and a pair of GMs are all conjugated to the pupil plane. The essential part in RAO is the synchronization of DM pattern with tandem laser scanning to get the pseudo "simultaneous" correction with a single deformable mirror in one single frame, through segmented image plane correction in the vertical direction. The control signal sequence is shown in b), in which the DM is synchronized with VSYNC signal, and for 20 Hz VSYNC duration, the maximum DM update rate will 10 times faster at 200 Hz, this is due to the response time limit of our DM can get is 2 ms, as shown in Figure 3-14 c). Therefore, the maximum time-multiplexing correction is 10 segments at 20 Hz imaging rate.

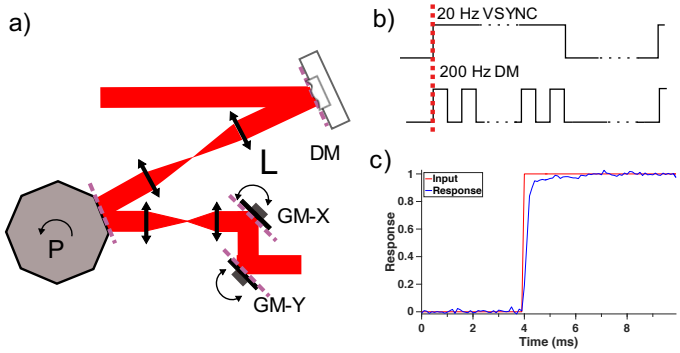

Figure 3-14 Practical realization of RAO. a) Schematic diagram of the RAO polygon microscope. b) The timing diagram and synchronization signal sequence in case of 10 segments correction at 20 FPS. The red dash line indicates the synchronization starting point. c) Normalized step response of the DM. The rise time of 10% to 90% is 313 μs, the overshoot is less than 6.3%.

This AO/RAO function has been integrated into the PScan GUI for easy access. The updated GUI with AO function has been shown in Figure 3-15, in which two more image channels has been added on the right side, providing results display after and before AO correction. The AO control panel is located under the AO imaging channels. Currently, there are buttons of AO SBPHScan, AO On/Off, AO Hscan, System on/Off and WFS, under these buttons is the command window, which used for choosing the number of segments. For the AO function buttons, AO SBPHScan is reserved for the future high SBP AO correction to combine

the high SBP image with AO correction. AO On/Off button is used to switch the AO correction state with the measured aberration masks through pressing the AOHscan button. System on/Off is the button for switching system aberration correction on and off. WFS button is reserved for future fast aberration measurement, e.g. transport equation based fast wavefront sensing [226].

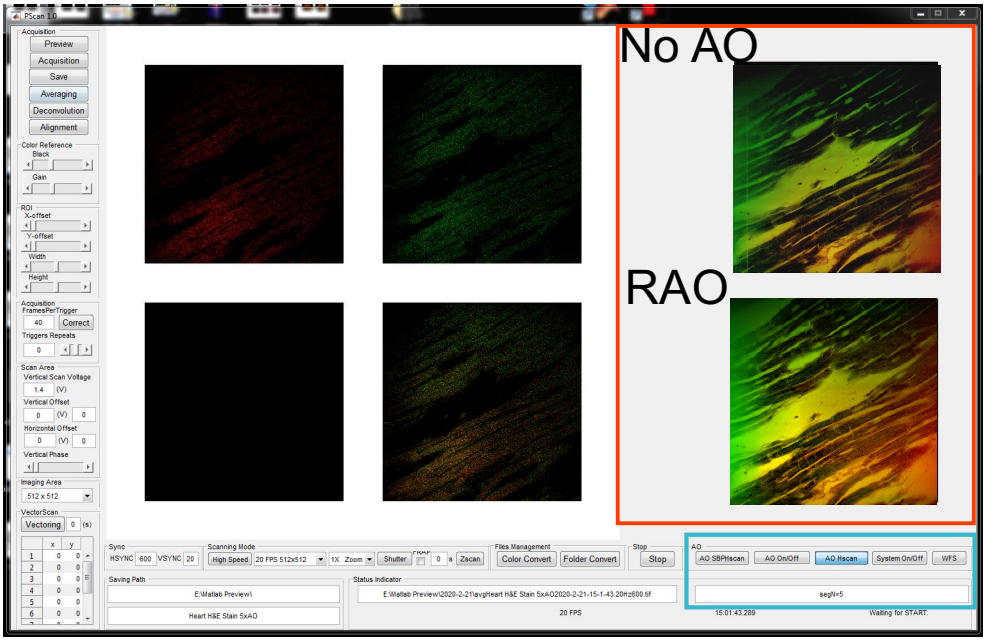

Figure 3-15 PScan GUI with RAO function, in which the control button and commend dialogue window are shown in the blue square. In the red square are the two channels of the average image before and after AO correction. The sample used here is mice heart tissue slide.

The test results of improving in correction over the number of segments are shown in Figure 3-16 by using a rhodamine stained mice kidney slide. The kidney is a type of sample with high inhomogeneous index, thus is a suitable specimen for the AO performance test. The wavefront measurement time is 22 seconds for one segment, so from 1 to 2, 5 and 10 segments RAO, the corresponding measuring time are 22, 44, 110 and 220 seconds respectively. The result demonstrated with image brightness, and contrast are proportional to the number of segments. To see the detail, zoomed images of the area from top to bottom are shown in Figure 3-16 b), c), d) and e). The quantified results of image intensity plot are shown in f), which has a 2.65 times improvement overall area, this figure proves the effectiveness of RAO comparing to the traditional method. All the images are 2 s averaged image from a 20 FPS video.

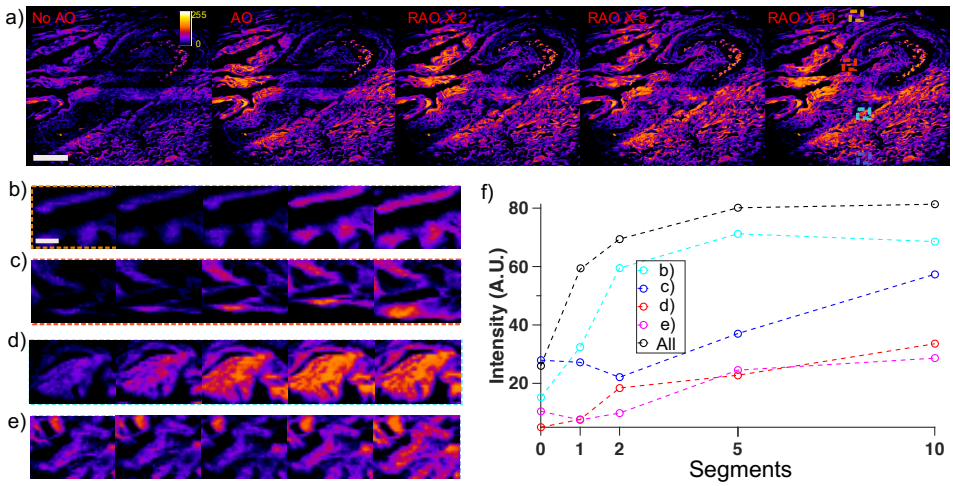

Figure 3-16 a) Image results of rhodamine stained mouse kidney sample slide. From left to right is before AO, one segment AO, 2 segments RAO, 5 segments RAO and 10 segments RAO. Image is segmented in the vertical direction for correction as in Fig. 4. Scale bar 50 μm. b) Zoomed-in image of the magenta ROI in the top region of a), from no AO to 10 segments RAO. Scale bar 5 μm. c) Zoomed-in image of the red ROI in the middle up area. d) Zoomed-in image of cyan ROI in the middle down area. e) Zoomed0in image of the blue ROI in the bottom. f) Area intensity plots of the 4 regions chosen in b) c) d) and e) as well as the whole image area in a), 2.65 times improvement over the entire area and 2 to 3 times increase over all the chosen region can be derived from the plot.

Characterising experiment was conducted on 210 nm beads samples. The imaging result is shown in Figure 3-17 a). It is 10 segments correction RAO, The normalized reconstructed wavefront of each segment in RAO and the normal AO with the entire area as metric area are shown in b). The PV value of RAO is about 3 times bigger than the normal AO, which means RAO can achieve higher wavefront estimation accuracy. Zooming images of interest areas are shown in c), which are quantified by the line plot through the centre of the chosen beads in d). The signal intensity has increased 2 times by RAO over the different areas.

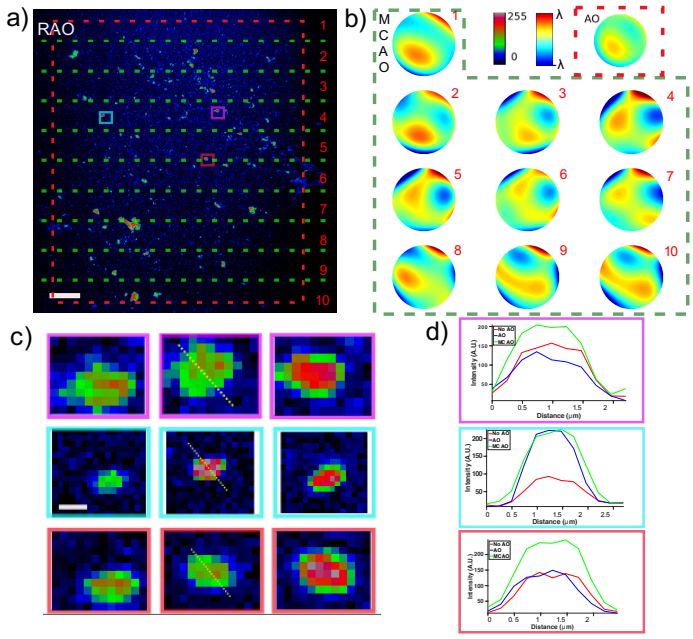

Figure 3-17 a) 2s averaged image of 210 nm beads at 20 FPS without 10 segments RAO correction. Scale bar is 25 μm. Red dashed square denotes the area of image metric for normal AO. Green dashed line indicates the segment area for RAO. b) The normalized DM pattern of corresponding single AO and RAO in a). c) Zoomed-in image of the choosing area. Scale bar is 1 μm. d) Intensity profile plot of the yellow dashed line area in c).

To further testify the RAO performance, 3 μm yellow-green fluorescent microspheres (Polyscience, Inc) with artificially induced heterogeneity refractive index medium have been used. With purposely introduced layers of mismatched glycerol, glass and cured transparent silicone – polydimethylsiloxane, PDMS to make the sample, and the experiment structure is shown in Figure 3-18 a). The total imaging depth is up to 1.1 mm, 3 μm diameter Fluoresbrite yellow-green microspheres embedded in a silicone polymer block, the fluorescence signals' intensity and FWHM before and after RAO are used for quantification measurement of the degree of aberration correction. Four representative depths of 25 μm, 500 μm, 900 μm and 1000 are shown in Figure 3-18 b). The corresponding intensity line plot is shown in c). Our results demonstrated that RAO could afford up to 1.36 fold and 1.74 fold improvement in FWHM and signal intensity respectively over a certain imaging depth of 1 mm.

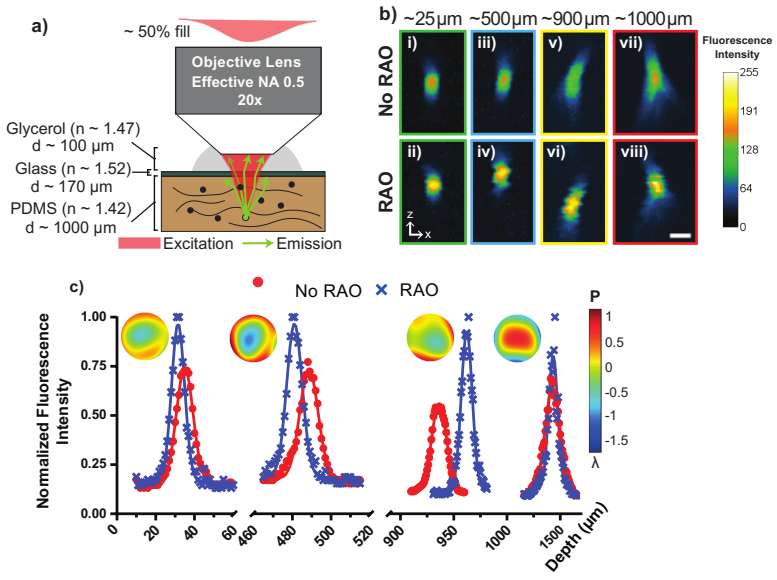

Figure 3-18 Imaging results of inhomogeneity 3 μm yellow-green beads. a) Diagram of the experiment setup. b) Axial image of beads without and without RAO at different depths. Imaging speed is 20 FPS, acquired by motorized stage moving in z-direction. c) Improvement comparisons line plot of images in b). The correction wavefront mask is shown at the corner.

Moreover, RAO can also be used to correct the aberration along the fast axis by stitching. The principle is shown in Figure 3-19 a), in which the subsegment in the horizontal direction (fast axis) is labelled by integer m, m equals the number of images needs to be stitched. In this case, only that subsegment area will be counted as the metric area for wavefront sensing, when stitching, only this area will be kept. RAO correction can correct isoplanatic patches with arbitrary shapes. The second application of RAO is extending FOV through a combination usage of GM and RAO. The principle is shown in Figure 3-19 b), in which FOV can be stitched by using GM to generate a shift in horizontal direction, and RAO will compensate the introduced field curvature, so the full FOV will be extended.

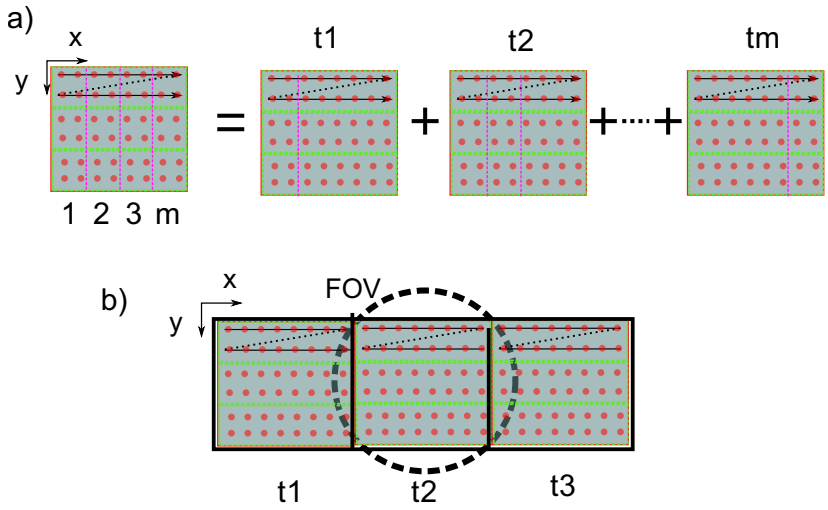

Figure 3-19 a) Fast axis segment correction in RAO through the stitching. b) Large FOV correction by RAO.

The results of a large FOV image with 5 x 10 correction segments are shown in Figure 3-20. The sample is fibroblast cells, from left to right are samples, with 5 segments RAO correction on each frame, and 5 x 10 segments RAO correction by GM stitching, a final image with 320 x 850 μm FOV is obtained. It shows the intensity at the horizontal boundary is much improved, with the nucleus of the cell being resolved [227]. The pixel size is 0.6 μm, and imaging speed is still 20 FPS, the wavefront update time is 10 ms, so stitching into a 50 wavefront musk image will take 500 ms. The image is obtained by control the x-direction GM, with a step value of 100 um, totally 10 frames are acquired. And each of these 10 frames has a 5 RAO correction masks. Each measurement area for RAO wavefront retrieving was digitally selected to an 80 um x 80 um area. After getting the 10 frames in sequence, ImageJ software was used to achieve digital stitching.

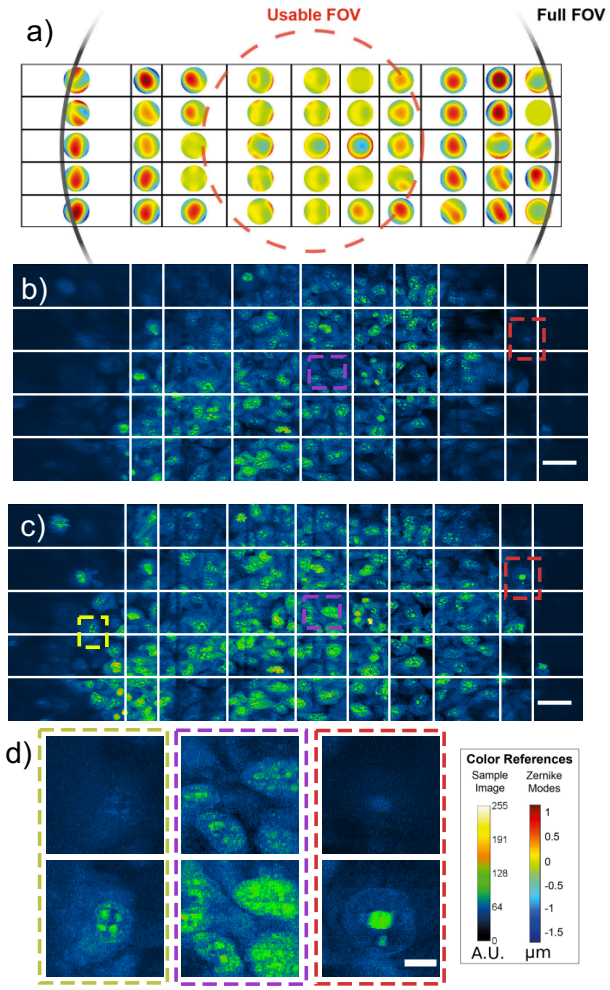

Figure 3-20 Results of flexible RAO with large FOV imaging. a) The correction phase mask of the RAO with 5 x 10 segments on horizontal and vertical directions. b) The image of fibroblast cells before RAO correction. Scale bar, 50 μm. c) Image after RAO correction. Scale bar, 50 μm. d) The zoomed-in picture of the selected area in b) and c) for comparisons. Scale bar 5 um.

In summary, by applying RAO to laser scanning polygon microscope, we achieved 10 segments AO correction system with high resolution and high speed. The current correction process is synchronized to VSYNC only, which increased the potential of introducing jittering effect due to the mismatch with polygon scanning in horizontal, and also the segments number is limited to 10 at 20 FPS. Lastly, it is working in open loop and the segments number is limited by the response time of DM. But all these can be solved by working in a real-time control system to synchronize to the HSYNC and extended to close loop correction, and a faster DM

can further increase the number of segments. Besides, the DM can also be used to do axis scanning, which can be envisioned that a volumetric RAO correction can be possible. The major limitation of RAO is the bandwidth of the DM, cause during the DM transition; the wavefront is not stable and will cause possible artefacts and imaging aliasing.

3.5 Contributions

Woei Ming Lee supervised the project. Qiongkai Xu assisted in developing the image metric based AO correction algorithm. Daniel Lim assited in preparing the inhomogeneity beads and fibroblast cells, conducting the RAO experiment of these samples, and processing the corresponding data.

Chapter 4 Volumetric Multiphoton Microscope with Photomanipulation

From the previous chapters, a polygon based multiphoton microscope with RAO correction has been introduced. It retains unprecedented flexibility and improved performance in temporal resolution, spatial resolution and phototoxicity control (laser dwelling time). However, our current design still has two limitations. First, it lacks the random scanning function for photomanipulation. Second, different from previous research which focuses on 2-dimensional scanning, real biological events are happening in 3-dimensional space. Hence rapid volumetric imaging ability is demanded. In this chapter, I shall first demonstrate the achievement of volumetric imaging functionality by both mechanical stage and DM scanning. Then, I shall introduce the design of integrating photomanipulation function into polygon microscope and present the *in vivo* laser ablation experiment results. Photomanipulation can be used for selective photobleaching (FRAP) and laser surgeries (ablation), which is crucial for quantitively measuring the kinetics of molecules and observing of biological reactions. Rapid volumetric imaging can obtain the comprehensive the interaction of cells and its microenvironments, such as how the function of a cell can be affected by the vessels, the immune system and the neuron system. In this chapter, all animal experiments were performed using procedures approved by the Australian National University Standing Committee for Ethical Research Using Animals (protocol 2015/46).

4.1 Volumetric Imaging

One of the significant advantages inherited in the multiphoton microscope is the optical sectioning ability, which provides a three-dimensional resolving capability that cannot be

achieved in traditional widefield microscopes. However, in order to generate the volumetric imaging and apply it to capture dynamic biological processes, high-speed volumetric scanning is required. There are several methods to achieve 3D scanning with axial sectioning ability, such as mechanical sweeping either by moving the sample through mechanical stage or moving the objective with z-axis motor [228]; using electrically tunable lens or tunable acoustic gradience devices (TAG) to scan along axial axis (~10 ms) via varying beam diverge [145, 229]; remote scanning for rapid focus shifting (~ms) in axial direction [130, 230-232]. Mechanical stage-controlled volume imaging is simple to implement but limited to the speed (~ seconds) and might introduce mechanical jittering which might affect the accuracy during *in vivo* imaging experiment. Lens-based volume imaging is fast, but it requires an additional cost on the imaging performance, and have smaller FOV together with degraded PSF.

Here in the polygon microscope system, I deployed two volumetric scanning strategies, which combined will constitute a volumetric scanning module with both high range and high speed as well as high axial resolution. This system retains the flexibilities of speed, scanning steps (frames per volume) and volume size. This flexibility provides versatility in conducting different bioimaging experiments. For example, in *in vitro* samples, the volumetric scanning range is more important than scanning speed, while in most *in vivo* studies, the volumetric scanning speed will become the primary factor. I will also show the results of using our scanning system.

The key in our design is the combination of a high accuracy mechanical stage and a high-speed deformable mirror (DM). The mechanical stage provides flexibility about the scanning range, while DM provides the flexibility of scanning speed. So, for different imaging samples with different imaging motivations, we can use different devices. Through the synchronization of the axial scanning device and the GM scanners, volume speed at 1 to 10 VPS, based on the steps of scanning, has been achieved.

4.1.1 Mechanical Stage

The mechanical scanning strategy we chose is based on a precision motorized stage, MP-285 from Sutter Instrument (US). This stage has a motorized 25 mm travel range in all 3 orthogonal axes, with close-loop techniques to eliminate drifts. It has a controllable submicron tuning resolution ranging from 0.2 μm in coarse to 40 nm in fine. The controller devices are ROE 200 and MPC 200, both from Sutter Instrument. They are connected to our workstation through a USB cable, to enable serial communication control. The control communication software that sends commends to do iteration scanning is written in LabVIEW software (National Instruments, US), for its simplicity and compatibility with our existing control program for the polygon microscope scanning.

Sutter Instrument provides external control solution by sending commends through a USB cable to the read panel of ROE 200 which is connected to the MPC 200 controller. It supports the control of position in a straight line at a specified speed, by command as:

'S' + sp + Xpos + Ypos + Zpos,

where 'S' is the ASCII character "S" (decimal value 83 (53 hexadecimal) stored in 1 byte, sp is the speed level stored in 1 byte and contains a value of 0 (00 hex.) to 15 (0F hex.). Xpos, Ypos, and Zpos each consist of 4 bytes are used to contain a 32-bit unsigned integer value representing the absolute position of the axis of which to move. The positional value is the number of micro steps, which has a relation to the micron unit as 1 micro step equals to 16 microns. The speed in the axial scanning we set to is at the lowest velocity for reducing the mechanical movement jittering noises. Moreover, the total time delay for one micron is 150 ms, thus for one second, the moving distance is about 6.66 μm.

The imaging results are shown in the following figures. First, we imaged the blood vessel area of the leg. The specimen we used is a C57BL6 wildtype mouse under anaesthetic by ketamine/xylazine solution. This time we chose the artery instead of capillaries as our interest area due to its property of high density of cells and flowing dynamics, which is a good benchmark for demonstrating our imaging performance. The labelling dye we used is FITC

dextran (US, Thermo Fisher), under the guidelines and regulations of Australian National University protocol A2016/46. The whole setup in the *in vivo* experiment is shown in Figure 4-1 a). The intended imaging area of the leg was first opened up with a scissor. Then the mouse was allocated to a customized 3D printed container with a concave design in corresponding to the shape and size of the mice leg. Next, a coverslip was put on the top of the leg, touching slightly but sealed with phosphate-buffered saline (PBS) to minimize the mismatching of refractive index. On top of the coverslip, a metal ring was attached with ointment, which will be used as it provides tension to constrain the droplet of water immersion between the objective and the coverslip for imaging. The ready to image status after preparation is shown in Figure 4-1 b).

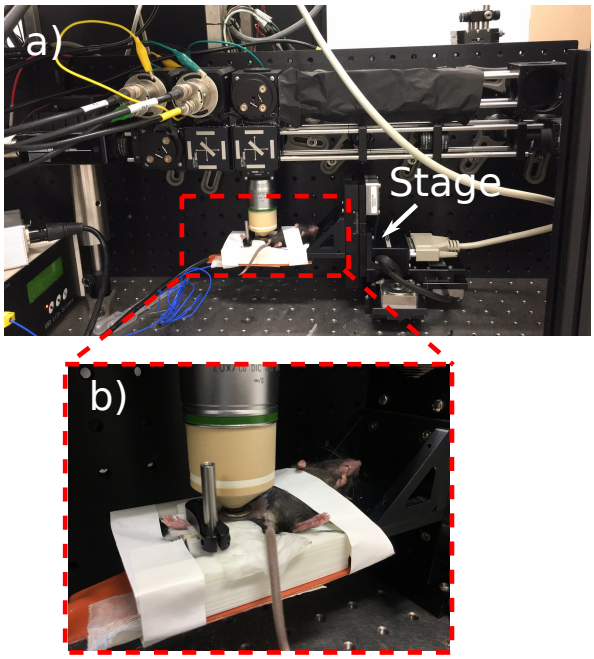

Figure 4-1 Photo of experiment setup and animal preparation. a) The final setup of polygon microscope, in the experiment progress, the mechanical stage had been shown in the figure. b) The zoomed image of mice under intravital vessel imaging, with customized 3D printing modules to hold the leg. A clamp was used to fix the leg for minimalizing the movement and sealing the immersion liquid.

The experiment results are shown in Figure 4-2. Scanned image with different depth of blood vessels are montaged into a single image. The blue fluorescence is second harmonic

generation (SHG) signals from the collagen fibre of the tissue, which provides a good indication of the focus distance onto the skin. Over the time of recording, imaging depth was increased, and we can see how the imaging goes through the tissue to reach the blood cells inside the artery. The round shape cell close to the wall of the vessel is mostly the white blood cells at slow speed. Here the contrast is provided purely by the dye circulation rather than other intrinsic labelling like engineered protein. The total imaging depth achieved for blood vessel tissue is about 110 μm in our system.

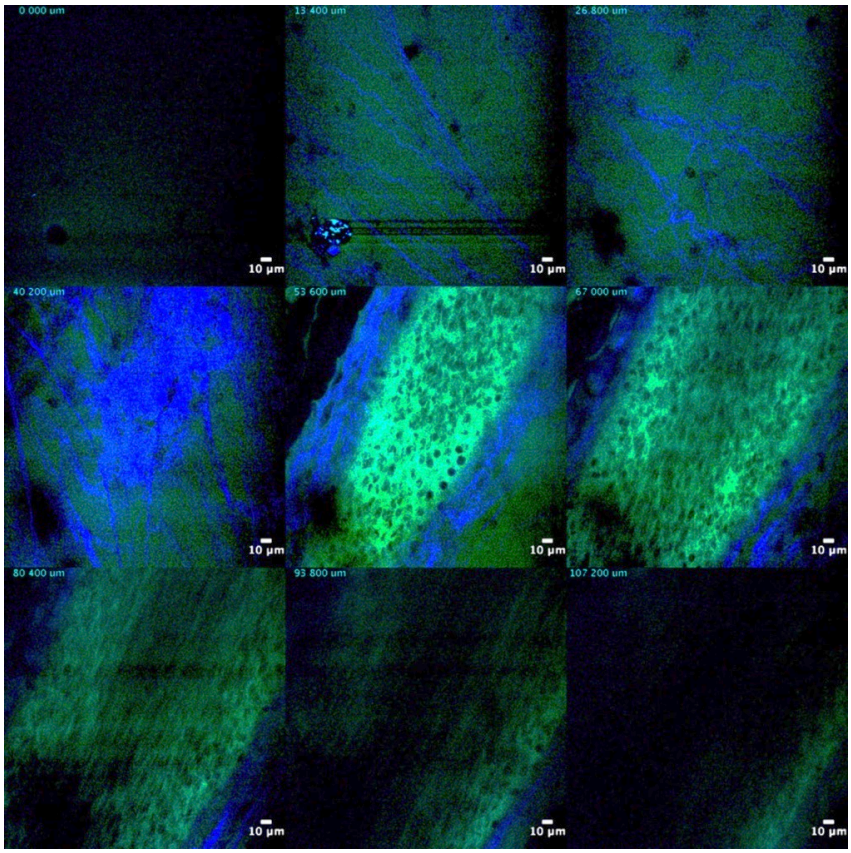

Figure 4-2 Intravital images of artery vessel with different depth. Images are generated by montaging the image sequence from a 20 FPS time-lapse video. The depth step of each image is 13.4 μm, which means 2 s in time in the 6.667 μm/s axial scanning speed condition.

Also, this 3D scanning multiphoton microscope was further tested in highly scattering tissue, the spleen, which is an essential organ for immunology study [233]. This time, we used a transgenic GFP mouse as our sample. The spleen was extracted from the back of the mouse

without wounding the other organs and tissues. The image results are shown in Figure 4-3. Here, the blue channel signal is still coming from the collagen tissue due to SHG, and the green signal is from the intrinsic GFP cells, the red signal is from the blood flow labelled with rhodamine dextran. The spleen is integrated with the body in life without any further preparations. The total imaging depth for the spleen is about 50 μm in our system.

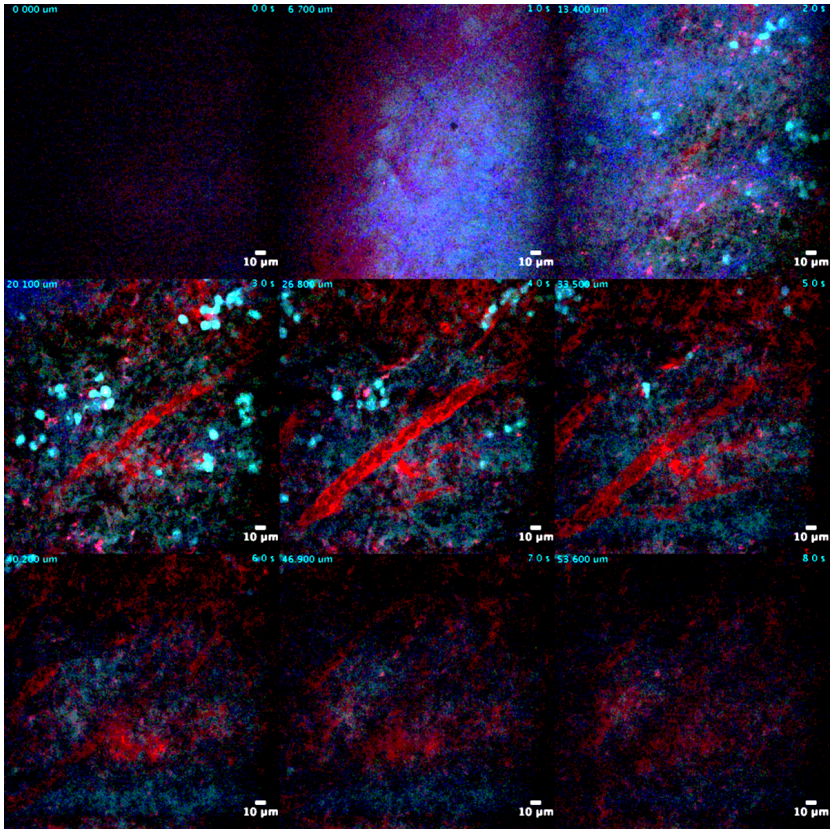

Figure 4-3 The *in vivo* spleen image over different depth of GFP mice. The depth is increased from left to right, and top to bottom sequence. Each step is about 6.7 μm, which is 1 s interval sampling from a 20 FPS video with 6. 667 μm/s axial scanning speed.

In addition, platelets volumetric imaging in microfluidics was conducted. The image results are shown in Figure 4-4. The platelets (green signal) are attached to collagen (blue signal) on a microfluidic channel. The image was recorded in video-rate (20 FPS). By the high SBP zooming imaging, fibrin network among the platelets is resolved. The 3D image was reconstructed by ImageJ volume viewer plugin.

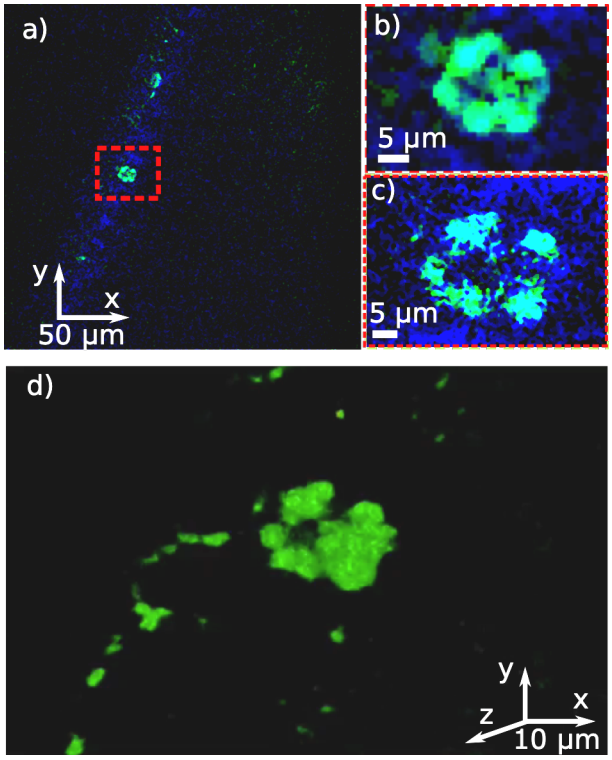

Figure 4-4 *In vitro* human platelets adhered to the microfluidic channel. a) 2s averaged image of platelets, with imaging format of 20 FPS and 512 x 512 pixels. b) Zoomed image of red dashed area in a). c) 5 x anamorphic polygon scanning zooming image of the same area in b). d) 3D reconstruction of platelets in a) area. It was processed by 3D Viewer plugin of ImageJ.

4.1.2 Deformable Mirror

The mechanical stage provides a simple solution of volumetric imaging, with an extended scanning depth without limitations of different types of biological samples. However, the response speed of the mechanical stage is limited to a level of a few milliseconds to seconds, which is not fast enough to capture dynamic movements in biological samples. Another method is using optical beam scanning to replace the mechanical scanning. Here in this subchapter, I will introduce the use of the DM to shift the focus in the axial direction via modulating the wavefront of the beam at the frequency of kHz. The optical schematic diagram is shown in Figure 4-5 a). In which, the polygon constituted the fast axis scanning device in the horizontal direction, GM scanned along the orthogonal direction of polygon scanner, and DM functioned as the axial direction scanning device. The setup is developed from the system as we introduced

in the polygon microscope chapter, with the notable difference of conjugating a DM to the polygon and GM. The scanning volume is shown in Figure 4-5 b).

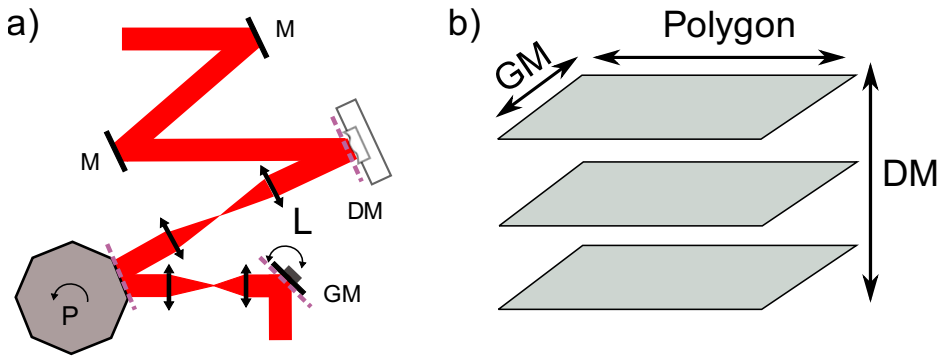

Figure 4-5 a) The optical schematic diagram of volumetric scanning setup by DM. b) The illustration of relations between volumetric frames and scanning devices.

The synchronization of signals is the same as the polygon multiphoton microscope, which polygon triggers the horizontal synchronization signal HSYNC, GM triggers the vertical frame synchronization signal VSYNC. The only additional step is synchronizing the DM update signal with the VSYNC so that each frame will have the same imaging depth during the scanning period. The relation between the control and synchronization signals are shown in Figure 4-6.

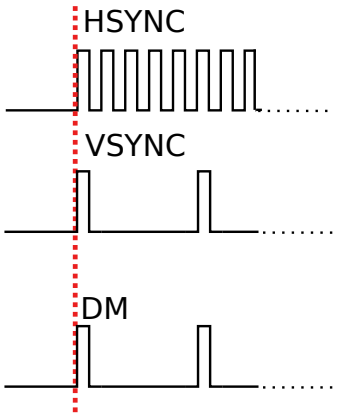

Figure 4-6 The plot of control and synchronization signals in time sequence loop.

The phase mask we applied to the DM is a simple defocus aberration, Z5. The principle is shown in Figure 4-7. Since the direction of light is the gradient of the wavefront, the parabolic

wavefront will generate a focus where the position is based on paraxial approximation. This principle is drawn in Figure 4-7 a), in which the pupil function at the BFP of the objective is modulated by the DM, with an equation as

$$P_d = Pupil(x,y)e^{(-ikW(x,y))}\ , \qquad \text{Equation 4-1}$$

in which, P_d denotes the pupil function after defocus, $Pupil(x,y)$ denotes the pupil function, which is a circular function for the spherical lens, k denotes the wavenumber, and $W(x,y)$ denotes the wavefront. The wavefront of $W(x,y)$ for defocus is

$$W(x,y) = a_5 \cdot \sqrt{3}[2(x^2+y^2)-1], \qquad \text{Equation 4-2}$$

which is the defocus Zernike term in aberration equation.

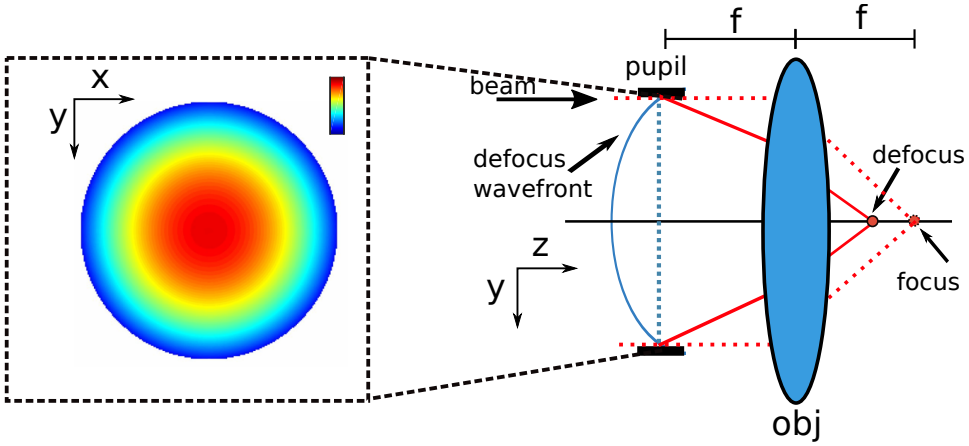

Figure 4-7 Principle of DM based axial scanning. a) Defocus aberration at the pupil of objective generated the shift along the axial direction (z). Dashed lines indicate the input beam with flat wavefront, as a reference beam and reference wavefront.

As we know, the PSF is the Fraunhofer pattern of the incident optical field at the pupil plane [184], which is the Fourier transform of the pupil function. Moreover, with the defocus aberration, the pupil function becomes into effective pupil function which will degrade the imaging performance. However, fortunately, in multiphoton imaging, only confined area is stimulated due to the nonlinearity absorption effect, which suppressed the unwanted signal, as shown in Figure 1-9. Thus the PSF with minimal aberration is maintained even at an extended

depth of field. This multiphoton absorption feature releases the requirement of deconvolution, which is demanded in other microscopes [234-236].

The depth of field equation can be derived from the geometry of the optical beams as [144],

$$D = 4n^3/NA^2(\frac{R_{BFP}}{R_{DM}})^2\Delta a_5, \qquad \text{Equation 4-3}$$

where D denotes the depth of field, n is the refractive index of the immersion media between the objective and the sample, Δa_5 is the maximum defocus stroke (PV, μm) of DM, λ is the wavelength of light. Here in our usage, the stroke is the amplitude of the Z5 aberration coefficient, which can be retrieved from the datasheet of Thorlabs. Given the peak to valley (PV) of $\pm 6.5\,\mu m$ within the 10 mm diameter pupil, the corresponding defocus stroke coefficient is $\frac{13}{W(1)-W(0)} = 3.75\,\mu m$. In our setup, the NA of our objective (Zeiss 1.0 NA 20x Apochromatic) is 1. The refractive index is about 1.33 for water immersion medium, substituted all these values into the depth equation, we get the calculated ΔS is about 79.40 μm, which is the achievable scanning range of our DM based volumetric multiphoton microscope.

DM device is flexible in changing the value of stepping sizes of the aberration coefficients, which allowed the rapid changing of both the speed and the number of frames contained per volume. Comparing to the speed of light sheet microscope, which provides 100 FPS for 2-dimensional imaging and 1 to 10 VPS in 3-dimensional imaging [53], our DM based volumetric multiphoton microscope can reach 100 FPS with a anamorphic FOV as 450 x 280 μm^2, and 1 kHz DM scanning speed in axial direction with variable step size (~ μm). Therefore, this DM based volumetric multiphoton microscope has comparable speed of light sheet microscopy, and extra benefits in deep tissue imaging of mammal animal, like rodents, as well as multi-channel RGB imaging ability.

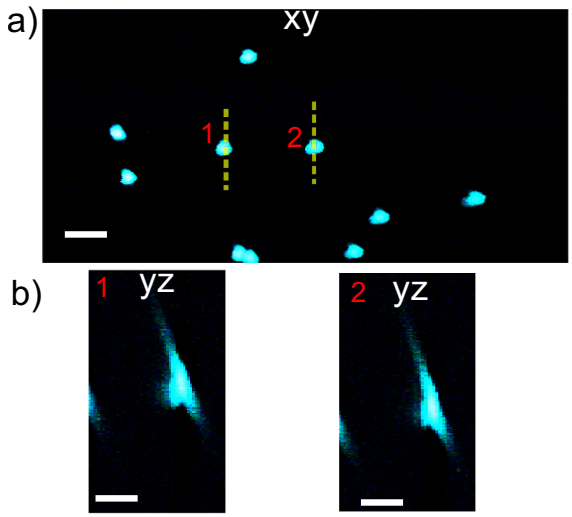

Figure 4-8 Image of 3 μm beads. a) Single lateral image without averaging in lateral (xy) direction at 20 FPS. Scale bar, 10 μm. b) The axial plot of the yellow dashed line 1 and 2 in a). This axial image is obtained by DM based axial scanning without averaging, step size is 0.4 μm, with 1 VPS rate. Scale bar, 5 μm.

To characterize the performance of DM based axial scanning, first, we used 3 μm diameter beads to testify its lateral and axial dimension obtained from volume scanning. The imaging results are shown in Figure 4-8. In which, b) 1 and b) 2 are the digital zooming image of yellow dashed line area in a) in lateral and axial direction respectively. The measured lateral diameter is about 3 μm. It clearly shows that in the axial direction, the bead image was elongated about three times comparing to the lateral measurement, which follows the theoretical equation of xy and xz direction PSF introduced in the second chapter of this thesis. These images are obtained from a single image frame without any averaging, so the glitches at the boundary of each beads profile can be smoothed with the averaging process by acquiring more frames as what usually done. Here we only showed the raw data to prove that using DM with defocus pattern can achieve the high-quality axial scanning in accordance to the TPA theory. This PSF might be degraded by residual tilting aberration from the DM mirror, since the DM is not allocated vertically but obliquely to the laser beam.

We further testified our DM based axial scanning with pollen grain sample. The results are shown in Figure 4-9. In a), a 2 s averaged 2D image without axial scanning is shown. In b),

the volumetric image of the same area but without averaging is displayed. This volume image is rendered by Imaris software; the volume contains 10 frames with a total scanning time of 0.5 s. It clearly shows that pollens located at different depth has been captured by volumetric scanning, providing much more information than a simple 2D image.

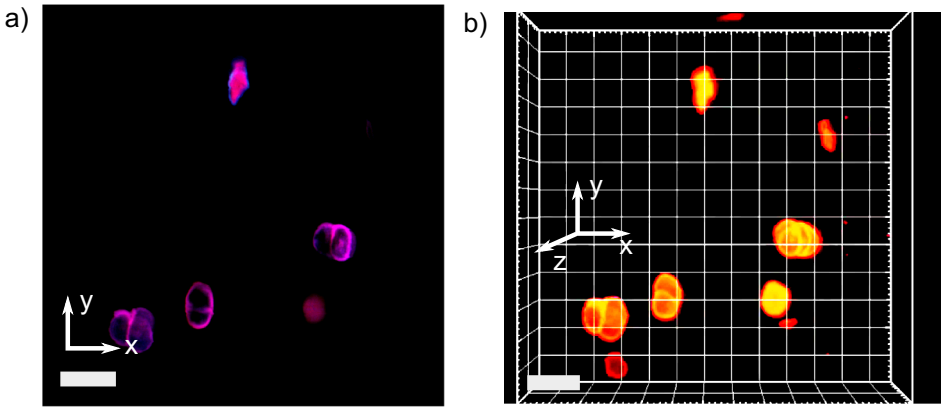

Figure 4-9 Image results of pollen grain slide. a) 2 s averaged 2-dimensional image without axial scanning. Scale bar, 40 μm. b) 3-dimensional reconstructed image from the same area of the image in a) but with axial scanning by DM. This image is reconstructed from a single frame without averaging; the total acquisition time is 0.5 s, at 20 FPS rate for 2-dimensional frame, and 2 VPS in volume. This image is reconstructed by Imaris software. Scale bar is 40 μm.

To further testify the high-speed imaging ability, time sequence of volume images from a dynamically fluidic sample of 3 μm beads are shown in Figure 4-10. This volumetric time sequence images are extracted from Imaris rendered volumetric movie, with 10 frames per volume (2 VPS). From a) to j), 10 time points are chosen for demonstrating the ability to capture the motility process in volume.

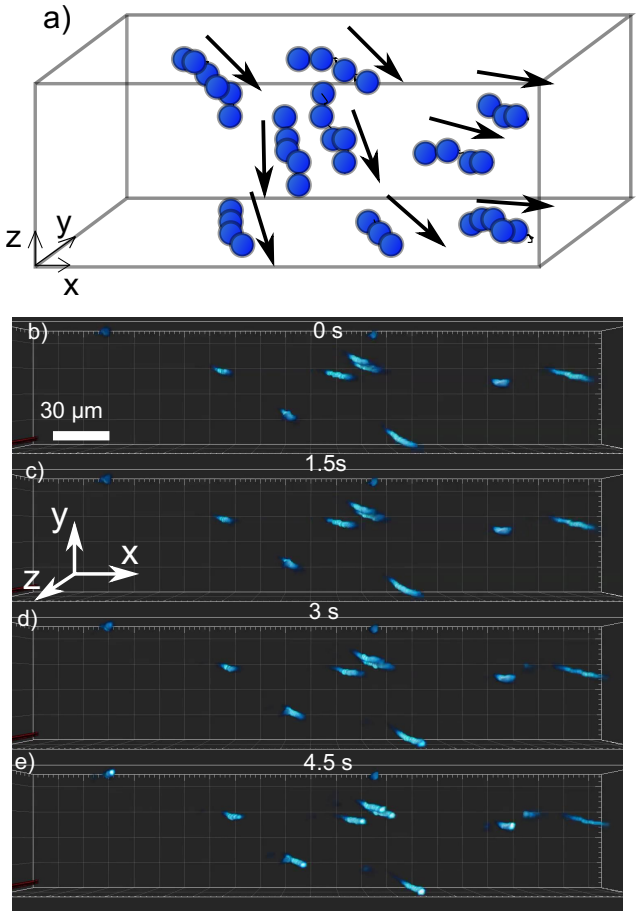

Figure 4-10 Time-lapse video of high-speed volumetric image of flowing beads by DM scanning. a) Schematic diagram of volumetric beads tracking. b) to e) are reconstructed single volume frame by a time interval of 1.4 s for 4.5 s in total. The volume rate is 2 VPS at 20 FPS frame rate, so 10 frames in each volume. Here we chose one frame from every three frames in order to show the tracking of beads. The video is reconstructed by Imaris software, by importing the sequence frames with numbered prefix labelling on the name.

In summary, the synchronization of the polygon mirror and DM enabled the fast volumetric scanning. TPA effect confines the stimulation area, high-quality imaging is maintained for both focused and defocused situations. Furthermore, in this design, deconvolution is not required for volumetric image recovering, which is an advantage over other fast imaging methods. Despite the current achievable axial scanning range of 80 µm, the scanning range can be further extended without limitations through the full range mechanical

stages, which in together constituted a complimentary axial scanning scheme. Overall, both the range and speed are retained in our system.

4.2 Photomanipulation

Photomanipulation is a wide range of techniques, attached to the microscope's high precision function, for interacting with the sample via light beam at the accurate scale comparable to the resolution of microscope [237]. Using photomanipulation, it becomes possible to initiate the biological process of interest during the observation instead of doing time-lapse imaging in hours or searching through large populations of cells. In some cases, photomanipulation function can trigger specific processes which are not being possible to observe without external activation. Photomanipulation can be used as an operation tool to precisely manipulate the biological sample, by affecting the local chemical compounds (photochemical effect) or physically destroy parts of the tissue (laser ablation). The key factors in achieving photomanipulation are the modulating of laser power with selective positioning control. Therefore, the choice of power engineering device is critical in photomanipulation. In the next section, I shall first introduce the instrument requirements for photomanipulation and typical applications.

Photomanipulation is a technique with various possible applications, such as photobleaching [238], photochromism [239], optogenetics [240, 241], photoablation [242] and uncaging [243] of biomolecules. All these applications are based on the light tissue interaction, which can be grouped into 4 effects: photochemical, photothermal, photoablative and electro-mechanic [244]. In addition, the combination of mode-locking and spatial focus provides the high-intensity pulse for laser medical surgery, since its accumulation of both time and space localized the interaction area and minimized the unwanted thermal effect [244]. Photodamage, including phototoxicity and photobleaching, needs to be concerned in photomanipulation applications [245]. The photodamage is caused by the oxidize reactants generated after the fluorophore stimulation. However, through monitoring the fluorescence signal or temperature level, feedback laser power control can mitigate the damaging effect. One of the representative

trials is controlled light exposure microscope, which used fluorescence signal to control the laser power so that for a brighter area less power is used while in weak area more power is added [246]. It broadened fluorescence intensity over two folds and was applied to image different cells with reduced photobleaching. Another important application area of photomanipulation is in the medical study. For instance, laser ablation surgery, based on the mechanism of photothermal and photon induced plasma, can generate the smallest stroke for blood thrombus analysis[247]. In summary, laser photomanipulation is an important tool for a broad area of studies. However, the utilization of this technique is still limited by delivery of ballistic photon. In the next section, I shall introduce the hardware for achieving photomanipulation and the representative photomanipulation techniques.

4.2.1 Hardware for Photomanipulation

For realizing the photomanipulation, laser power modulation devices are needed. There are various power modulation devices. The two primary choices are acousto-optic modulator (AOM) and electro-optic modulator (EOM). AOM uses ultrasonic wave to modulate a crystal for generating grating structure with the periodic refractive index. The grating will diffract the input light beam with a controllable angle and efficiency by changing the frequency and amplitude of the driven acoustic wave [145, 248]. EOM utilizes a crystal with electrically controllable refraction index to rotate the polarization of input light through birefringence. EOM will also be called Pockels cell if the independence of the index and the electrical field is linear. Therefore, EOM can be seen as a controllable waveplate, which will change the light's polarization state resulting in the target intensity by adding a polarizer.

Ideally, the laser power modulator should have short response time, large working wavelength, high optical transmission efficiency, low wavefront distortions, considerable modulation depth and high elimination contrast. In ultrafast laser optics, the frequency-dependent delay, known as dispersion, plays a crucial role in temporal broadening the laser pulse. Based on the multiphoton absorption efficiency equation, the peak power is inversed proportional to the laser pulse duration, and the excitation efficiency is nonlinearly dependent onto the peak power, so the expansion of laser pulse will lower the 2p stimulation efficiency at

a certain level. Pockels cell (EOM) is used more often than other devices in laser power control. The comparison between EOM and AOM is shown in Table 3_1 in detail [249].

Table 4-1 Comparison between EOM and AOM [249].

Feature/Spec	AOM	EOM
Rise Time	9 ns	40 ps
Transmission Efficiency	70 ~ 90%	70 ~ 90%
Contrast	>5000:1	<200:1
Cost	~ 2000 USD	~ 2000 USD
Dispersion	High	Low
Stability	Excellent	Good
Size	Compact	Large

At the system level, there are several techniques for photomanipulation microscope, for example, using field diagram to switch the light beam between imaging and photomanipulation, but field diagram method is slow and lacks targeting flexibility. The other options are using scanning devices, like DMD and GM. As we discussed before, DMD is based on the amplitude modulation technique for achieving diffraction effect, which allowed simultaneously multisite photomanipulation. Nevertheless, the weakness of DMD is the relatively low light transmission rate, which limits the photomanipulation efficiency. Currently, the widely used photomanipulation method in markets is based on the GM scanner, for its target flexibility, light transmission efficiency and location accuracy. However, the main drawback of GM is its speed cannot match the requirement of video-rate LSM. The current solution is switching between two groups of scanning devices, which increased both the cost and the complexity. Therefore, there is a demand for combining the speed and flexibility into one microscope platform. In the next section, I will present the polygon based photomanipulation microscope, with only one group of integrated scanning devices, but achieved both video-rate imaging and flexible multisite photomanipulation.

4.2.2 Applications of Photomanipulation

The integration of fluorescence labelling and photomanipulation technique had led to several applications in developing advanced fluorescence microscope for quantitative biological studies. For the application of photobleaching, fluorescence recovery after photobleaching (FRAP) [238] and its counter fluorescence loss in photobleaching (FLIP) [250] are being used for the quantitative study of molecule diffusion and structure compartmentalization. The two significant applications of photomanipulation are shown in Figure 4-11, in which thrombus formation and haemorrhage process by laser injury and FRAP signal plot are shown in a) and b) respectively. The laser injury provides a tool for investigating the dynamics of thrombus and clot metabolism by artificially introducing the high-intensity laser pulses to breakdown the blood vessels. FRAP explores the molecule diffusion rate through monitoring the process of fluorescence recovery before and after localised photobleaching by intense irradiation. FRAP was first achieved in the TIRF microscope for protein mobility study on the cell membrane [251]. One key factor in FRAP is the recovery time of at half of the initial level.

On the contrary, instead of looking at the recovery rate of the bleached area, FLIP looks at the loss of nearby area after repeated photobleaching. At first, FRAP can only be used to study the diffusion rate at lateral direction because the widefield microscope does not have the axial optical sectioning ability. Three-dimensional diffusion rate measurement is possible in the multiphoton microscope because of the high confinement TPA effect [252].

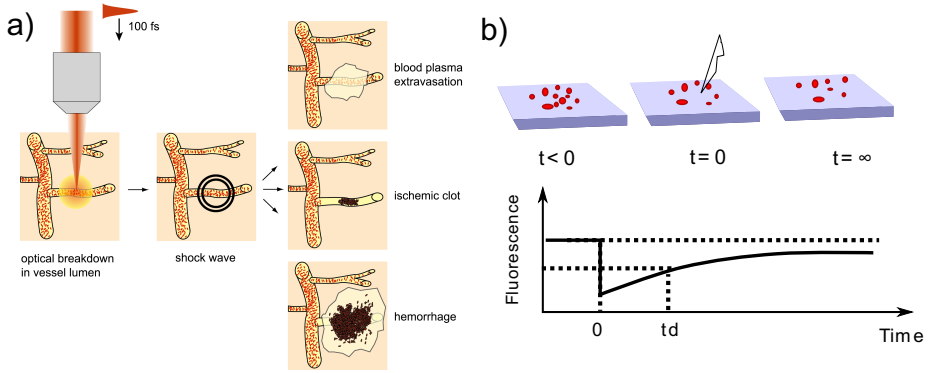

Figure 4-11 Applications of photomanipulation. a) Schematic of laser induced vessel injury, the metabolism process of thrombus formation and resulted haemorrhage reaction are being presented.

This image is adapted from [253] with permission. b) Diagram of FRAP process. Red spheres represent the fluorescence molecule. At time 0 on the top middle plot, an intense light was illuminated onto a round area surrounded with dashed lines, indicating the area being bleached. The bottom plot is the fluorescence signal in time sequence during the FRAP process. In which, td denotes the time when the brightness come back to half of the value before bleaching, which is an important parameter of the recovering speed. The recovering speed can calculate the diffusion rate of the molecules. [253] [254]

Also, to manipulate the fluorescent sates of proteins or dyes, the physical or chemical states of the specimen can also be managed by photomanipulation technique. In the multiphoton microscope, the highly spatial-temporal concentrated photons could be used to physically destroy a tiny part of the sample without affecting the surrounded area. With the tuning of power of the laser, ablation effect can vary from cutting subcellular organelles to individual cells and part of the whole tissues. There are many different applications of this photoablation effect, such as the study of the tissue repairing process after artificial trauma. The laser ablation facilitated the study of biological pathways and cell migration in the tissue-damaging metastatic processes like wound healing and inflammation [242] by introducing ablation wounds.

There are other critical applications of photomanipulation, such as the single-molecule localization microscope (PALM/STORM) by utilization of photoswitchable fluorophores [9, 10], tracking of specific objects in the complex microenvironment with massive cells [254]. The integration of photomanipulation and fluorescence labelling technique has transformed the biology research with exhibited information which was previously invisible. Therefore, the engineering of the laser beam's power and accuracy control of position is vital in microscope designing.

4.3 Photomanipulation with Binary Slit

The high precision polygon used in the multiphoton microscope is an electromagnetic effect based spinning mechanism with a certain level of inertia, so it is not possible to stop and start in an interval short enough for switching between widefield imaging and localised

photomanipulation. Photomanipulation function is responsive to a full application in selective activation and laser surgery. The hardware for photomanipulation is based on the laser power modulator device and high accuracy scanners such as GM. However, GM has been suffered from limited scanning speed which constraints its utilization in capturing and imaging dynamic biological samples. The comparisons between polygon and GM in the two functionalities of imaging and photomanipulation are shown in Figure 4-12, advantages and disadvantages of polygon and GM in each application are depicted. In our current volumetric microscope design, we utilized the superior polygon mirror to do flexible raster scanning, with minimal optical aberration and flexible imaging speed. While in the manipulation scenario, GM is an ideal device to provide random scanning ability with high accuracy but at a slower speed comparing to polygon scanner.

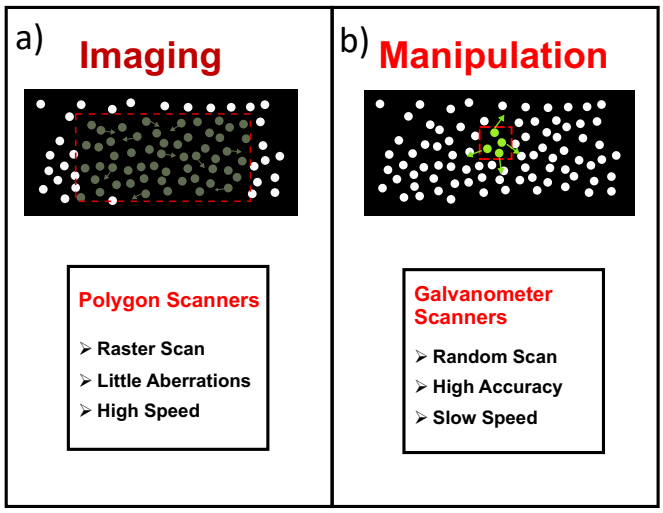

Figure 4-12 Modalities of wide-field imaging and localized photomanipulation. a) Imaging mode, in which, the spheres represent the sample, the red dashed square indicates the area that is being activated by the light illumination, by the different color of spheres. b) Diagram of photomanipulation. A smaller area is activated by high-intensity illuminating light. The features of the polygon mirror and GM are demonstrated below.

Therefore, there is a demand of building an integrated system of using both the advantage of polygon and GM, as a multimode platform with high-speed imaging and high accuracy photomanipulation, without costing too much of photon budget. There are several designs to

achieve this, such as using two scanning systems for two modes, or through high diffraction device like AOD to scan the position [255]. However, either way is complicated and redundancy in hardware design or introduce additional dispersions, which would degrade the TPA rate.

Here we put forward a simple, novel, efficiency and economical design, through allocating a binary slit with 150 μm width (Thorlabs, S150R) at Fourier plane of scan lens, we combined the polygon mirror and the virtual conjugated GMs. Schematic diagram of this design is shown in Figure 4-13. In which, polygon mirror is conjugated to a virtual conjugated GM pair, denoted as GM-X and GM-Y indicating the scanning directions. With the control of the slit's position, this design replaced the requirement of stopping the rotation of polygon for separating and decoupling from GM based localized photomanipulation.

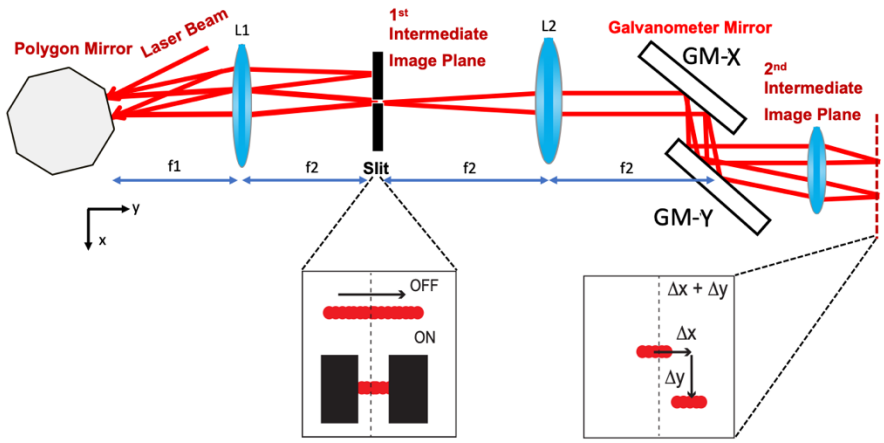

Figure 4-13 Schematic diagram of the scanning design of photomanipulation polygon microscope. The input laser beam got scanned by the polygon mirror. L1 and L2 are two achromatic lenses which composed a 4f system for delivering the laser beam to the GMs. GM-X and GM-Y are closed to each other as virtually conjugated, to reassign the beam to any lateral position. The slit was allocated onto the first intermediate image plane to truncate the beam into a narrow stripe.

The switching control of slit is based on a motorized flip mount (Thorlabs, MFF101/M), with switching speed up to 0.5 s. It has a 90° transition between two holders, except for the slit, the other branch is installed with a half waveplate (HWP). So, in imaging mode, the HWP

together with a polarization beam splitter, will modulate the laser power at a low intensity for imaging. When the slit is on, all the light will pass through the beam splitter to generate high-intensity illumination for laser manipulation. The illustration of this design is shown in Figure 4-14. It achieved the ability of rapid switching both the light's power and imaging area at the same time. The localized segment size can be derived from an equation as $f_1 \cdot \sin(\theta)$. in which, f_1 is the focus length of the scan lens, θ is the deflection angle of the polygon. In our setup, f_1 equals 30 mm and θ equals 20°, so the total scanning length is about 10.2 mm, which will generate a 6.5 μm width segment in the final image plane. In Figure 4-14, the bottom is an image of rhodamine stained paper tissues sample. The image is built by scanning the GM-x scanner at a 0.02 V amplitude step with the slit on, and it shows that using the GM in our design can retrieve any position within the FOV in the imaging mode.

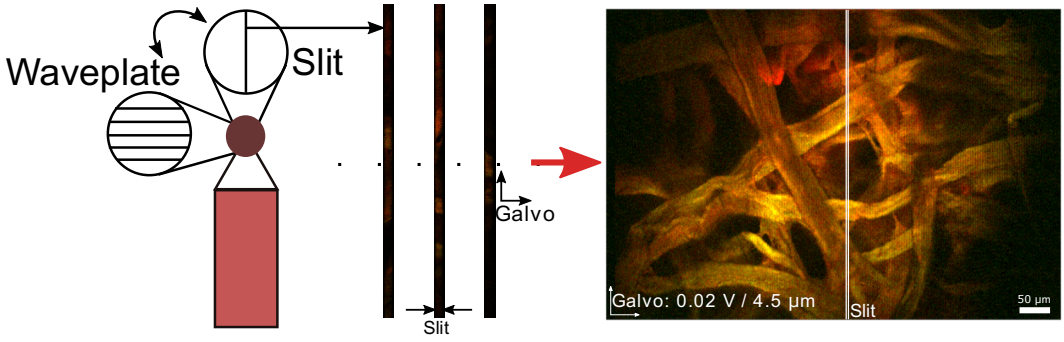

Figure 4-14 Schematic diagram of the motorized slit holder, in which the reconstructed image is available with the slit opening.

The final multi-site photomanipulation is based on the reassignment of scanning areas, which are selected from the averaged image of the interested area in advance. This process is drawn in Figure 4-15. In which the image plane is still synchronized with the HSYNC and VSYNC at the same frequency as imaging mode. So the position of the slit will stay at the same position of the image plane, and the scanning of GM will scan the selected area. The digital image displayed on the screen will be similar to the GM reassigning the different areas to the position of the slit. The position of amplitude is calibrated through registration of the position and input GM amplitude, which is a constant coefficient between voltage and pixels. Electronic control signals are shown in the inset of Figure 4-15. G-X and G-Y are voltages of

GM in horizontal and vertical direction, respectively. The G-X and G-Y signal are both synchronized with the VSYNC signal, so for each frame, the site can be a shift to a different position, and the number of frames (dwelling time) for each site can be controlled as well. In our current setup, in total staying length is 200 s long, within this duration, an arbitrary number of sites can be selected with programmable dwelling time.

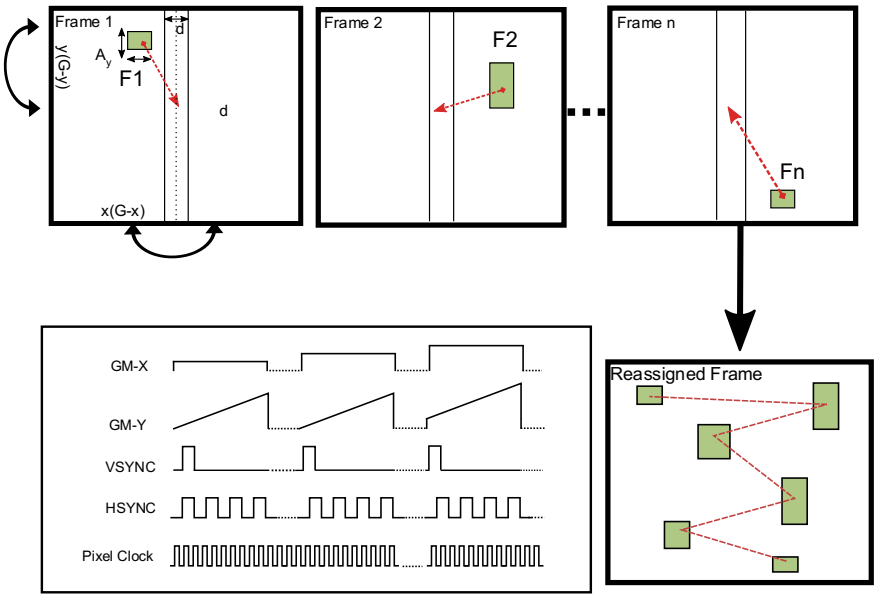

Figure 4-15 Schematic of selective photomanipulation process. The horizontal size of the localisation area d is determined by slit width. The amplitude signal of GM-Y determines the height A_y. Each target site can be selected in the averaged image in advance, through an array of coordinates, the chosen site F1, F2, …, Fn will be scanned sequentially in time. The inset plot is the sequence of control and synchronization signals.

The testing results of our method is shown in Figure 4-16. Here we wrote "ANU" onto three pollens through multi-site photobleaching. The coordinates are selected by using the averaged image as the map, by simply clicking the interested area. The dwelling time is 1 s for each site, and the bleaching power is 120 mW after the objective. Figure 4-16 (b) is the plot of bleaching accuracy. It demonstrates that the accuracy this setup can achieve is 3 μm, and the size of the bleaching square is about 6 μm, which matched well with the calculation.

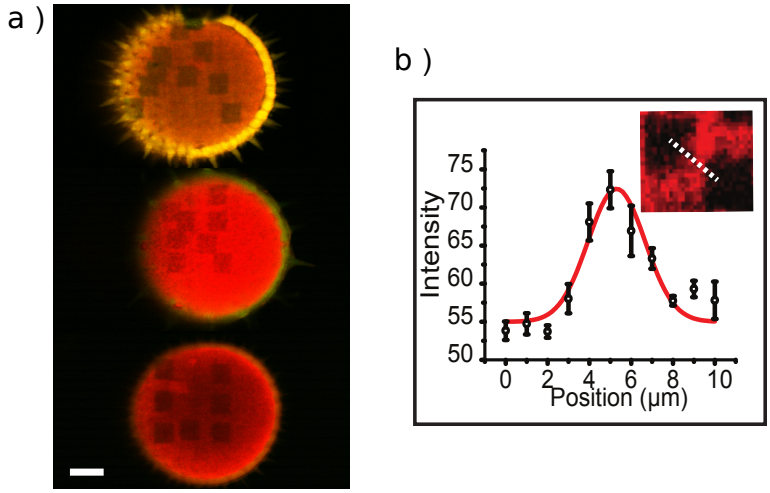

Figure 4-16 Multisite photobleaching experiment results. a) Pollens were bleached with the controlled pattern "A","N","U" respectively. Scale bar, 10 μm. b) Line plot of the two closest photobleaching squares.

4.3.1 *In vitro* Fluorescence Recovery After Photobleaching

Now, in this polygon based multimode microscopy platform, with controlled laser illumination intensity, rapid switching of illumination area and dwelling time, combined with the flexible spatial and temporal formats that polygon system provided, quantitative biological study at an unprecedented accuracy is allowable. The first experiment we applied is FRAP in fluorescent Giant Unilamellar Vesicles (GUV) and fluorescens.

FRAP can be used to measure the diffusion dynamics of molecules in the interesting medium, such as water and lipid. In FRAP, a high-power illuminating laser will be used to bleach a localized area, and then the recovery process of molecules will be recorded. The recorded data of recovery time and image intensity will be used to calculate the molecules diffusion rate. The FRAP experiment results of fluorescent isothiocyanate (FITC) water solution is shown in Figure 4-17. The FITC solution was made by mixing 10 mM FITC powder in phosphate-buffered saline (pH 7) thoroughly. Figure 4-17 a) i) is the 512 x 512 pixels image of the FITC sample after photobleaching. ii) is the digital zoomed image of the red square area, which has limited resolution due to the low SBP. iii) to v) are segments from high SBP (5120 x 512 pixels) imaging mode with 10 times optical zooming. This flexible polygon zooming

function in imaging mode greatly enhanced the accuracy in the measurement progress of fluorescence recovery. The intensity plots are drawn in Figure 4-17 b). The exponential fit equation is

$$I(t) = I_{final}(1 - e^{-\gamma t}), \qquad \text{Equation 4-4}$$

where $I(t)$ denotes the unified fluorescence intensity, and I_{final} is the plateau level value after recovery, γ is the time recovery coefficient. Here in the plot, the fitting value of γ is 0.7845 s, and I_0 is 0.7572. Using the diffusion equation [250]

$$I(t) = I_{final}\sqrt{1 - \frac{w^2}{w^2 + 4\pi D t}}, \qquad \text{Equation 4-5}$$

where w is the width of the bleaching area, D is the diffusion rate, the diffusion rate was calculated as 8.96 μm^2/s, which is compatible with previous studies [256].

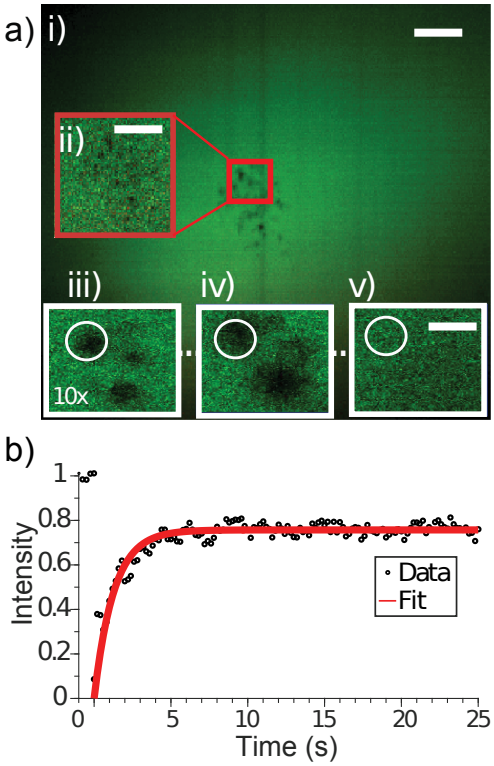

Figure 4-17 FRAP results of the FITC solution. a) Image frames of FRAP with low SBP and high SBP. i) 2 s time-averaged FITC image with 512 x 512 pixels after photobleaching, scale bar: 10 μm.

ii) Digital zoomed image of i) at the interested bleached FOV, single captured frame without averaging. (iii) - (v) are photobleached areas acquired sequentially from 1 to 22 seconds at high SBP (10 times polygon zooming) imaging mode (Scale bar: 1 μm). b) Line plot of the fluorescence intensity in the recovering process.

In addition, FRAP was applied to measure the lipid medium diffusion through using sulforhodamine B - labelled GUVs, with the density of sulforhodamine B - labelled sucrose as 2.5 μM for bright fluorescence. GUVs were prepared with an electro - swelling device for 200 minutes (Nanion, Germany: Vesicle Prep Pro) based on electroformation effect [257]. The materials are made by a mixing solution of diphytanoyl phosphatidylcholine (Sigma - Aldrich, Avanti Polar Lipids, USA), and encapsulating 2.5 μM sulforhodamine B (Sigma - Aldrich, MO, USA) with 100 mM sucrose solution. Then GUVs were diluted into 100 mM glucose solution for the FRAP experiment. In GUV FRAP, the bleaching area is not fully bleached, so the fitting equation is adapted to

$$I(t) = I_{final}(I_R - e^{-\gamma t}), \qquad \text{Equation 4-6}$$

where I_R denotes the residual intensity after the bleaching. Multi-site bleaching is applied to the same GUV, in which two different sites are bleached in sequent, and measurement results are shown in Figure 4-18. Here the fitting results for the first site in Figure 4-18 a) are $I_{final} = 0.1417, I_R = 7.0836, \gamma = 0.2427$, for the second site are $I_{final} = 0.1231, I_R = 8.1612, \gamma = 0.3543$. The corresponding diffusion rates are 3.71 and 5.40 μm^2/s, respectively. The discrepancy of the diffusion coefficients can be attributed to the difference in the amount of bleaching. Since site 2 has stronger bleaching, more molecules will need to be replenished, leading to the difference in diffusion rate measurements. This result is consistent with the published documents [256].

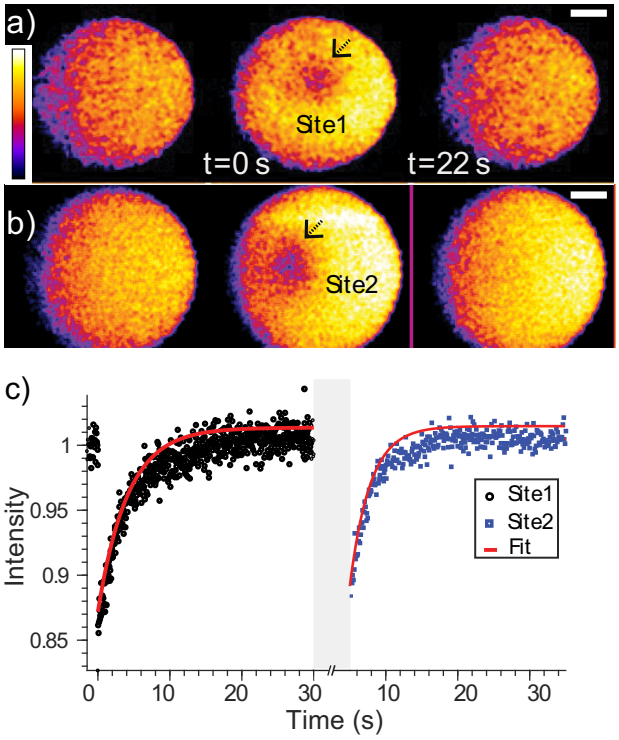

Figure 4-18 Results of multisite FRAP in GUV sample. a) Imaging of GUV at different time points in the FRAP experiment, from left to right are before bleaching and after bleaching. Image is at 5 times optical zooming with 200 nm pixel size. b) A different site of bleaching of the same GUV in a). Scale bar: 10 μm. c) The fluorescence intensity recovery plot over time with the two sites.

4.4 Photomanipulation for Study of Thrombosis

4.4.1 Vasculature Imaging

The multiphoton microscope is a powerful tool but still has its limitations; therefore, the application scenario should be chosen carefully. There are multiple research areas and disciplines that multiphoton microscopy can apply, like imaging of intact neurons, immune cell interactions. However, vascular imaging is perhaps a challenging target due to its highly dynamic movement. The vascular system is part of the network of the circulatory systems for pulmonary, cardiovascular and immune functions to sustain a working network of organs. The study on the health of vascular systems, therefore, will be related to angiology, nephrology,

haematology, hepatology, neurology and oncology as well as immunology [258]. In all the above areas, the multiphoton microscope has been successfully applied to achieve cell monitoring, molecule imaging and drug delivery testing also. A key strength in the multiphoton microscope is the study of blood dynamics event in the living host that is continually changing due to external stimulations. Even though there is usage of microfluidics to mimic the vascular environment, the study of intravascular activities can only be conducted in a living body [259].

The study of vasculature is also related to immune responses, which are results of various complex and dynamic individual cellular behaviours interacted with microenvironment factors. Previous *in vivo* experiments can only provide cell population information while *in vitro* experiments are in an artificial environment. Therefore, the multiphoton microscope which maintains the natural environment and provides the single-cell level real-time observation is the tool that is pressingly needed in immunology research [260].

In oncology, the most attractive question is how the microenvironment affects the development of the tumour and how the tumour cells migrate to different organs (metastasis) [261], which means tumour research cares about not only the development of the cancer, but also the microenvironment and metastatic growth [262]. There is an intense demanding of observing tumour cell migrating to the vascular system and also analysing the signal pathway in this process. In this study, the priority is longitudinal imaging and tracking of the interested cells in complex tissues, which means the primary requirement of microscope for tumour study is mostly on imaging depth and spatial resolution than the temporal resolution.

The blood vessel structure diagram and application scenarios are demonstrated in Figure 4-19. As shown in Figure 4-19 a), there are multiple cells and interactions in the blood vessel, which will affect the physiology process, such as fatal stroke induced by the formation of thrombus due to the clotting and platelets functioning. The thrombus imaging in the brain area is shown in Figure 4-19 b). In addition, white blood cells (e.g. neutrophil) can migrate to target areas for immune function through the vessel network, which is essential for immunology study. The immune cell migrating and interaction process is shown in Figure 4-19 c), which shows a leukocyte transendothelial migration as a significant inflammatory response. The using

of IVM to look at vessels during the migration process helped to answer that transient receptor potential canonical 6 (TRPC6) is a calcium channel responsible for endothelial cytosolic free calcium ion concentration, thus is beneficial for the immune cell migration. Another critical application of vascular imaging is tumour microenvironment and angiogenesis study. Figure 4-19 d) shows the protrusion of tumour along the blood vessels by IVM imaging of mouse ear with D2A1 LifeAct-YPet-expressing cells after 2 weeks of injection [263]. Here the blood vessel plays a vital role for answering the question about tumour metastasis process. In the next section, I will demonstrate the results of applying our photomanipulation technique to induce thrombus in the mouse's vessel.

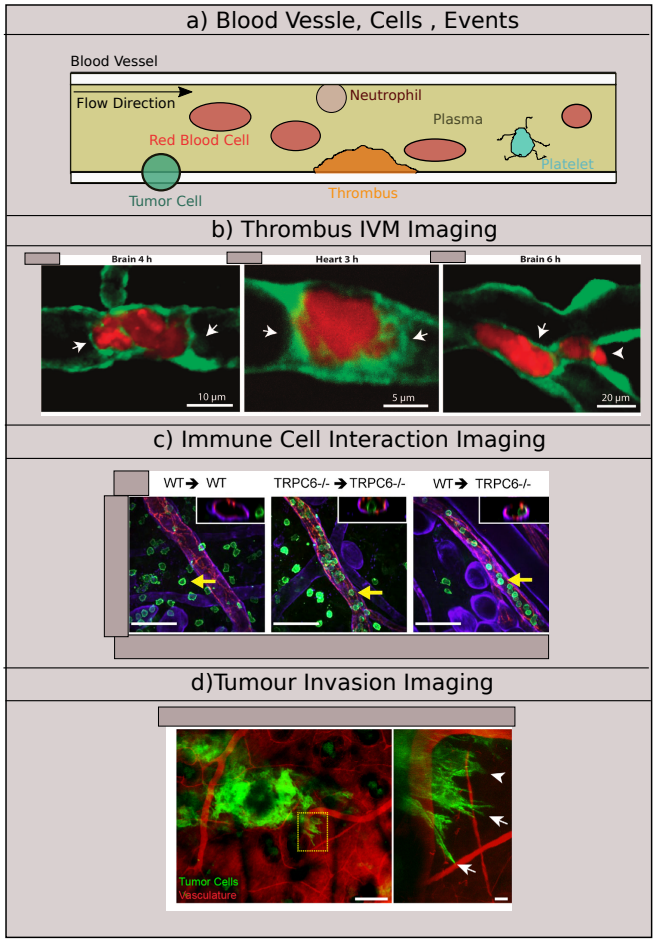

Figure 4-19 Vasculature intravital imaging and corresponding applications. a) Schematic diagram of cells and events in the blood vessel. In which, yellow background denotes plasma, red sphere denotes red blood cell, the green irregular sphere with glitches denote the platelet. Neutrophil and

tumour cell in metastases are drawn on the wall of the blood vessel, where the thrombus is formed as well. b) Thrombus imaging by IVM, with different areas and different imaging duration. c) Immune cell interaction imaging of different animal models. Scale bar, 50 μm. d) Tumour invasion process imaging, blood vessels are getting entangled with tumour tissues. Scale bars in left and right panels are 100 μm and 10 μm respectively. This figure is adapted from [263] [264] and [265] with permissions.

4.4.2 *In vivo* Thrombus Imaging

Thrombus is generated due to the clotting of blood cells and platelets fibrin. It is the final product of the coagulation of blood in haemostasis process. There are two significant components in thrombus, which are the plug formed by the aggregation of red blood cells and platelets, and a cluster of fibrin proteins. The thrombus is a reaction towards injury on the purpose of stopping bleeding. The pathogenesis of thrombus can be generally classified as endothelial (the interior surface of the blood vessel) injury, blood stasis, and hypercoagulability [266]. The two major causes of endothelial injury are trauma and blood hypertension. Blood stasis is the decreasing of blood flow rate, which will trigger the activation of platelets. Hypercoagulability is a disease that makes thrombus happened more than usual, which can be caused by cancer like leukaemia.

The thrombus itself is a healthy response, but it might cause significant harmful results. For example, thrombus could induce stroke disease, which can damage the brain, cause paralysis and death. Due to the complexity and importance in the thrombus formation, the cellular level image resolution and molecule tracking capability have made multiphoton microscope a powerful tool in the investigation of vessels and blood dynamics as well as thrombus metabolism in living bodies.

Photomanipulation based laser ablation has become a reliable method in introducing thrombosis in the vasculature for blood metabolism study. This ablation will remove the endothelial cells in the lining of a blood vessel, and make the subendothelial matrix of thrombotic collagen exposed to the blood fluidics [267]. The benefit of this laser induced ablation is that it can enable a precise activation of local coagulopathy within the interested

region, without introducing excessive plasma extravasation or haemorrhages. In our experiment, we first conducted a laser - mediated injury by switching the laser power with a dynamic FOV reassignment method. Then we changed to high SBP imaging mode (5 x zooming, 20 FPS) at real-time, so as to resolve and quantify the progression of thrombus formation in the microvasculature with smaller pixels. Here the injury area is chosen to be close to the femoral vein of an anaesthetized B6 wild type mouse. Tetramethylrhodamine isothiocyanate (TRITC) - dextran was injected through eye-orbital veins to visualize blood flow within the vasculature and monitor vascular dynamics [268].

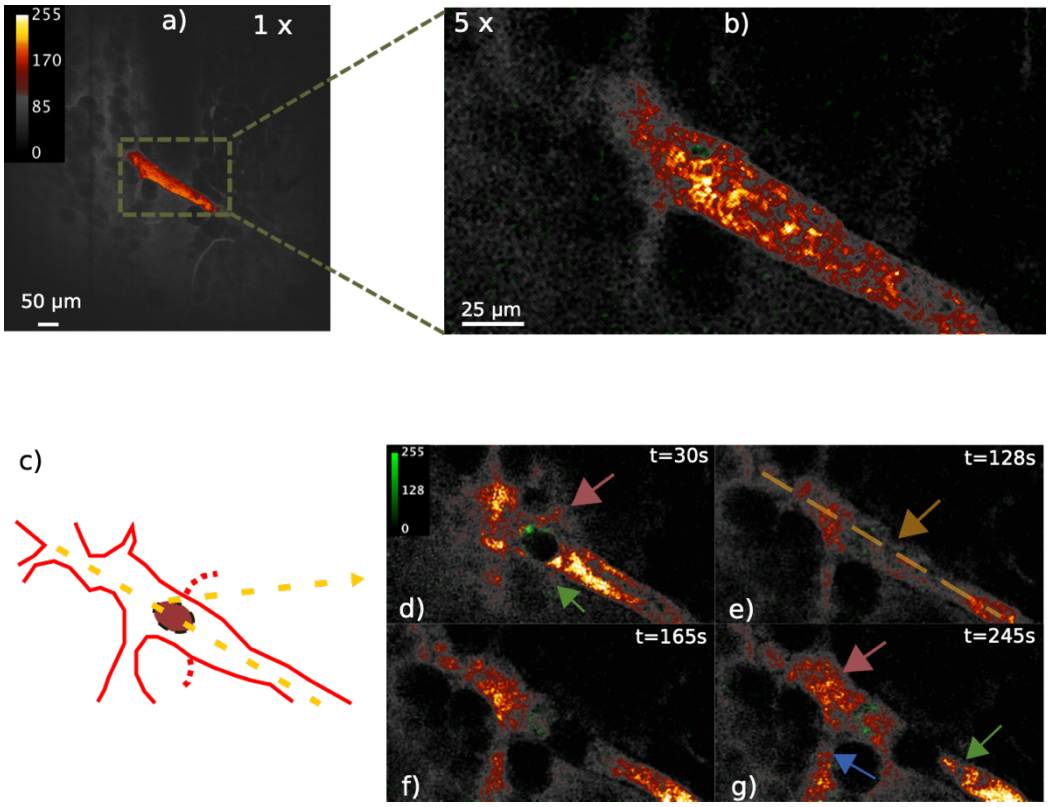

Figure 4-20 Imaging of a thrombus formation in vivo after the laser injury to a C57BL/6 wild - type mouse's blood vessel. Laser power for ablation is 180 mW, total ablation dwelling time is over 27 seconds. Thrombus started formatting in the injury process, and high contrast following embolization process was captured continually. Dextran rhodamine was injected to provide the contrast. The smart colour bar was used to increase visual performance. a) 2 s averaged image with 512 x 512 pixels SBP before surgery (FOV: 500 x 500 μm^2). b) 5 times zoomed high SBP image of a). Pixel size, 0.24 μm, frame rate, 20 FPS, FOV, 226 μm × 123 μm. c) Cartoon plot of the vessel

structure and trunk occlusion. d) to g) are still images captured at different particular time points. The laser injury damaged the vessel wall, and blood pressure was increased by thrombus. The intensity of the image was increased right after the laser ablation, due to the bleeding. The time stamps were chosen corresponding to the different phases in the thrombosis. d) Image of 30 s time point, right after the surgery. e) Image of 128 s, the time when the thrombosis collapsed. f) Image of 165 s, thrombosis formed again without additional laser injury. g) Image of 245 s, blood pressure increased by thrombosis, bleeding started again at the downside. The arrows indicated the bleeding areas. The green signal in these images is coming from the autofluorescence after laser ablation.

The experiment results are shown in Figure 4-20. Figure 4-20 a) is the 2 s averaged still image of surgery area before laser injury. Through the smart colour bar, vessels with high flow count of blood are labelled out from the grey background. b) is a single frame of the optical 5 times zooming image (170 nm pixel) at 20 FPS video-rate speed. c) is the schematic diagram depicting the thrombus process, yellow dashed line denotes the axis of blood vessel, red dashed line indicates the bleeding sites on the boundary of the vascular wall. d) to g) are the selected frames at different time stamps from the video, which allowed us to monitor the evolution of the micro-embolization dynamics. Figure 4-20 d) shows that at time equals 30 s, a thrombotic occlusion occurred, and after expansion and then collapsed (embolizing) at t = 128 seconds in Figure 4-20 e). That site reached a second wave of embolization at t = 165 seconds, without any additional laser injury, Figure 4-20 f). Moreover, after this time point, several local sites of haemorrhage evident happened at positions (i) and (ii), Figure 4-20 g), as indicated by fluorescently stained blood leaking. The time course and dynamics of these imaging results are consistent with platelets activation and collagen exposing. Our image results present the recruiting of new platelets with fibrin, generated from the thrombin and facilitated by the activated platelets, attributing to the wave of embolization [269]. The mechanism of injury is based on the laser thermal effect. The laser induced energy was absorbed by the tissue, which causes tissue damage. In our scenario, the collagen in the matrix is exposed by photothermal effect with a contrast change over the axial direction while doing a volume scanning. Exposure of subendothelial matrix leads to adhesion, activation and aggregation of platelets to the vessel wall. The red fluorescence signal from the outside of the vessel area is indicating the leaking of blood. Therefore, by measuring the fluorescence signal intensity of the adjacent area of the blood vessel, the increasing of leaking blood indicated the blood pressure is increased.

In summary, polygon based photomanipulation microscope is achieved, and both *in vitro* and *in vivo* photomanipulation experiments are conducted. Now, this setup is become a comprehensive multi-mode platform, with the extended function of rapid volumetric imaging and photomanipulation. Together with the previously developed AO function, a volumetric AO polygon laser scanning microscope has been built up, through the engineering of laser beam's position, phase, amplitude and wavelength, in together with state of the art controlling hardware and software, we achieved the flexibilities in temporal resolution, spatial resolution, imaging depth, and phototoxicity.

4.5 Contributions

Woei Ming Lee supervised the developing of photomanipulation functionality. Yujie Zheng provided the 3 μm beads for volumetric imaging. Michael Castanares and Vincent Daria provided the FITC sample for FRAP. Xuefei He assisted in the preparation of the GUV sample. Samantha Montague and Elizabeth Gardiner provided the *in vitro* platelets sample and assisted in the *in vivo* thrombus experiment.

Chapter 5 Conclusions and Future Works

This chapter serves as the conclusion and future work discussion chapter. I will first make a summary of the achieved results, including the discussion of both advantages and disadvantages in the volumetric AO polygon microscope. Furthermore, planned works for the future will be introduced, consisting of both technological development and biological experiment design.

5.1 Summary

In summary, a flexible laser scanning multiphoton microscope based on the polygon mirror has been presented in this thesis. In this multiphoton microscope, it has achieved flexibilities in imaging speed, SBP, imaging FOV as well as photomanipulation functionality. This polygon microscope has a volumetric imaging area of 450 x 450 x 80 μm, with a volume scanning speed of 1 to 10 VPS, and up to 100 MB SBP per frame. The RAO function enabled aberration correction over the whole FOV either in deep depth and on the surface of the tissue. Moreover, RAO extended the FOV over 2 times to break the constraints of lens size in the optical train. All these functions have been integrated into a customized control software PScan, with extendibility and easy access graphic control interface, for practical deployment.

A series of imaging tests and *in vivo* experiments have been conducted. The measurements of neuron action potentials, blood dynamics, and thrombus metabolism have been demonstrated. In all, a flexible polygon based laser scanning intravital microscope platform, with large FOV AO correction capability, photomanipulation functionality, and fast volumetric imaging ability had been achieved and the design detail had been shown in this thesis.

5.2 PScan 2.0

To further develop and exploit this platform, a series of future works are scheduled, including both technological upgrade and biological experiment design. First, PScan 2.0 is under development, with the utilisation of GPU and advanced computational toolboxes, for building a smart microscope, with automatic imaging and analysis ability. Machine learning technique will be implemented for achieving functional modules like optical, cell detection and tracking, even self-investigating function. The proposed schematic of PScan 2.0 has been shown in Figure 5-1.

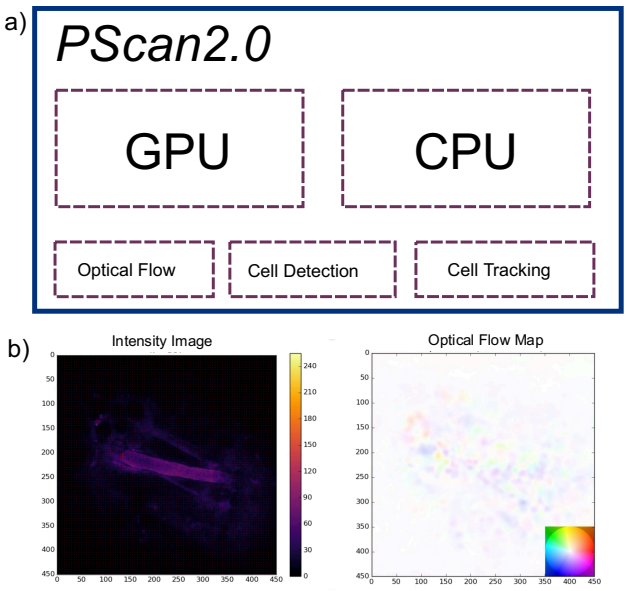

Figure 5-1 Schematic of PScan 2.0. PScan 2.0 will utilise both GPU and CPU for parallel high-speed real-time processing. More advanced function modules are developed, such as optical flow to detect the flow speed, automatic cell detection and cell tracking for biological studies. b) Measurement of blood flowing speed and direction by optical flow [270].

Also, open-source PScan software might be helpful to the community. However, it is not clear how helpful customised hardware control software will be. In order to make a public version PScan, revising and editing of both the code and the relevant document will be required.

5.3 3D RAO

Another technological improvement is achieving rapid three-dimensional RAO correction. The proposed method is shown Figure 5-2. A fast DM will be used, with each frame in sequence, a unitary defocus aberration mask will be applied, for the purpose of axial scanning. While in addition to the defocus aberration, RAO will be added to correct the aberration in each frame. The defocus aberration mask will maintain the same in the single frame, but in combined with different RAO patterns for corrections. Ideally, this will give a volumetric RAO correction, with the ability to work over the whole imaging volume.

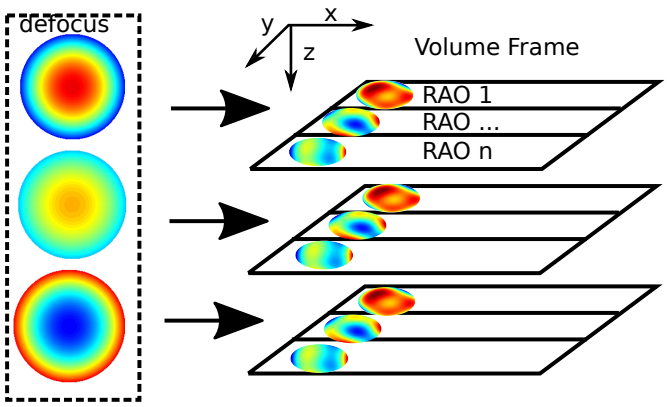

Figure 5-2 Volumetric RAO Correction. A combination of RAO and defocus volumetrically scanning method. A volumetric defocus aberration (Z5) is applied together with the RAO correction. For every single frame, one constant defocus coefficient with several line correction mask it added together to achieve the video-rate volume scanning.

Besides, the RAO correction area can be further symmetric by replacing the current 36 facets polygon (Lincoln Laser, US) to a new polygon with smaller facets. So that the horizontal scanning area will be optically sectioned corresponding to the number of facets. For instance, with 72 facets, the imaging area will be half the size of the current FOV for each frame in terms of width. However, the line scanning rate is increased proportionally to the number of facets. Therefore, through driving the horizontal direction GM mirror, the imaging FOV can still be the same by stitching 2 frames together without losing any temporal resolution. The wavefront

retrieving accuracy can be further increased through using the high contrast high SBP image instead of the 512 x 512 pixels frame [101].

5.4 3D FRAP

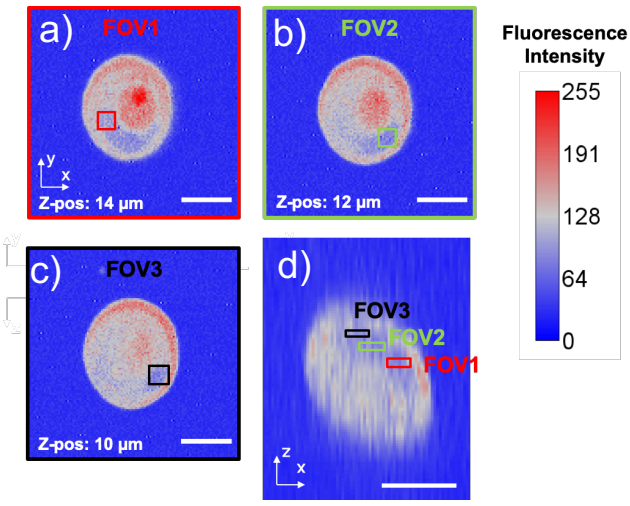

Figure 5-3 Fast volumetric imaging of FRAP on GUV. a) The lateral image GUV after photobleaching at 14 μm depth. b) Lateral image of same GUV at 12 μm depth. c) Lateral image of same GUV at 10 μm. d) Axial image of GUV after photobleaching, obtained from a), b) and c) by DM based fast volumetric imaging. The corresponding areas of lateral FOV 1 to 3 are labelled. Scale Bar: 25 μm.

Rapid volumetric visualizing of molecular and cell dynamics is still challenging in biology. Now with this volumetric laser scanning microscope and its dual functions of imaging and photomanipulation, photomanipulation studies can be extended from 2D to 3D. For example, volumetric imaging of GUV after FRAP is shown in Figure 5-3 [271]. In which, the imaging speed is 1 VPS. Axial imaging size is 34 μm, 2 μm for each step. The fluorescence signal from the bleached region is lower than the other areas. This experiment was conducted under the same process of previous GUV FRAP but followed with 3D imaging.

5.5 *In vivo* Volumetric Platelets Imaging

On the other side, we will further investigate the dynamic process of multisite thrombus in 3D. The proposed experiment schematic process is shown in Figure 5-4, in which three injury sites are induced, and the blood flow and interactions among the injuries will be imaged in 3D. In the future, photoconversion dyes will be used to label the platelets for tracking and further analysis.

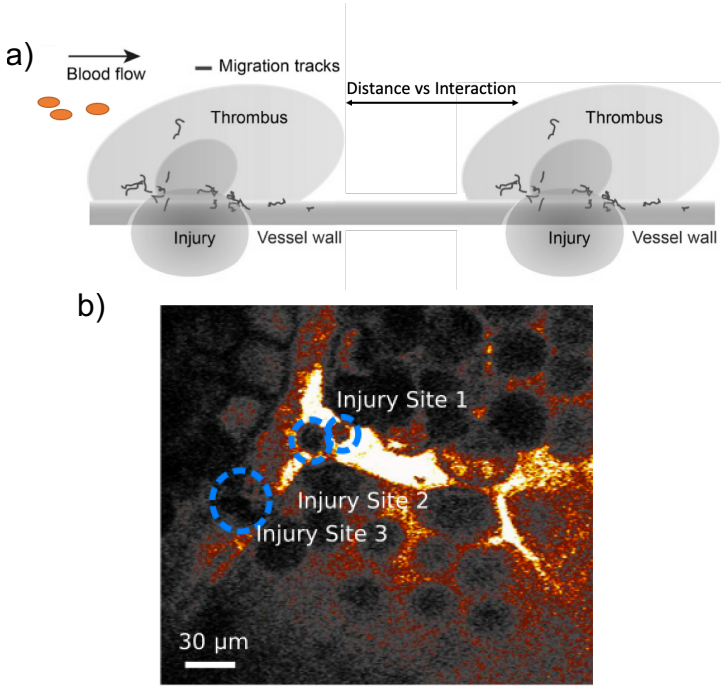

Figure 5-4 Multisite injuries of the blood vessel by laser ablation. a) Schematic diagram of multisite injuries in the blood vessel wall. This figure is being Adapted from [272] with permission requested. b) In vivo multisite injuries experiment, in which three thrombi are introduced at the connections joint between two vessels. The experiment was conducted onto the B6 wild type mouse.

Another potential application is imaging on the microfluidic chip. As shown in Figure 4-4, in which we used the microfluidic channel to mimic the flow of blood, and the platelets were injected into the channel, attached with collagen substrate. With the enhanced speed and spatial resolution, the dynamical functioning platelets will be studied.

5.6 Contributions

Juan David Adarve wrote the optical flow algorithm and assisted in the measuring of blood flow speed. Daniel Lim conducted the 3D GUV FRAP experiment and processed the data.

References

1. König, K., *Multiphoton microscopy in life sciences*. Journal of Microscopy, 2000. **200**(2): p. 83-104.
2. Gest, H., *The discovery of microorganisms by Robert Hooke and Antoni Van Leeuwenhoek, fellows of the Royal Society*. Notes and records of the Royal Society of London, 2004. **58**(2): p. 187-201.
3. Franklin, R.E. and R.G. Gosling, *Molecular configuration in sodium thymonucleate*. Nature, 1953. **171**(4356): p. 740.
4. Liu, Y., et al., *Near-atomic cryo-EM imaging of a small protein displayed on a designed scaffolding system*. Proceedings of the National Academy of Sciences, 2018. **115**(13): p. 3362-3367.
5. Schermelleh, L., et al., *Super-resolution microscopy demystified*. Nature Cell Biology, 2019. **21**(1): p. 72-84.
6. Williams, D.B. and C.B. Carter, *The transmission electron microscope*, in *Transmission electron microscopy*. 1996, Springer. p. 3-17.
7. Chugani, H.T., M.E. Phelps, and J.C. Mazziotta, *Positron emission tomography study of human brain functional development*. Annals of neurology, 1987. **22**(4): p. 487-497.
8. Weigert, R., et al., *Intravital microscopy: a novel tool to study cell biology in living animals*. Histochemistry and cell biology, 2010. **133**(5): p. 481-491.
9. Betzig, E., et al., *Imaging intracellular fluorescent proteins at nanometer resolution*. Science, 2006. **313**(5793): p. 1642-5.
10. Rust, M.J., M. Bates, and X. Zhuang, *Sub-diffraction-limit imaging by stochastic optical reconstruction microscopy (STORM)*. Nature methods, 2006. **3**(10): p. 793.
11. Hell, S.W. and J. Wichmann, *Breaking the diffraction resolution limit by stimulated emission: stimulated-emission-depletion fluorescence microscopy*. Optics Letters, 1994. **19**(11): p. 780-782.
12. Fernandez-Suarez, M. and A.Y. Ting, *Fluorescent probes for super-resolution imaging in living cells*. Nat Rev Mol Cell Biol, 2008. **9**(12): p. 929-43.
13. Yang, F., L.G. Moss, and G.N. Phillips, *The molecular structure of green fluorescent protein*. Nature Biotechnology, 1996. **14**(10): p. 1246-1251.
14. Münter, S., *Super-Resolution Microscopy*. 2017.

15. Davidovits, P. and M.D. Egger, *Scanning Laser Microscope*. Nature, 1969. **223**(5208): p. 831-831.

16. Ohara-Imaizumi, M., et al., *TIRF imaging of docking and fusion of single insulin granule motion in primary rat pancreatic beta-cells: different behaviour of granule motion between normal and Goto-Kakizaki diabetic rat beta-cells*. The Biochemical journal, 2004. **381**(Pt 1): p. 13-18.

17. Nobis, M., et al., *Molecular mobility and activity in an intravital imaging setting - implications for cancer progression and targeting*. J Cell Sci, 2018. **131**(5).

18. Holtmaat, A., et al., *Long-term, high-resolution imaging in the mouse neocortex through a chronic cranial window*. Nature Protocols, 2009. **4**: p. 1128.

19. Masch, J.-M., et al., *Robust nanoscopy of a synaptic protein in living mice by organic-fluorophore labeling*. Proceedings of the National Academy of Sciences, 2018. **115**(34): p. E8047-E8056.

20. Zernike, F., *How I discovered phase contrast*. Science, 1955. **121**(3141): p. 345-349.

21. Allen, R.D., N.S. Allen, and J.L. Travis, *Video - enhanced contrast, differential interference contrast (AVEC - DIC) microscopy: A new method capable of analyzing microtubule - related motility in the reticulopodial network of Allogromia laticollaris*. Cell motility, 1981. **1**(3): p. 291-302.

22. Hoffman, R. and L. Gross, *Modulation contrast microscope*. Applied Optics, 1975. **14**(5): p. 1169-1176.

23. Renz, M., *Fluorescence microscopy-a historical and technical perspective*. Cytometry A, 2013. **83**(9): p. 767-79.

24. ELLINGER, P., *FLUORESCENCE MICROSCOPY IN BIOLOGY*. Biological Reviews, 1940. **15**(3): p. 323-347.

25. Schäferling, M., *The art of fluorescence imaging with chemical sensors*. Angewandte Chemie International Edition, 2012. **51**(15): p. 3532-3554.

26. Cheng, A., et al., *Simultaneous two-photon calcium imaging at different depths with spatiotemporal multiplexing*. Nature Methods, 2011. **8**: p. 139.

27. Shaner, N.C., P.A. Steinbach, and R.Y. Tsien, *A guide to choosing fluorescent proteins*. Nat Methods, 2005. **2**(12): p. 905-9.

28. Specht, E.A., E. Braselmann, and A.E. Palmer, *A Critical and Comparative Review of Fluorescent Tools for Live-Cell Imaging*. Annual Review of Physiology, 2017. **79**(1): p. 93-117.

29. Ntziachristos, V., *FLUORESCENCE MOLECULAR IMAGING*. Annual Review of Biomedical Engineering, 2006. **8**(1): p. 1-33.

30. Suzuki, T., et al., *Recent advances in fluorescent labeling techniques for fluorescence microscopy*. Acta histochemica et cytochemica, 2007. **40**(5): p. 131-137.

31. Lichtman, J.W. and J.-A. Conchello, *Fluorescence microscopy*. Nature Methods, 2005. **2**: p. 910.

32. Jablonski, A., *Efficiency of anti-Stokes fluorescence in dyes*. Nature, 1933. **131**(3319): p. 839.

33. Kapuscinski, J., *DAPI: a DNA-specific fluorescent probe*. Biotechnic & Histochemistry, 1995. **70**(5): p. 220-233.

34. Collins, H.A., et al., *Blood-vessel closure using photosensitizers engineered for two-photon excitation*. Nature Photonics, 2008. **2**(7): p. 420.

35. Kherlopian, A.R., et al., *A review of imaging techniques for systems biology*. BMC Syst Biol, 2008. **2**: p. 74.

36. Bera, D., et al., *Quantum Dots and Their Multimodal Applications: A Review*. Materials, 2010. **3**(4): p. 2260-2345.

37. Michalet, X., et al., *Quantum Dots for Live Cells, in Vivo Imaging, and Diagnostics*. Science (New York, N.Y.), 2005. **307**(5709): p. 538-544.

38. Tsien, R.Y., *The Green Fluorescent Protein*. Annual Review of Biochemistry, 1998. **67**(1): p. 509-544.

39. Prasher, D.C., et al., *Primary structure of the Aequorea victoria green-fluorescent protein*. Gene, 1992. **111**(2): p. 229-233.

40. Zimmer, M., *Green Fluorescent Protein (GFP): Applications, Structure, and Related Photophysical Behavior*. Chemical Reviews, 2002. **102**(3): p. 759-782.

41. Fan, G.Y., et al., *Video-Rate Scanning Two-Photon Excitation Fluorescence Microscopy and Ratio Imaging with Cameleons*. Biophysical Journal, 1999. **76**(5): p. 2412-2420.

42. Tsien, R.Y., *Nobel lecture: constructing and exploiting the fluorescent protein paintbox*. Integrative Biology, 2010. **2**(2-3): p. 77-93.

43. Akerboom, J., et al., *Optimization of a GCaMP calcium indicator for neural activity imaging*. The Journal of neuroscience : the official journal of the Society for Neuroscience, 2012. **32**(40): p. 13819-13840.

44. Cheng, H., W. Lederer, and M. Cannell, *Calcium sparks: elementary events underlying excitation-contraction coupling in heart muscle*. Science, 1993. **262**(5134): p. 740-744.

45. Cho, A., N. Haruyama, and A.B. Kulkarni, *Generation of transgenic mice*. Current protocols in cell biology, 2009. **Chapter 19**: p. Unit-19.11.

46. Vennin, C., et al., *Transient tissue priming via ROCK inhibition uncouples pancreatic cancer progression, sensitivity to chemotherapy, and metastasis*. Science translational medicine, 2017. **9**(384): p. eaai8504.

47. Nimmerjahn, A., *Advances in Two-Photon Fluorescence Microscopy for high-resolution Anatomical and Functional Imaging of cell populations in the intact brain*. 2005.

48. Osswald, M. and F. Winkler, *Insights into cell-to-cell and cell-to-blood-vessel communications in the brain: in vivo multiphoton microscopy*. Cell and tissue research, 2013. **352**(1): p. 149-159.

49. Axelrod, D., *Total Internal Reflection Fluorescence Microscopy in Cell Biology*. Traffic, 2001. **2**(11): p. 764-774.

50. Li, D., et al., *ADVANCED IMAGING. Extended-resolution structured illumination imaging of endocytic and cytoskeletal dynamics*. Science, 2015. **349**(6251): p. aab3500.

51. Huisken, J., et al., *Optical sectioning deep inside live embryos by selective plane illumination microscopy*. Science, 2004. **305**(5686): p. 1007-1009.

52. Bouchard, M.B., et al., *Swept confocally-aligned planar excitation (SCAPE) microscopy for high speed volumetric imaging of behaving organisms*. Nat Photonics, 2015. **9**(2): p. 113-119.

53. Chen, B.C., et al., *Lattice light-sheet microscopy: imaging molecules to embryos at high spatiotemporal resolution*. Science, 2014. **346**(6208): p. 1257998.

54. Follain, G., et al., *Seeing is believing - multi-scale spatio-temporal imaging towards in vivo cell biology*. J Cell Sci, 2017. **130**(1): p. 23-38.

55. S, U., *How to Draw a Mouse*. Available at: http://how2drawanimals.com/8-animals/17-draw-mouse.html, 2019.

56. Carvalho, J., *Welcome to CRISPR fly design!* available at: https://www.crisprflydesign.org/, 2019.

57. Reynaud, E.G., et al., *Guide to light-sheet microscopy for adventurous biologists*. Nature Methods, 2014. **12**: p. 30.

58. MINSKY, M., *Microscopy apparatus*. 1961, US Patent 3,013,467.

59. Minsky, M., *Memoir on inventing the confocal scanning microscope*. Scanning, 1988. **10**(4): p. 128-138.

60. Denk, W., J.H. Strickler, and W.W. Webb, *Two-photon laser scanning microscopy*. Science, 1990. **248**.

61. Grzybowski, A. and K. Pietrzak, *Maria Goeppert-Mayer (1906–1972): Two-photon effect on dermatology*. Clinics in Dermatology, 2013. **31**(2): p. 221-225.

62. Diaspro, A., G. Chirico, and M. Collini, *Two-photon fluorescence excitation and related techniques in biological microscopy*. Quarterly reviews of biophysics, 2005. **38**(2): p. 97-166.

63. Masters, B.R. and P.T.C. So, *Antecedents of two-photon excitation laser scanning microscopy*. Microscopy Research and Technique, 2004. **63**(1): p. 3-11.

64. Denk, W., J.H. Strickler, and W.W. Webb, *Two-photon laser scanning fluorescence microscopy*. Science, 1990. **248**(4951): p. 73-76.

65. Horton, N.G., et al., *In vivo three-photon microscopy of subcortical structures within an intact mouse brain*. Nature Photonics, 2013. **7**: p. 205.

66. Bloembergen, N., et al., *Optical second-harmonic generation in reflection from media with inversion symmetry*. Physical Review, 1968. **174**(3): p. 813.

67. Zipfel, W.R., et al., *Live tissue intrinsic emission microscopy using multiphoton-excited native fluorescence and second harmonic generation*. Proceedings of the National Academy of Sciences, 2003. **100**(12): p. 7075-7080.

68. Xu, C. and W. Webb, *Measurement of two-photon excitation cross sections of molecular fluorophores with data from 690 to 1050 nm*. Vol. 13. 1996. 481-491.

69. Helmchen, F. and W. Denk, *Deep tissue two-photon microscopy*. Nature Methods, 2005. **2**(12): p. 932-940.

70. Zipfel, W.R., R.M. Williams, and W.W. Webb, *Nonlinear magic: multiphoton microscopy in the biosciences*. Nature Biotechnology, 2003. **21**(11): p. 1369-1377.

71. Benaron, D.A., W.-F. Cheong, and D.K. Stevenson, *Tissue optics*. Science, 1997. **276**(5321): p. 2002-2003.

72. Badon, A., et al., *Smart optical coherence tomography for ultra-deep imaging through highly scattering media*. Science Advances, 2016. **2**(11): p. e1600370.

73. Fujimoto, J.G., et al., *Optical Coherence Tomography: An Emerging Technology for Biomedical Imaging and Optical Biopsy*. Neoplasia (New York, N.Y.), 2000. **2**(1-2): p. 9-25.

74. Milstein, A.B., et al., *Fluorescence optical diffusion tomography*. Applied Optics, 2003. **42**(16): p. 3081-3094.

75. Max, C. *Introduction to adaptive optics and its history*. in *American Astronomical Society 197th Meeting*. 2001. NSF Center for Adaptive Optics University of California at Santa Cruz and ….

76. Prahl, S.A., *A Monte Carlo model of light propagation in tissue*. Institutes for Advanced Optical Technologies. Vol. 10305. 1989: SPIE.

77. Mainster, M.A., *Wavelength selection in macular photocoagulation: tissue optics, thermal effects, and laser systems*. Ophthalmology, 1986. **93**(7): p. 952-958.

78. Tuchin, V.V. and V. Tuchin, *Tissue optics: light scattering methods and instruments for medical diagnosis*. 2007.

79. Tuchin, V.V., *Tissue optics and photonics: light-tissue interaction*. Journal of Biomedical Photonics & Engineering, 2015. **1**(2).

80. Wang, L.V. and S. Hu, *Photoacoustic Tomography: In Vivo Imaging from Organelles to Organs*. Science, 2012. **335**(6075): p. 1458-1462.

81. Mourant, J.R., et al., *Predictions and measurements of scattering and absorption over broad wavelength ranges in tissue phantoms*. Applied optics, 1997. **36**(4): p. 949-957.

82. Reddy, G.K., L. Stehno-Bittel, and C.S. Enwemeka, *Laser photostimulation accelerates wound healing in diabetic rats*. Wound Repair and Regeneration, 2001. **9**(3): p. 248-255.

83. Tuchin, V.V., S.R. Utz, and I.V. Yaroslavsky, *Tissue optics, light distribution, and spectroscopy*. Optical Engineering, 1994. **33**(10): p. 3178-3189.

84. Vo-Dinh, T., *Biomedical Photonics Handbook, 3 Volume Set*. 2014: CRC press.

85. Kobat, D., N.G. Horton, and C. Xu, *In vivo two-photon microscopy to 1.6-mm depth in mouse cortex*. Journal of biomedical optics, 2011. **16**(10): p. 106014.

86. Steelman, Z.A., et al., *Light-scattering methods for tissue diagnosis*. Optica, 2019. **6**(4): p. 479-489.

87. Rodriguez, L.G., S.J. Lockett, and G.R. Holtom, *Coherent anti - stokes Raman scattering microscopy: A biological review*. Cytometry Part A: The Journal of the International Society for Analytical Cytology, 2006. **69**(8): p. 779-791.

88. Kneipp, K., et al., *Single molecule detection using surface-enhanced Raman scattering (SERS)*. Physical review letters, 1997. **78**(9): p. 1667.

89. Lockwood, D.J., *Rayleigh and Mie Scattering*. 2015: p. 1-12.

90. Miles, R.B., W.R. Lempert, and J.N. Forkey, *Laser rayleigh scattering*. Measurement Science and Technology, 2001. **12**(5): p. R33.

91. Bhattacharjee, S., *DLS and zeta potential - What they are and what they are not?* J Control Release, 2016. **235**: p. 337-351.

92. Theer, P. and W. Denk, *On the fundamental imaging-depth limit in two-photon microscopy*. JOSA A, 2006. **23**(12): p. 3139-3149.

93. Horton, N.G., et al., *In vivo three-photon microscopy of subcortical structures within an intact mouse brain*. Nature photonics, 2013. **7**(3): p. 205.

94. Marx, V., *Microscopy: hello, adaptive optics*. Nat Methods, 2017. **14**(12): p. 1133-1136.

95. Brabec, T., et al., *Kerr lens mode locking*. Optics letters, 1992. **17**(18): p. 1292-1294.

96. Fork, R., B. Greene, and C.V. Shank, *Generation of optical pulses shorter than 0.1 psec by colliding pulse mode locking*. Applied Physics Letters, 1981. **38**(9): p. 671-672.

97. Hofer, R., et al., *Modelocking of a Nd-fiber laser at 920 nm*. Optics communications, 1997. **140**(4-6): p. 242-244.

98. Spence, D.E., P.N. Kean, and W. Sibbett, *60-fsec pulse generation from a self-mode-locked Ti:sapphire laser*. Optics Letters, 1991. **16**(1): p. 42-44.

99. Fork, R., O. Martinez, and J. Gordon, *Negative dispersion using pairs of prisms*. Optics letters, 1984. **9**(5): p. 150-152.

100. Römer, G.R.B.E. and P. Bechtold, *Electro-optic and Acousto-optic Laser Beam Scanners*. Physics Procedia, 2014. **56**: p. 29-39.

101. Li, Y., et al., *High contrast imaging and flexible photomanipulation for quantitative in vivo multiphoton imaging with polygon scanning microscope*. Journal of biophotonics, 2018. **11**(7): p. e201700341.

102. Young, M.D., et al., *A pragmatic guide to multiphoton microscope design*. Advances in optics and photonics, 2015. **7**(2): p. 276-378.

103. Haderka, O., M. Hamar, and J. Peřina Jr, *Experimental multi-photon-resolving detector using a single avalanche photodiode*. The European Physical Journal D-Atomic, Molecular, Optical and Plasma Physics, 2004. **28**(1): p. 149-154.

104. Castanares, M.L., et al., *Efficient multi-site two-photon functional imaging of neuronal circuits*. Biomedical Optics Express, 2016. **7**(12): p. 5325-5334.

105. Roth, J.M., T. Murphy, and C. Xu, *Ultrasensitive and high-dynamic-range two-photon absorption in a GaAs photomultiplier tube*. Optics letters, 2002. **27**(23): p. 2076-2078.

106. *Confocal Microscopy - Introduction | Olympus Life Science*.

107. *A miniature head-mounted two-photon microscope: high-resolution brain imaging in freely moving animals*. Neuron, 2001. **31**: p. 903.

108. Zong, W., et al., *Fast high-resolution miniature two-photon microscopy for brain imaging in freely behaving mice*. Nat Methods, 2017. **14**(7): p. 713-719.

109. Helmchen, F., et al., *A miniature head-mounted two-photon microscope: high-resolution brain imaging in freely moving animals*. Neuron, 2001. **31**(6): p. 903-912.

110. Sofroniew, N.J., et al., *A large field of view two-photon mesoscope with subcellular resolution for in vivo imaging*. Elife, 2016. **5**.

111. Rodríguez, C., et al., *Three-photon fluorescence microscopy with an axially elongated Bessel focus*. Optics Letters, 2018. **43**(8): p. 1914-1917.

112. Booth, M.J., *Adaptive optics in microscopy*. Philos Trans A Math Phys Eng Sci, 2007. **365**(1861): p. 2829-43.

113. Liu, Z., L.D. Lavis, and E. Betzig, *Imaging live-cell dynamics and structure at the single-molecule level*. Mol Cell, 2015. **58**(4): p. 644-59.

114. Mertz, J., C. Xu, and W. Webb, *Single-molecule detection by two-photon-excited fluorescence*. Optics letters, 1995. **20**(24): p. 2532-2534.

115. Bewersdorf, J., R. Pick, and S.W. Hell, *Multifocal multiphoton microscopy*. Optics Letters, 1998. **23**(9): p. 655-657.

116. Nguyen, Q.T., et al., *Construction of a two-photon microscope for video-rate Ca2+ imaging*. Cell Calcium, 2001. **30**(6): p. 383-393.

117. Salomé, R., et al., *Ultrafast random-access scanning in two-photon microscopy using acousto-optic deflectors*. Journal of Neuroscience Methods, 2006. **154**(1): p. 161-174.

118. Go, M.A., et al., *Simultaneous multi‐site two‐photon photostimulation in three dimensions*. Journal of biophotonics, 2012. **5**(10): p. 745-753.

119. Nikolenko, V., et al., *SLM microscopy: scanless two-photon imaging and photostimulation using spatial light modulators*. Frontiers in neural circuits, 2008. **2**: p. 5.

120. Lillis, K.P., et al., *Two-photon imaging of spatially extended neuronal network dynamics with high temporal resolution*. Journal of Neuroscience Methods, 2008. **172**(2): p. 178-184.

121. Theriault, G., et al., *Extended two-photon microscopy in live samples with Bessel beams: steadier focus, faster volume scans, and simpler stereoscopic imaging*. Front Cell Neurosci, 2014. **8**: p. 139.

122. Chen, B., et al., *Rapid volumetric imaging with Bessel-Beam three-photon microscopy*. Biomedical optics express, 2018. **9**(4): p. 1992-2000.

123. Duemani Reddy, G., et al., *Three-dimensional random access multiphoton microscopy for functional imaging of neuronal activity*. Nat Neurosci, 2008. **11**(6): p. 713-20.

124. Nadella, K.M.N.S., et al., *Random-access scanning microscopy for 3D imaging in awake behaving animals*. Nature Methods, 2016. **13**: p. 1001.

125. Grewe, B.F., et al., *High-speed in vivo calcium imaging reveals neuronal network activity with near-millisecond precision*. Nat Methods, 2010. **7**(5): p. 399-405.

126. Iyer, V., T.M. Hoogland, and P. Saggau, *Fast functional imaging of single neurons using random-access multiphoton (RAMP) microscopy*. Journal of neurophysiology, 2006. **95**(1): p. 535-545.

127. Otsu, Y., et al., *Optical monitoring of neuronal activity at high frame rate with a digital random-access multiphoton (RAMP) microscope*. Journal of neuroscience methods, 2008. **173**(2): p. 259-270.

128. Amir, W., et al., *Simultaneous imaging of multiple focal planes using a two-photon scanning microscope*. Optics Letters, 2007. **32**(12): p. 1731-1733.

129. Stirman, J.N., et al., *Wide field-of-view, multi-region, two-photon imaging of neuronal activity in the mammalian brain*. Nat Biotechnol, 2016. **34**(8): p. 857-62.

130. Weisenburger, S., et al., *Volumetric Ca2+ Imaging in the Mouse Brain Using Hybrid Multiplexed Sculpted Light Microscopy*. Cell, 2019. **177**(4): p. 1050-1066.e14.

131. Wilt, B.A., et al., *Advances in Light Microscopy for Neuroscience*. Annual Review of Neuroscience, 2009. **32**(1): p. 435-506.

132. Yang, W., et al., *Simultaneous Multi-plane Imaging of Neural Circuits*. Neuron, 2016. **89**(2): p. 269-284.

133. Ducros, M., et al., *Encoded multisite two-photon microscopy*. Proceedings of the National Academy of Sciences, 2013. **110**(32): p. 13138-13143.

134. Lutz, C., et al., *Holographic photolysis of caged neurotransmitters*. Nature Methods, 2008. **5**: p. 821.

135. Gabor, D., *A New Microscopic Principle*. Nature, 1948. **161**(4098): p. 777-778.

136. Fienup, J.R., *Phase retrieval algorithms: a comparison*. Applied Optics, 1982. **21**(15): p. 2758-2769.

137. Pégard, N.C., et al., *Three-dimensional scanless holographic optogenetics with temporal focusing (3D-SHOT)*. Nature Communications, 2017. **8**(1): p. 1228.

138. Nielsen, T., et al., *High efficiency beam splitter for multifocal multiphoton microscopy*. Journal of microscopy, 2001. **201**(3): p. 368-376.

139. Ji, N., J. Freeman, and S.L. Smith, *Technologies for imaging neural activity in large volumes*. Nature Neuroscience, 2016. **19**: p. 1154.

140. Zhu, G., et al., *Simultaneous spatial and temporal focusing of femtosecond pulses*. Optics Express, 2005. **13**(6): p. 2153-2159.

141. Oron, D., E. Tal, and Y. Silberberg, *Scanningless depth-resolved microscopy*. Optics Express, 2005. **13**(5): p. 1468-1476.

142. Žurauskas, M., et al., *Rapid adaptive remote focusing microscope for sensing of volumetric neural activity*. Biomedical Optics Express, 2017. **8**(10): p. 4369-4379.

143. Lu, R., et al., *Video-rate volumetric functional imaging of the brain at synaptic resolution*. Nature Neuroscience, 2017. **20**: p. 620.

144. Shain, W.J., et al., *Extended depth-of-field microscopy with a high-speed deformable mirror*. Optics Letters, 2017. **42**(5): p. 995-998.

145. Grewe, B.F., et al., *Fast two-layer two-photon imaging of neuronal cell populations using an electrically tunable lens*. Biomedical Optics Express, 2011. **2**(7): p. 2035-2046.

146. Thériault, G., et al., *Extended two-photon microscopy in live samples with Bessel beams: steadier focus, faster volume scans, and simpler stereoscopic imaging*. Frontiers in cellular neuroscience, 2014. **8**: p. 139-139.

147. Rosenegger, D.G., et al., *A High Performance, Cost-Effective, Open-Source Microscope for Scanning Two-Photon Microscopy that Is Modular and Readily Adaptable*. PLOS ONE, 2014. **9**(10): p. e110475.

148. Choi, S., et al., *Development of a high speed laser scanning confocal microscope with an acquisition rate up to 200 frames per second*. Optics express, 2013. **21**(20): p. 23611-23618.

149. Kim, K.H., C. Buehler, and P.T. So, *High-speed, two-photon scanning microscope*. Applied Optics, 1999. **38**(28): p. 6004-6009.

150. Veilleux, I., et al., *In vivo cell tracking with video rate multimodality laser scanning microscopy*. IEEE Journal of selected topics in quantum electronics, 2008. **14**(1): p. 10-18.

151. Webb, R.H., G.W. Hughes, and F.C. Delori, *Confocal scanning laser ophthalmoscope*. Applied Optics, 1987. **26**(8): p. 1492-1499.

152. Bumstead, J.R., et al., *Designing a large field-of-view two-photon microscope using optical invariant analysis*. Neurophotonics, 2018. **5**(2): p. 025001.

153. Artoni, P., et al., *Arduino Due based tool to facilitate in vivo two-photon excitation microscopy*. Biomedical optics express, 2016. **7**(4): p. 1604-1613.

154. *A call for bioimaging software usability*. Nat. Methods, 2012. **9**: p. 666.

155. Eliceiri, K.W., et al., *Biological imaging software tools*. Nature Methods, 2012. **9**: p. 697.

156. Liu, T.-L., et al., *Observing the cell in its native state: Imaging subcellular dynamics in multicellular organisms*. Science, 2018. **360**(6386).

157. *MOSAIC | Microscopy | Ashburn, VA, USA | Advanced Imaging Center*.

158. Ruan, H., et al., *Deep tissue optical focusing and optogenetic modulation with time-reversed ultrasonically encoded light*. Science Advances, 2017. **3**(12).

159. Chi, K.R., *Imaging and detection: focusing on software*. Nature Methods, 2008. **5**: p. 651.

160. Nguyen, Q.-T., P.S. Tsai, and D. Kleinfeld, *MPScope: A versatile software suite for multiphoton microscopy*. Journal of Neuroscience Methods, 2006. **156**(1): p. 351-359.

161. *HelioScan: a software framework for controlling in vivo microscopy setups with high hardware flexibility, functional diversity and extendibility*. J. Neurosci. Methods, 2013. **215**: p. 38.

162. Pologruto, T.A., B.L. Sabatini, and K. Svoboda, *ScanImage: Flexible software for operating laser scanning microscopes*. BioMedical Engineering OnLine, 2003. **2**(1): p. 13.

163. Edelstein, A.D., et al., *Advanced methods of microscope control using μManager software*. Journal of Biological Methods; Vol 1, No 2 (2014), 2014.

164. Edelstein, A., et al., *Computer control of microscopes using μManager*. Current protocols in molecular biology, 2010. **Chapter 14**: p. Unit14.20-Unit14.20.

165. Jang, M., et al., *Wavefront shaping with disorder-engineered metasurfaces*. Nature Photonics, 2018. **12**(2): p. 84-90.

166. Warren, S.C., et al., *Removing physiological motion from intravital and clinical functional imaging data*. Elife, 2018. **7**: p. e35800.

167. Feng, S., et al. *A subpixel registration algorithm for low PSNR images*. in *2012 IEEE Fifth International Conference on Advanced Computational Intelligence (ICACI)*. 2012. IEEE.

168. Dertinger, T., et al., *Fast, background-free, 3D super-resolution optical fluctuation imaging (SOFI)*. Proceedings of the National Academy of Sciences, 2009. **106**(52): p. 22287-22292.

169. Unekawa, M., et al., *RBC velocities in single capillaries of mouse and rat brains are the same, despite 10-fold difference in body size*. Brain Research, 2010. **1320**: p. 69-73.

170. Shih, A.Y., et al., *Two-photon microscopy as a tool to study blood flow and neurovascular coupling in the rodent brain*. Journal of cerebral blood flow and metabolism : official journal of the International Society of Cerebral Blood Flow and Metabolism, 2012. **32**(7): p. 1277-1309.

171. *bliQ Photonics: Video-rate Microscopy System*. *Available from* https://bliqphotonics.com/solutions/vms/.

172. Zhang, T., et al., *Kilohertz two-photon brain imaging in awake mice*. Nature methods, 2019. **16**(11): p. 1119-1122.

173. Mertz, J., H. Paudel, and T.G. Bifano, *Field of view advantage of conjugate adaptive optics in microscopy applications*. Applied optics, 2015. **54**(11): p. 3498-3506.

174. Park, J.-H., W. Sun, and M. Cui, *High-resolution in vivo imaging of mouse brain through the intact skull*. Proceedings of the National Academy of Sciences, 2015. **112**(30): p. 9236-9241.

175. Park, J.-H., et al., *Large-field-of-view imaging by multi-pupil adaptive optics*. Nat Meth, 2017. **14**(6): p. 581-583.

176. Navarro, R. and E. Moreno-Barriuso, *Laser ray-tracing method for optical testing*. Optics letters, 1999. **24**(14): p. 951-953.

177. Hell, S., et al., *Aberrations in confocal fluorescence microscopy induced by mismatches in refractive index*. Journal of microscopy, 1993. **169**(3): p. 391-405.

178. Babcock, H.W., *The possibility of compensating astronomical seeing*. Publications of the Astronomical Society of the Pacific, 1953. **65**(386): p. 229-236.

179. Ragazzoni, R., J. Farinato, and E. Marchetti. *Adaptive optics for 100-m-class telescopes: new challenges require new solutions*. in *Adaptive Optical Systems Technology*. 2000. International Society for Optics and Photonics.

180. Roddier, F., *V the effects of atmospheric turbulence in optical astronomy*, in *Progress in optics*. 1981, Elsevier. p. 281-376.

181. Antonello, J., et al., *Optimization-based wavefront sensorless adaptive optics for multiphoton microscopy*. JOSA A, 2014. **31**(6): p. 1337-1347.

182. Ji, N., *Adaptive optical fluorescence microscopy*. Nature Methods, 2017. **14**: p. 374.

183. Booth, M.J., *Adaptive optical microscopy: the ongoing quest for a perfect image*. Light: Science &Amp; Applications, 2014. **3**: p. e165.

184. Goodman, J.W., *Introduction to Fourier optics*. 2005: Roberts and Company Publishers.

185. Mahajan, V.N., *Zernike Circle Polynomials and Optical Aberrations of Systems with Circular Pupils*. Applied Optics, 1994. **33**(34): p. 8121-8124.

186. Kang, S., et al., *Simultaneous suppression of scattering and aberration for ultra-high resolution imaging deep within scattering media*. arXiv preprint arXiv:1609.07433, 2016.

187. Popoff, S., et al., *Measuring the transmission matrix in optics: an approach to the study and control of light propagation in disordered media*. Physical review letters, 2010. **104**(10): p. 100601.

188. Platt, B.C. and R. Shack, *History and principles of Shack-Hartmann wavefront sensing*. Journal of Refractive Surgery, 2001. **17**(5): p. S573-S577.

189. Tao, X., et al., *Adaptive optics microscopy with direct wavefront sensing using fluorescent protein guide stars*. Optics Letters, 2011. **36**(17): p. 3389-3391.

190. Tao, X., et al., *Adaptive optics confocal microscopy using direct wavefront sensing*. Optics Letters, 2011. **36**(7): p. 1062-1064.

191. Wang, K., et al., *Rapid adaptive optical recovery of optimal resolution over large volumes*. Nat Methods, 2014. **11**(6): p. 625-8.

192. Aviles-Espinosa, R., et al., *Measurement and correction of in vivo sample aberrations employing a nonlinear guide-star in two-photon excited fluorescence microscopy*. Biomedical Optics Express, 2011. **2**(11): p. 3135-3149.

193. Albert, O., et al., *Smart microscope: an adaptive optics learning system for aberration correction in multiphoton confocal microscopy*. Optics Letters, 2000. **25**(1): p. 52-54.

194. Wright, A.J., et al., *Exploration of the optimisation algorithms used in the implementation of adaptive optics in confocal and multiphoton microscopy*. Microsc Res Tech, 2005. **67**(1): p. 36-44.

195. Booth, M.J., et al., *Adaptive aberration correction in a confocal microscope*. Proceedings of the National Academy of Sciences, 2002. **99**(9): p. 5788-5792.

196. Débarre, D., et al., *Image-based adaptive optics for two-photon microscopy*. Optics Letters, 2009. **34**(16): p. 2495-2497.

197. Milkie, D.E., E. Betzig, and N. Ji, *Pupil-segmentation-based adaptive optical microscopy with full-pupil illumination*. Optics Letters, 2011. **36**(21): p. 4206-4208.

198. Ji, N., T.R. Sato, and E. Betzig, *Characterization and adaptive optical correction of aberrations during in vivo imaging in the mouse cortex*. Proceedings of the National Academy of Sciences, 2012. **109**(1): p. 22-27.

199. Le Roux, B., et al., *Optimal control law for classical and multiconjugate adaptive optics*. JOSA A, 2004. **21**(7): p. 1261-1276.

200. Kulcsár, C., et al., *Optimal control, observers and integrators in adaptive optics*. Optics express, 2006. **14**(17): p. 7464-7476.

201. Freeman, R.H. and J.E. Pearson, *Deformable mirrors for all seasons and reasons*. Applied Optics, 1982. **21**(4): p. 580-588.

202. Bifano, T., *Adaptive imaging: MEMS deformable mirrors*. Nature Photonics, 2011. **5**(1): p. 21-23.

203. Fernández, E.J., et al., *Adaptive optics with a magnetic deformable mirror: applications in the human eye*. Optics Express, 2006. **14**(20): p. 8900-8917.

204. Love, G.D., *Wave-front correction and production of Zernike modes with a liquid-crystal spatial light modulator*. Applied optics, 1997. **36**(7): p. 1517-1524.

205. Allen, J., *Application of patterned illumination using a DMD for optogenetic control of signaling*. Nature Methods, 2017. **14**.

206. Lee, W.-H., *Binary computer-generated holograms*. Applied Optics, 1979. **18**(21): p. 3661-3669.

207. Jang, J., et al., *Complex wavefront shaping for optimal depth-selective focusing in optical coherence tomography*. Optics Express, 2013. **21**(3): p. 2890-2902.

208. Dudley, D., W.M. Duncan, and J. Slaughter. *Emerging digital micromirror device (DMD) applications*. in *MOEMS display and imaging systems*. 2003. International Society for Optics and Photonics.

209. Pozzi, P., et al., *High speed wavefront sensorless aberration correction in digital micromirror based confocal microscopy*. Optics Express, 2017. **25**(2): p. 949-959.

210. Wang, K., et al., *Direct wavefront sensing for high-resolution in vivo imaging in scattering tissue*. Nat Commun, 2015. **6**: p. 7276.

211. Bifano, T.G., et al., *Adaptive optics two photon microscopy with direct wavefront sensing using autofluorescent guide-stars*. 2014. **8978**: p. 89780D.

212. Booth, M.J., *Wavefront sensorless adaptive optics for large aberrations*. Optics Letters, 2007. **32**(1): p. 5-7.

213. Jesacher, A., et al., *Adaptive harmonic generation microscopy of mammalian embryos*. Optics letters, 2009. **34**(20): p. 3154-3156.

214. Feierabend, M., M. Rückel, and W. Denk, *Coherence-gated wave-front sensing in strongly scattering samples*. Optics Letters, 2004. **29**(19): p. 2255-2257.

215. Rueckel, M., J.A. Mack-Bucher, and W. Denk, *Adaptive wavefront correction in two-photon microscopy using coherence-gated wavefront sensing*. Proceedings of the National Academy of Sciences, 2006. **103**(46): p. 17137-17142.

216. Ellerbroek, B.L., *First-order performance evaluation of adaptive-optics systems for atmospheric-turbulence compensation in extended-field-of-view astronomical telescopes*. Journal of the Optical Society of America A, 1994. **11**(2): p. 783-805.

217. Ragazzoni, R., E. Marchetti, and G. Valente, *Adaptive-optics corrections available for the whole sky*. Nature, 2000. **403**: p. 54.

218. Booth, M.J., *Wave front sensor-less adaptive optics: a model-based approach using sphere packings*. Optics Express, 2006. **14**(4): p. 1339-1352.

219. Wu, T.-w. and M. Cui, *Numerical study of multi-conjugate large area wavefront correction for deep tissue microscopy*. Optics Express, 2015. **23**(6): p. 7463-7470.

220. Boyden, E.S. and A.H. Marblestone, *Architecting Discovery: A Model for How Engineers Can Help Invent Tools for Neuroscience*. Neuron, 2019. **102**(3): p. 523-525.

221. Suárez-Gómez, S.L., et al., *An approach using deep learning for tomographic reconstruction in solar observation*. Proceedings of the Adaptive Optics for Extremely Large Telescopes, 2017. **5**.

222. Tokunaga, A.T., *Chapter 51 - New Generation Ground-Based Optical/Infrared Telescopes*, in *Encyclopedia of the Solar System (Third Edition)*, T. Spohn, D. Breuer, and T.V. Johnson, Editors. 2014, Elsevier: Boston. p. 1089-1105.

223. Thorlabs. *Piezoelectric Deformable Mirrors*. Available from: https://www.thorlabs.com/newgrouppage9.cfm?objectgroup_id=5056.

224. Booth, M.J., M.A. Neil, and T. Wilson, *Aberration correction for confocal imaging in refractive - index - mismatched media*. Journal of microscopy, 1998. **192**(2): p. 90-98.

225. McNally, J.G., et al., *Three-dimensional imaging by deconvolution microscopy*. Methods, 1999. **19**(3): p. 373-385.

226. Roddier, F., *Wavefront sensing and the irradiance transport equation*. Applied Optics, 1990. **29**(10): p. 1402-1403.

227. Li, Y., et al., *Raster adaptive optics for video rate aberration correction and large FOV multiphoton imaging*. Biomedical Optics Express, 2020. **11**(2): p. 1032-1042.

228. Göbel, W., B.M. Kampa, and F. Helmchen, *Imaging cellular network dynamics in three dimensions using fast 3D laser scanning*. Nature methods, 2007. **4**(1): p. 73.

229. Zong, W., et al., *Large-field high-resolution two-photon digital scanned light-sheet microscopy*. Cell research, 2015. **25**(2): p. 254-257.

230. Sofroniew, N.J., et al., *A large field of view two-photon mesoscope with subcellular resolution for in vivo imaging*. Elife, 2016. **5**: p. e14472.

231. Botcherby, E.J., et al., *Aberration-free three-dimensional multiphoton imaging of neuronal activity at kHz rates*. Proc Natl Acad Sci U S A, 2012. **109**(8): p. 2919-24.

232. *Aberration-free optical refocusing in high numerical aperture microscopy*. Opt. Lett., 2007. **32**: p. 2007.

233. Okada, T. and J.G. Cyster, *B cell migration and interactions in the early phase of antibody responses*. Current opinion in immunology, 2006. **18**(3): p. 278-285.

234. Levoy, M., et al. *Light field microscopy*. in *ACM Transactions on Graphics (TOG)*. 2006. ACM.

235. Broxton, M., et al., *Wave optics theory and 3-D deconvolution for the light field microscope*. Optics Express, 2013. **21**(21): p. 25418-25439.

236. Prevedel, R., et al., *Simultaneous whole-animal 3D imaging of neuronal activity using light-field microscopy*. Nature methods, 2014. **11**(7): p. 727.

237. Ishikawa-Ankerhold, H.C., R. Ankerhold, and G.P. Drummen, *Advanced fluorescence microscopy techniques—Frap, Flip, Flap, Fret and flim*. Molecules, 2012. **17**(4): p. 4047-4132.

238. Axelrod, D., et al., *Mobility measurement by analysis of fluorescence photobleaching recovery kinetics*. Biophysical Journal, 1976. **16**(9): p. 1055-1069.

239. Patterson, G.H. and J. Lippincott-Schwartz, *A Photoactivatable GFP for Selective Photolabeling of Proteins and Cells*. Science, 2002. **297**(5588): p. 1873-1877.

240. Callaway, E.M. and L.C. Katz, *Photostimulation using caged glutamate reveals functional circuitry in living brain slices*. Proceedings of the National Academy of Sciences, 1993. **90**(16): p. 7661-7665.

241. Nagel, G., et al., *Channelrhodopsin-1: A Light-Gated Proton Channel in Green Algae*. Science, 2002. **296**(5577): p. 2395-2398.

242. RAABE, I., et al., *Intracellular nanosurgery and cell enucleation using a picosecond laser*. Journal of Microscopy, 2009. **234**(1): p. 1-8.

243. Ellis-Davies, G.C.R., *Caged compounds: photorelease technology for control of cellular chemistry and physiology*. Nature methods, 2007. **4**(8): p. 619-628.

244. Boulnois, J.-L., *Photophysical processes in recent medical laser developments: A review*. Lasers in Medical Science, 1986. **1**(1): p. 47-66.

245. *Artifacts of light*. Nature Methods, 2013. **10**: p. 1135.

246. Hoebe, R., et al., *Controlled light-exposure microscopy reduces photobleaching and phototoxicity in fluorescence live-cell imaging*. Nature biotechnology, 2007. **25**(2): p. 249.

247. Shih, A.Y., et al., *The smallest stroke: occlusion of one penetrating vessel leads to infarction and a cognitive deficit*. Nature neuroscience, 2013. **16**(1): p. 55.

248. Olivier, N., et al., *Two-photon microscopy with simultaneous standard and extended depth of field using a tunable acoustic gradient-index lens*. Optics letters, 2009. **34**(11): p. 1684-1686.

249. *Laser power modulation: EOMs and AOMs – Labrigger*.

250. Ellenberg, J., et al., *Nuclear membrane dynamics and reassembly in living cells: targeting of an inner nuclear membrane protein in interphase and mitosis*. The Journal of cell biology, 1997. **138**(6): p. 1193-1206.

251. Koppel, D., et al., *Dynamics of fluorescence marker concentration as a probe of mobility*. Biophysical Journal, 1976. **16**(11): p. 1315-1329.

252. Mazza, D., et al., *A new FRAP/FRAPa method for three-dimensional diffusion measurements based on multiphoton excitation microscopy*. Biophysical journal, 2008. **95**(7): p. 3457-3469.

253. Nishimura, N., et al. *Targeted disruption of deep-lying neocortical microvessels in rat using ultrashort laser pulses*. in *Commercial and Biomedical Applications of Ultrafast Lasers IV*. 2004. International Society for Optics and Photonics.

254. Lippincott-Schwartz, J., N. Altan-Bonnet, and G.H. Patterson, *Photobleaching and photoactivation: following protein dynamics in living cells*. Nature cell biology, 2003: p. S7-14.

255. Carlson, A.L., et al., *Tracking single cells in live animals using a photoconvertible near-infrared cell membrane label*. PloS one, 2013. **8**(8): p. e69257.

256. Deschout, H., et al., *Straightforward FRAP for quantitative diffusion measurements with a laser scanning microscope*. Optics express, 2010. **18**(22): p. 22886-22905.

257. Meleard, P., L.A. Bagatolli, and T. Pott, *Giant unilamellar vesicle electroformation: From lipid mixtures to native membranes under physiological conditions*. Methods in enzymology, 2009. **465**: p. 161-176.

258. Breier, G., *Angiogenesis in Embryonic Development—A Review*. Placenta, 2000. **21**: p. S11-S15.

259. Kinstlinger, I.S. and J.S. Miller, *3D-printed fluidic networks as vasculature for engineered tissue*. Lab on a Chip, 2016. **16**(11): p. 2025-2043.

260. Cahalan, M.D., et al., *Two-photon tissue imaging: seeing the immune system in a fresh light*. Nature Reviews Immunology, 2002. **2**(11): p. 872-880.

261. Vennin, C., et al., *Reshaping the Tumor Stroma for Treatment of Pancreatic Cancer*. Gastroenterology, 2018. **154**(4): p. 820-838.

262. Vennin, C., et al., *Intravital imaging reveals new ancillary mechanisms co-opted by cancer cells to drive tumor progression [version 1; peer review: 2 approved]*. F1000Research, 2016. **5**(892).

263. Karreman, M.A., et al., *Fast and precise targeting of single tumor cells in vivo by multimodal correlative microscopy*. J Cell Sci, 2016. **129**(2): p. 444-56.

264. Weber, E.W., et al., *TRPC6 is the endothelial calcium channel that regulates leukocyte transendothelial migration during the inflammatory response*. J Exp Med, 2015. **212**(11): p. 1883-99.

265. Grutzendler, J., et al., *Angiophagy prevents early embolus washout but recanalizes microvessels through embolus extravasation*. Sci Transl Med, 2014. **6**(226): p. 226ra31.

266. Furie, B. and B.C. Furie, *Mechanisms of thrombus formation*. New England Journal of Medicine, 2008. **359**(9): p. 938-949.

267. Halkar, M. and A.M. Lincoff, *Dual antiplatelet therapy for acute coronary syndromes: How long to continue?* Cleve Clin J Med, 2016. **83**: p. 675-688.

268. Pink, D.B., et al., *Real-time visualization and quantitation of vascular permeability in vivo: implications for drug delivery*. PloS one, 2012. **7**(3): p. e33760.

269. Dubois, C., et al., *Thrombin-initiated platelet activation in vivo is vWF independent during thrombus formation in a laser injury model*. The Journal of clinical investigation, 2007. **117**(4): p. 953-960.

270. Adarve, J.D. and R. Mahony, *A filter formulation for computing real time optical flow*. IEEE Robotics and Automation Letters, 2016. **1**(2): p. 1192-1199.

271. Lim, Y.J., Y. Li, and W.M. Lee. *Achieving 3D FRAP using multiphoton polygon scanning microscopy*. in *Biophotonics Australasia 2019*. 2019. International Society for Optics and Photonics.

272. Gaertner, F., et al., *Migrating Platelets Are Mechano-scavengers that Collect and Bundle Bacteria*. Cell, 2017. **171**(6): p. 1368-1382 e23.

Appendix A Polygon Microscope Operation

A.1 Start the Laser

The laser source for the 3D 2p microscope is a TI-sapphire femtosecond pulse laser (Tsunami, Model 3960, Spectra Physics). It can output a laser with a tunable wavelength from 690-930 nm with maximum 800 mW power.

To start up the laser, first, need to press the “LASER POWER” button on the remote controller once to warm up the laser if it is the first time of the day using the laser (‘cold start’ of the T40 power supply). The warm-up time can take up to 20 minutes. After the warm-up is finished, the device will enter Standby mode. For a ‘warm start’, hold the “LASER POWER”

button for a few seconds until heard the click sound or the red indicator light is on. Then wait a few minutes until the power is pumped up to pre-set 5 W.

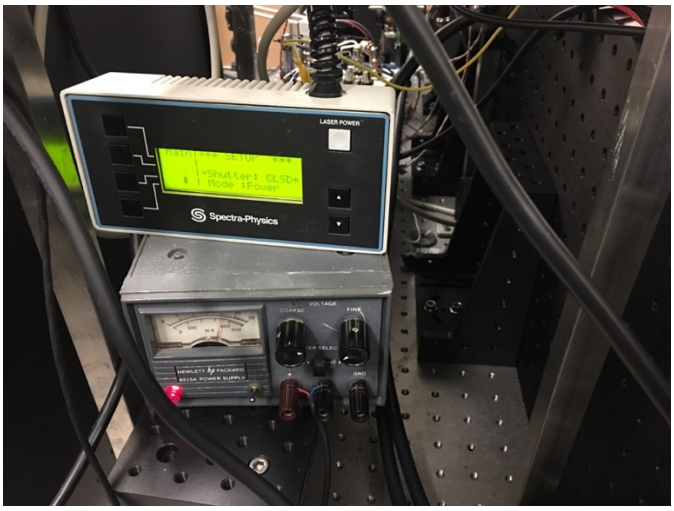

Fig. A.1 Laser controller above and the mechanical shutter control below.

A.2 Start the Electronic Devices and Drivers

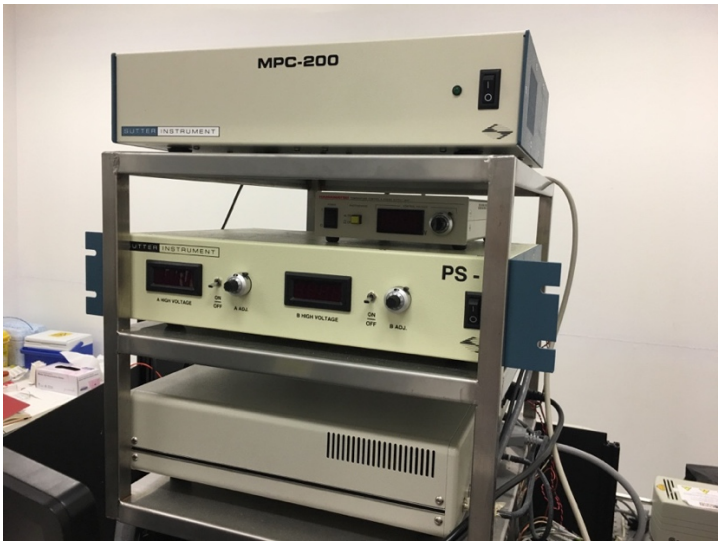

Fig. A.2 Devices above the bench, from top to bottom are the stage controller, GaAsP detector power supply, PMT power supply and mode lock controller.

This polygon microscope uses a scanning laser with a combination of the polygon mirror, galvanometer mirror and deformable mirror. Three detectors are used: one GaAsP and two PMT detectors. All these devices need their corresponding drivers to function, which are switched on and controlled by specific devices.

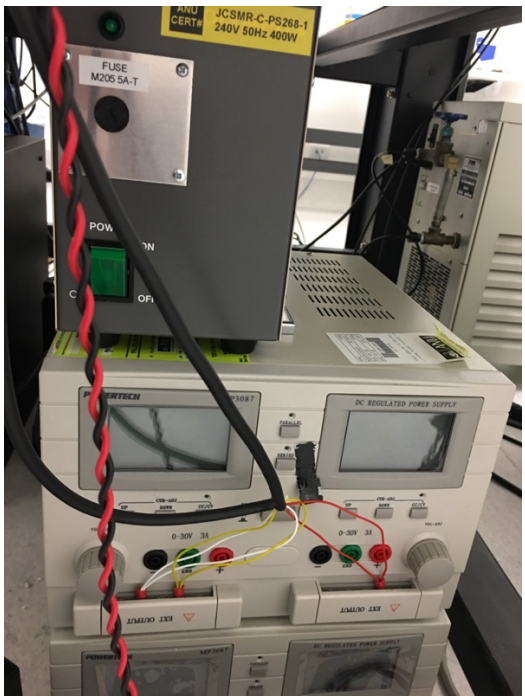

Fig. A.3 Below the optical table, from top to bottom are polygon driver power supply, PMT amplifier power supply and galvo driver power supply.

Before switching on the GaAsP and PMT power supply units, ensure that the photosensor switches for the GaAsP and PMT units are set to off, and dials are set to minimum (see Fig. A.4), as room lighting can damage the PMT. The instruments in Fig. A.3 should be switched on one by one. For the PMT amplifier button, please remember to press the series button to make it work in series mode since the amplifiers require a polarized input (running at a ±5V).

A.3 Run the Microscope

Now all the preparation should be done; please wear the safety glasses with the proper IR protection. Open both the shutter of the remote laser controller (pressing the directional

arrows) and mechanic driver switch (mechanical toggle) shown in Fig. A.5. Tap on the optical table until the mode-locking light is on. Open the MATLAB 2015b, run the imagui.m file (PScan). The GUI loaded can be used for image preview, acquisition, saving, and averaging, multisite photomanipulation and video-rate AO. The detail will be shown in Appendix C.

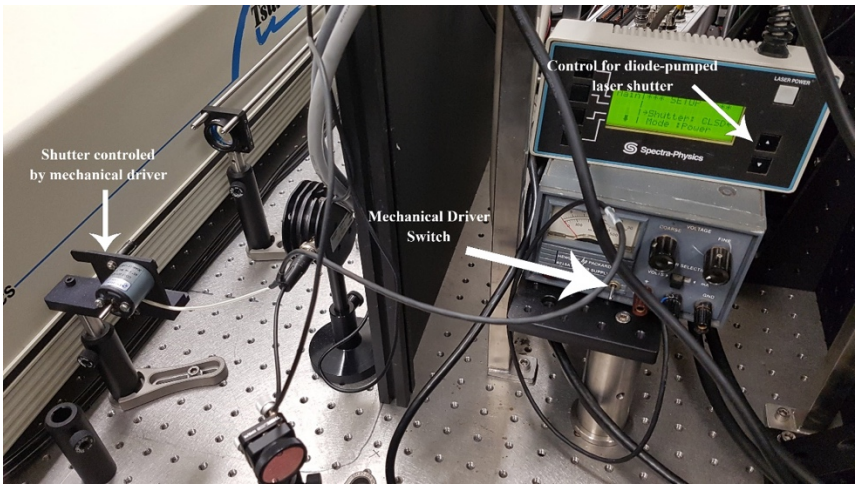

Fig. A.3 Controls for laser shutters. The switch button controls the shutter after the Tsunami laser. The remote controller controls the shutter before the Tsunami laser.

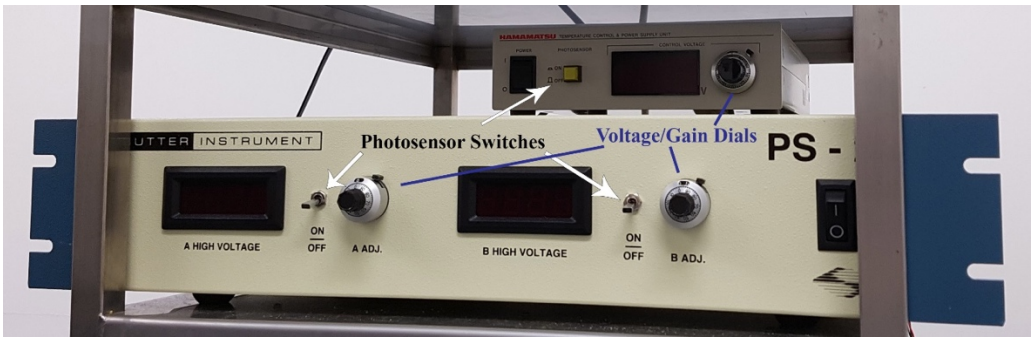

Fig. A.4 Controls for the GaAsP and standard PMTs.

Finally, switch off room lights and then switch on the photosensor switches. Adjust the voltage/gain of the PMTs with the dials.

Appendix B Animal Experiment Protocol

1. Anesthetize the mouse using IP injection of ketamine(10mg/ml)/xylazine(2mg/ml) solution.
2. Monitor the depth of anaesthesia by checking reflexes until it is sufficiently anaesthetized.
3. Remove the hair around the target area using removal cream and paper tissues, put the mouse onto the stage with a heating plate for body temperature maintaining (Fig. B.1 a)).
4. Prepare the 3D printed holder and coverslip (Fig. B.1 b)).
5. Make a 3 to 5 mm incision on the skin.
6. Inject 100 ul of dyes like FITC-dextran (3% w/v) intravenously (retro-orbital).
7. Locate the chosen leg onto the 3D printed holder (Fig. B.1 c)).

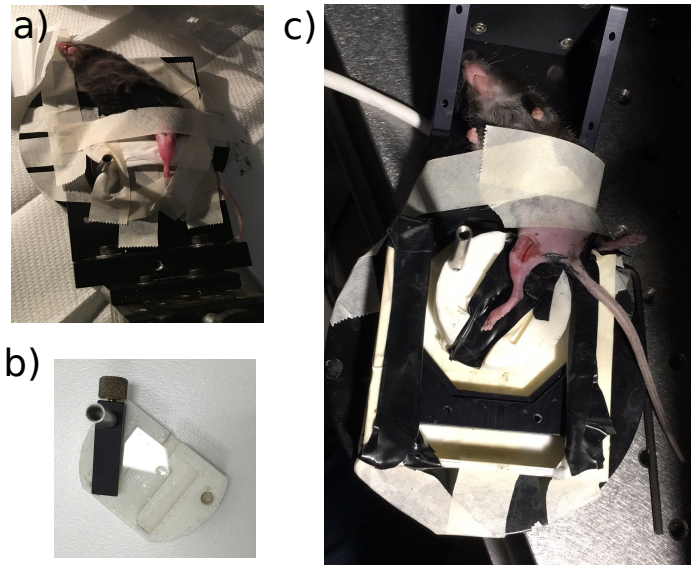

Fig. B.1 Procedure of the animal surgery preparation. a) Hair move. b) 3D printed holder. c) Image of the animal after surgery.

8. Put the coverslip mounting by a clamp to flatten the imaging area. A metal ring will be attached to the imaging area sealed by ointment, dip a drop of PBS, the drop will be maintained in the ring area if the ring is sealed well (Fig. B.2 a)).
9. Put the mouse under the objective lens and move the stage by the controller. Be aware of the imaging distance, not press the coverslip with the objective lens, when the front of the objective lens is immersed with the liquid, it is ready to start multiphoton imaging (Fig. B.2 b), c)).

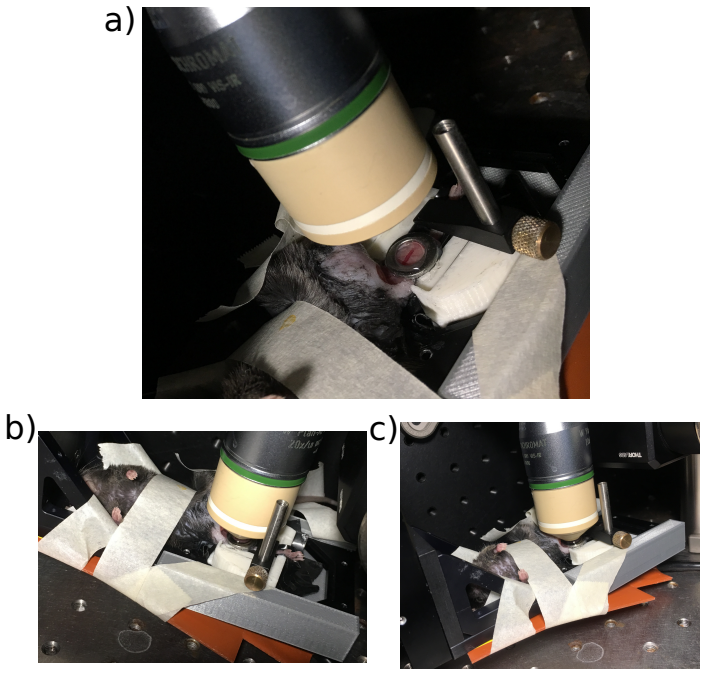

Fig. B.2 Procedure of animal imaging preparation. a) Put the coverslip onto the holder, and allocate the animal under the objective lens. b) Control the distance of the stage and the objective lens, make the objective lens touched and immersed by the immersion liquid. c) Animal during imaging experiment.

Appendix C Running PScan Software

PScan software includes a MATLAB based GUI and supporting configuration files of Matrox frame grabber and LabVIEW based devices control. The address of acquiring PScan software can be found by searching the name "PScan-MicroscopyControlSoftware" on GitHub, https://github.com/unisteo/PScan-MicroscopyControlSoftware, the current webpage is shown in Fig. C. 1.

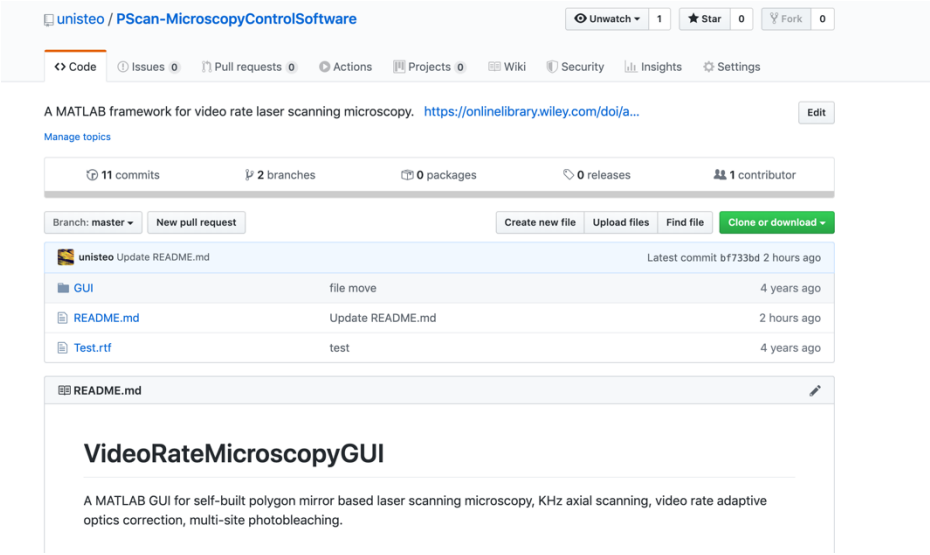

Fig. C.1 Pscan repository page on GitHub. The working profile locates in the GUI folder.

Download the GUI folder, put it on the MATLAB's default working folder. The GUI folder includes the MATLAB main program named "imagui.m", the LabVIEW program folder "LabVIEW", and a series of Matrox frame grabber configuration DCF files, as shown in Fig. C. 2.

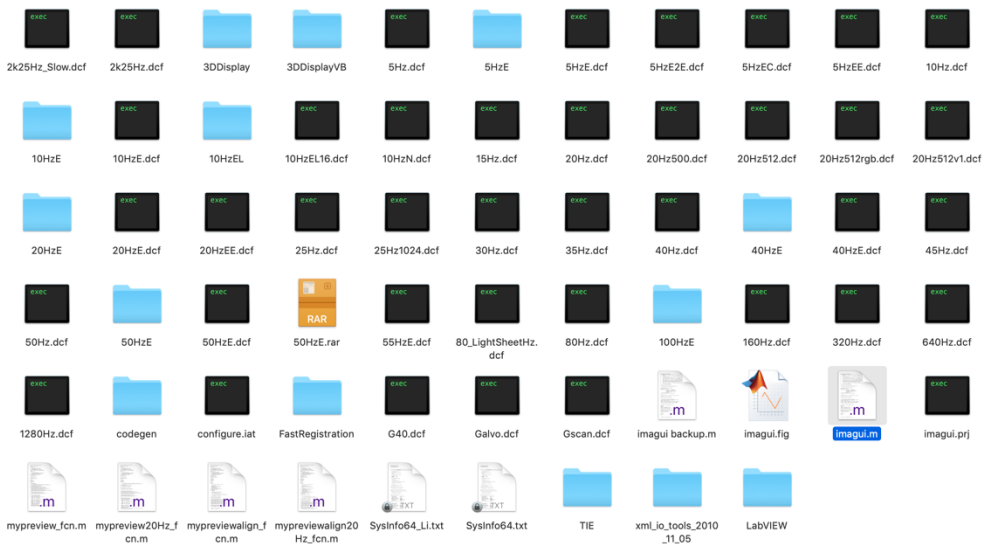

Fig. C. 2 The files and subfolders of the main GUI folder. The selected “imagui.m” file is the main program file of PScan.

Open the “imagui.m” file with MATLAB 2015(b), and run the file, PScan will first do an initialization which will open the corresponding ImageJ packages, LabVIEW project folder and then after the initialization, PScan GUI will be automatically opened. The opened LabVIEW project folder and “imagui.m” are shown in Fig. C. 3.

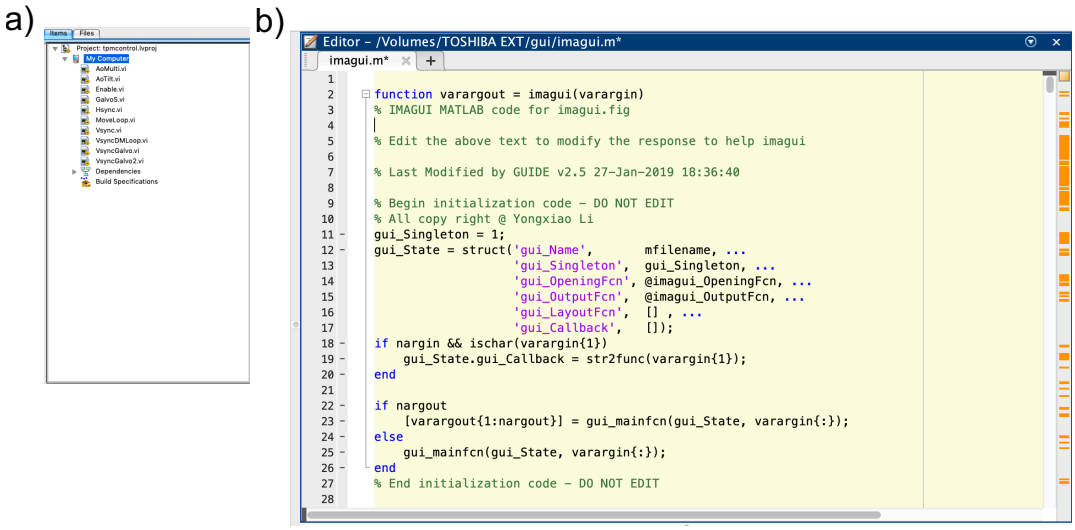

Fig. C. 3 The project window of LabVIEW and PScan main program in MATLAB. a) LabVIEW project named “tpmcontrol.lvproj”. All the required Labview programs are included and will be

running as background programs controlled by the MATLAB GUI. b) Opened PScan main program "imagui" in script window of MATLAB.

After the GUI is opened, then the corresponding control of the MATLAB program is available. The opened GUI (PScan with AO function) is shown in Fig. C. 4. All the functions are grouped by devices and corresponding controls for instant access. For instance, "Acquisition" and "Color Reference" on the top left is the control of live view of samples and corresponding manipulations, like saving and averaging. On the bottom left is the multisite photomanipulation panel. An demonstration video can be found on the supporting material in the published paper [101]. The dialogue bars on the bottom of GUI are grouped as "Saving Path" and "Status Indicator", used for file saving and command control as well as PScan's return value display.

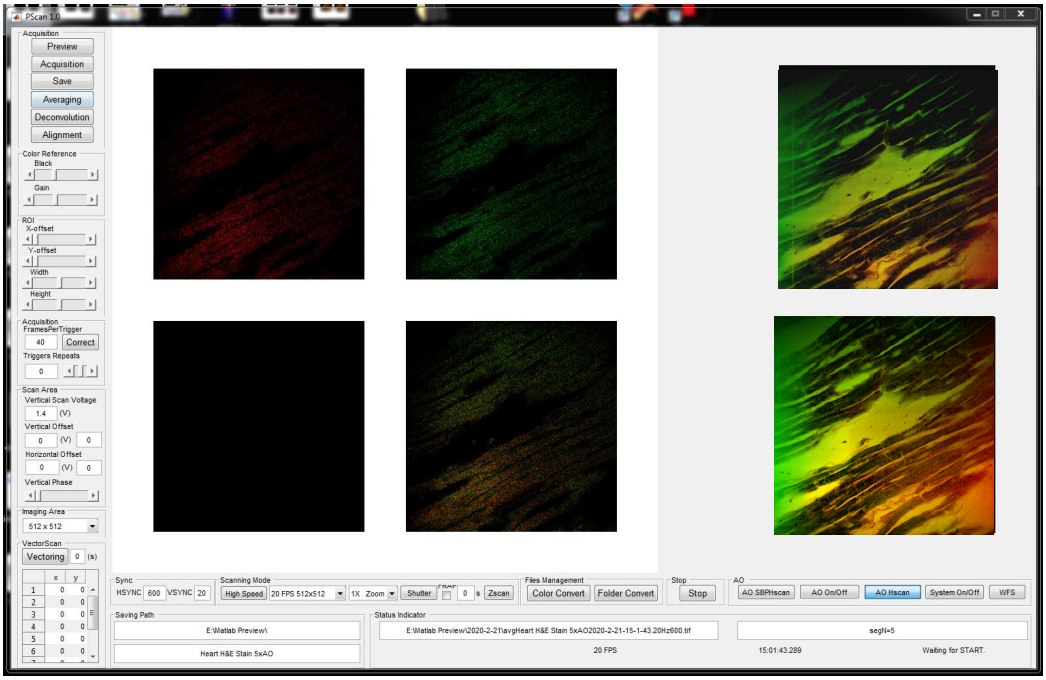

Fig. C. 4 GUI of PScan, designed and grouped by the functions and related devices control.